Nonlinear Dielectric Responses of Glasses and Glass-Ceramics in the Microwave Range

Dissertation
zur Erlangung des Grades
"Doktor der Naturwissenschaften"
am Fachbereich Physik, Mathematik und Informatik
der Johannes Gutenberg-Universität
in Mainz

Florian Bergmann
geboren in Bonn

JOHANNES GUTENBERG UNIVERSITÄT MAINZ

JG|U

Mainz, 2021

Datum der mündlichen Prüfung: 22. September 2021
Erster Berichterstatter: Prof. Dr. Gerhard Jakob
Zweiter Berichterstatter: [wegen Datenschutz entfernt]

Abstract

The ever-increasing data traffic by a growing number of communicating wireless devices calls for a larger bandwidth and for its efficient use in the fifth (5G) and sixth (6G) mobile communication generations. The bandwidth is extended by utilizing higher frequencies. However, a phenomenon that troubles the efficient use of bandwidth is passive intermodulation (PIM). PIM leads to channel cross talk and has its origin in any kind of nonlinear response. One such source is the nonlinear electric susceptibility of dielectrics in microwave devices.

This work deals with the characterization of the nonlinear electric susceptibility of glasses and glass-ceramics at microwave frequencies. Glasses and glass-ceramics exhibit advantageous properties for microwave devices compared to classically employed sintered ceramics or PTFE compounds, such as better metal adhesion and higher homogeneity. The nonlinear susceptibility of a $Ba_4Al_2Ti_{10}O_{27}$ glass-ceramic was determined to $|\chi_3| = (4 \pm 2) \times 10^{-16}\,\mathrm{m^2/V^2}$ at 1 GHz. The intermodulation level observed during this measurement cannot be adequately described by a classical power-law representation of the nonlinearity. While the power-law description is only applicable within its radius of convergence, an alternative approach based on Fourier coefficient integrals allows accurate description of the dependency of intermodulation levels on input power over a wider range. Using established physical nonlinear response models, this description additionally allows determining previously inaccessible model parameters, such as the linear contribution of the nonlinear mechanism ($\chi_1 = 10^{-8}$).

The experimental setup was extended to also characterize materials with lower permittivity, including a glass. SiO_2 immiscibilities in the glass were found to increase the nonlinear microwave response significantly without having a measurable impact on the linear dielectric properties.

For comparison, the nonlinear susceptibility of the $Ba_4Al_2Ti_{10}O_{27}$ glass-ceramic was measured with a 1 kHz ultra-high precision capacitance bridge under a high DC voltage bias, resulting in a nonlinear susceptibility, which is higher by three orders of magnitude than in the GHz range. The kHz nonlinear susceptibility was shown to increase with the crystallite size in the glass-ceramic.

In summary, both the experimental method as well as the theoretical description of intermodulation open new prospects in understanding dielectrics and nonlinear responses in general and thus laying a foundation for higher performance microwave devices.

Kurzfassung

Der stetig steigende Datenverkehr einer wachsenden Zahl von drahtlos kommunizierenden Geräten erfordert eine größere Bandbreite und deren effiziente Nutzung in der fünften (5G) und sechsten (6G) Mobilfunkgeneration. Die Bandbreite wird durch die Erweiterung zu höheren Frequenzen erreicht. Ein Effekt, der jedoch die effiziente Nutzung der Bandbreite beeinträchtigt, ist passive Intermodulation (PIM). PIM verursacht Übersprechen zwischen Kanälen und wird von jeglicher Art nichtlinearer Antwort hervorgerufen. Eine davon ist die nichtlineare elektrische Suszeptibilität von Dielektrika in Mikrowellengeräten.

Diese Arbeit beschäftigt sich mit der Charakterisierung der nichtlinearen elektrischen Suszeptibilität von Gläsern und Glaskeramiken bei Mikrowellenfrequenzen. Gläser und Glaskeramiken weisen im Vergleich zu gewöhnlich eingesetzten gesinterten Keramiken oder PTFE-Verbindungen vorteilhafte Eigenschaften für Mikrowellengeräte auf, wie eine bessere Metallhaftung und eine höhere Homogenität.

Die nichtlineare Suszeptibilität einer $Ba_4Al_2Ti_{10}O_{27}$ Glaskeramik wurde bei 1 GHz zu $|\chi_3| = (4 \pm 2) \times 10^{-16}\,\mathrm{m^2/V^2}$ bestimmt. Das bei dieser Messung beobachtete Intermodulationslevel kann nicht angemessen durch eine Nichtlinearität in Form einer klassischen Potenzreihe beschrieben werden. Während diese Potenzreihe nur innerhalb ihres Konvergenzradius anwendbar ist, kann ein alternativer, auf einem Fourierkoeffizientenintegral basierender Ansatz die Abhängigkeit des Intermodulationslevels von der Eingangsleistung präzise über einen größeren Leistungsbereich vorhersagen. Die Anwendung dieser Beschreibung auf etablierte physikalische nichtlineare Modelle ermöglicht zusätzlich die Bestimmung von vorher unzugänglichen Modelparametern wie dem linearen Anteil des nichtlinearen Mechanismus ($\chi_1 = 10^{-8}$).

Der Messaufbau wurde für die Charakterisierung von kleineren Permittivitäten erweitert. Dies ermöglichte die Charakterisierung eines Glases. Es wurde festgestellt, dass SiO_2 Entmischungen in dem Glas die Nichtlinearität signifikant erhöhen, ohne dabei einen messbaren Einfluss auf die linearen dielektrischen Eigenschaften zu haben.

Vergleichsmessungen an der $Ba_4Al_2Ti_{10}O_{27}$ Glaskeramik mit einer 1 kHz Präzisionskapazitätsbrücke unter einer zusätzlichen Gleichspannung ergaben eine um drei Größenordnungen höhere Nichtlinearität im Vergleich zu den GHz Messungen. Es wurde festgestellt, dass die kHz-Nichtlinearität mit der Kristallitgröße in der Glaskeramik ansteigt.

Zusammenfassend lässt sich sagen, dass sowohl die experimentelle Methode als auch die theoretische Beschreibung von Intermodulationen neue Perspektiven im Verständnis von Dielektrika und Nichtlinearitäten im Allgemeinen eröffnet und damit eine Grundlage für leistungsfähigere Mikrowellengeräte legt.

Contents

List of Figures

List of Tables

Chapter 1

Introduction and Motivation

Society in the 21st century is increasingly relying on digitization and data [MLa19]. An ever-rising number of communicating devices (the "Internet of Things") and the enormous amount of data ("Big Data") call for a growing high speed data volume. This demand challenges various fields of science. Besides software solutions to tackle the data volume (e.g. "Neural Networks"), hardware issues that arise from the increasing data traffic need to be addressed. Generally, higher data rates are obtained by resorting to higher frequencies. This favors optical devices. However, it is a futile endeavor to connect all devices by optical fibers, especially mobile devices. The other window that nature offers for wireless information transfer are microwave frequencies. This band is home to cell phone standards (GSM, UMTS, LTE, 5G), global navigation satellite systems (GPS, GLONASS, Galileo, Beidou) and other more localized systems (WLAN, Bluetooth). The rapid growth in mobile data traffic of such techniques is visualized in Figure 1.1.

All these players need to be arranged in a limited bandwidth. The separation of user communication channels can occur in the time domain (time division multiple access, TDMA) or in the frequency domain (frequency division multiple access, FDMA). In TDMA, the devices need to be synchronized to assign at which point which device transmits or receives. FDMA assigns each device a transmitting and receiving band that it can use all the time. The same issue arises for uplink and downlink communication of just two devices and can be addressed by time or frequency division duplexing (TDD and FDD). To handle the enormous data traffic and number of devices, the usable bandwidth needs to be extended, especially to higher frequencies, and the available frequencies have to be made efficient use of. Higher frequencies make use of the fundamental relation between available bandwidth and data rate [Har28].

As visible in the increasing number of publications in relation to "microwave materials" in Figure 1.2, the materials for microwave devices have gained interest. Dielectrics are one class that plays a key role. They are found in various roles such as substrates having a low permittivity or as dielectric resonators with a high permittivity. The substrates are used as a basis for printing metal lines to obtain integrated circuits. Besides the low permittivity, substrate materials are mostly required to have low dielectric loss,

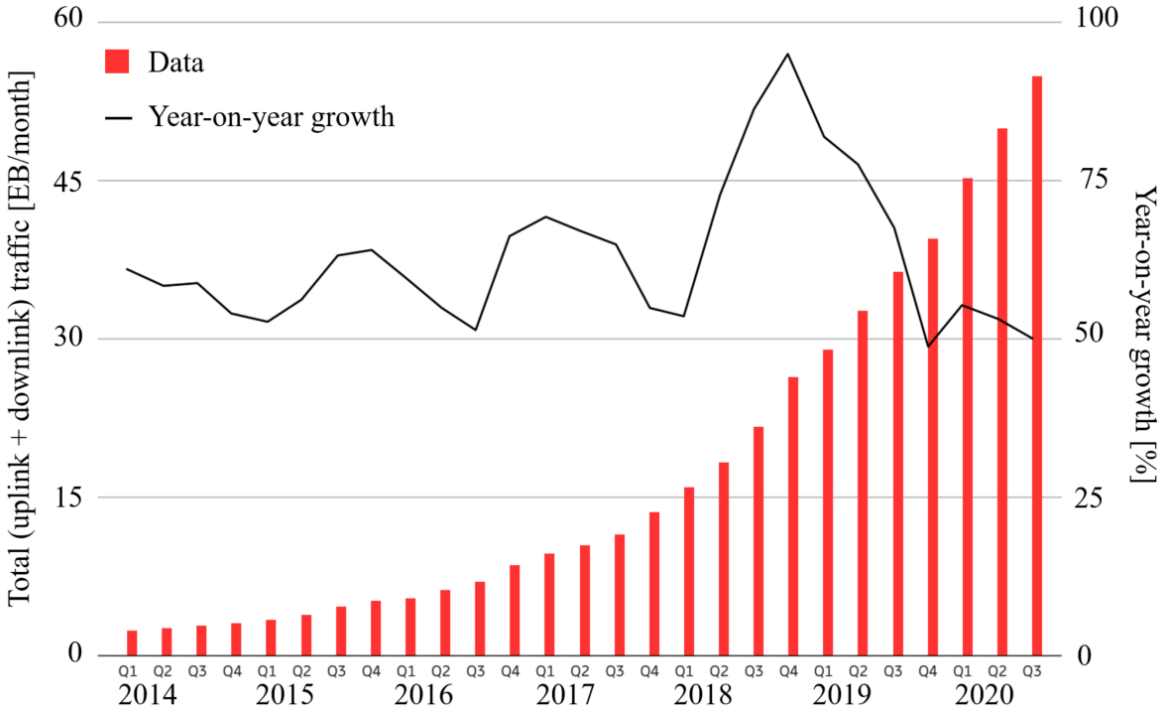

Figure 1.1: Global mobile network data traffic and year-on-year growth [JDL+20].

a good metal adhesion and suitable thermal properties. Dielectric resonators, on the other hand, are a basis for filters. Filters are the backbone of FDMA/FDD as they carry signals of specific frequencies and block signals from adjacent bands. Here, low loss is essential for frequency selectivity. Dielectric resonators are preferred to metal cavity resonators because they outperform metal cavities in their temperature stability and size [Seb08]. Substrates usually are material composites of (sometimes glass-reinforced) epoxy laminates. Dielectric resonators, on the other hand, are commonly made of sintered ceramics. Even though these materials have been optimized for current applications and exhibit outstanding dielectric properties, glasses and glass-ceramics offer some advantages over both classically employed material classes when advancing to higher frequencies: as the devices decrease in size together with the wavelength, tighter absolute tolerances on both the dielectric and geometric properties are required. Glasses possess a highly homogeneous permittivity. For instance, optical glasses having a homogeneity $\Delta\varepsilon_r/\varepsilon_r < 5 \times 10^{-5}$ over lenses of 20 cm diameter are standard in industrial production [Opt20]. Additionally, glasses can be machined with high precision (i.e. a few µm) and the feasibility of structuring glass of 50 µm thickness has been demonstrated [LZV+18]. Finally, the lower porosity of glasses and glass-ceramics allow better metal adhesion than PTFE substrates and sintered ceramics [BMH+17]. The glass passes these properties onto the glass-ceramic. The homogeneity of the permittivity is especially critical for filter applications, as batch-to-batch variations of the permittivity impose the necessity of post-processing due to the lack of reproducibility.

However, even with small bandwidth filters, the efficient use of the frequency spectrum

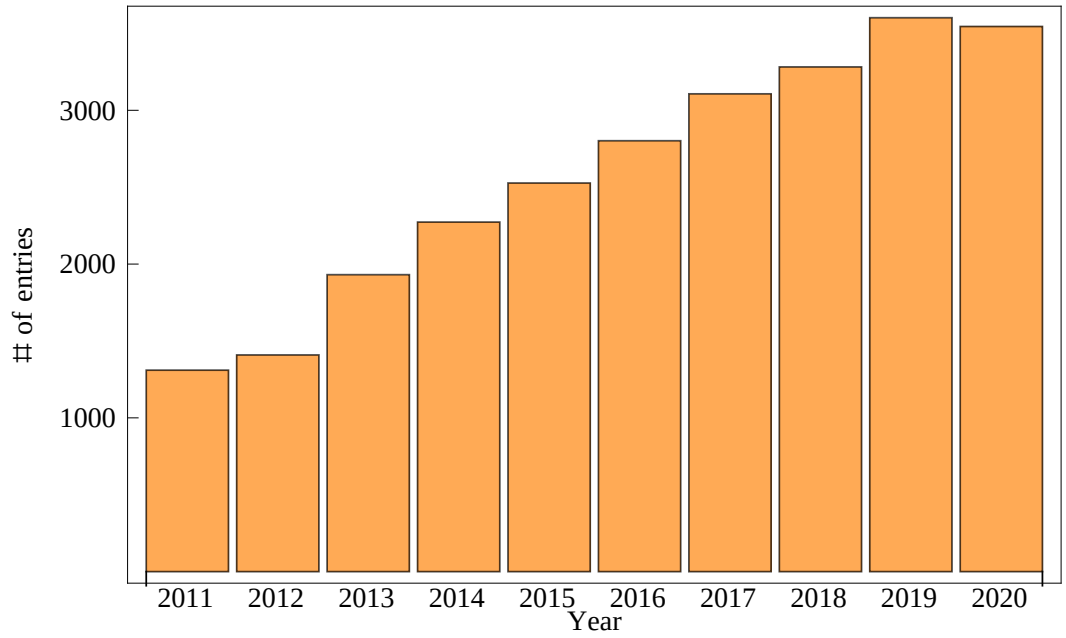

Figure 1.2: "Microwave materials" entries in Web of Science.

is limited by spurious mixing signals (termed "passive intermodulation", PIM) that arise from signal distortions in nonlinear components [Sta80]. These mixing signals can fall in a neighboring band, a phenomenon called adjacent channel cross talk.

The trouble of PIM becomes more prominent with the order of magnitudes in power that needs to be covered. For instance, cell phone base stations typically transmit 40 dBm, while the received signal coming from a cell phone is only in the range of a −110 dBm. Thus, the base station needs to handle signals with a difference of about 15 orders of magnitude. Here, even tiny nonlinearities can lead to significant PIM, which in turn results in apparently occupied channels, a smaller coverage or a loss of data rate due to an increased bit error rate. Tests have revealed an approximate 18 % drop in download speed when the PIM level increases from −125 dBm to −105 dBm [TW16]. For current digital standards, no well-defined linearity requirement exists. However, the analogue GSM (2G) standard allowed a maximum PIM level of −112 dBm at 43 dBm input power [HCC09a].

The sources of PIM are diverse [Lui90]. Figure 1.3 illustrates the different sources that have been addressed in literature. PIM is extensively investigated on a device level, which gives rise to instruments with the sole task to characterize PIM [EKS19, Yag16, Bra14]. For example, PIM is a major challenge in microstrip lines [SKS18]. PIM reduction has been achieved by using high permittivity coatings to mitigate locally enhanced electric fields at the fringed etched edges [KSB+20]. Other approaches include canceling of PIM with another PIM source [JGHB20]. A different approach even uses liquid metal antennas to avoid active tuning, as active devices generally result in much larger PIM than solely passive ones [WKSA18].

To mitigate PIM on a more fundamental level, it is necessary to investigate the

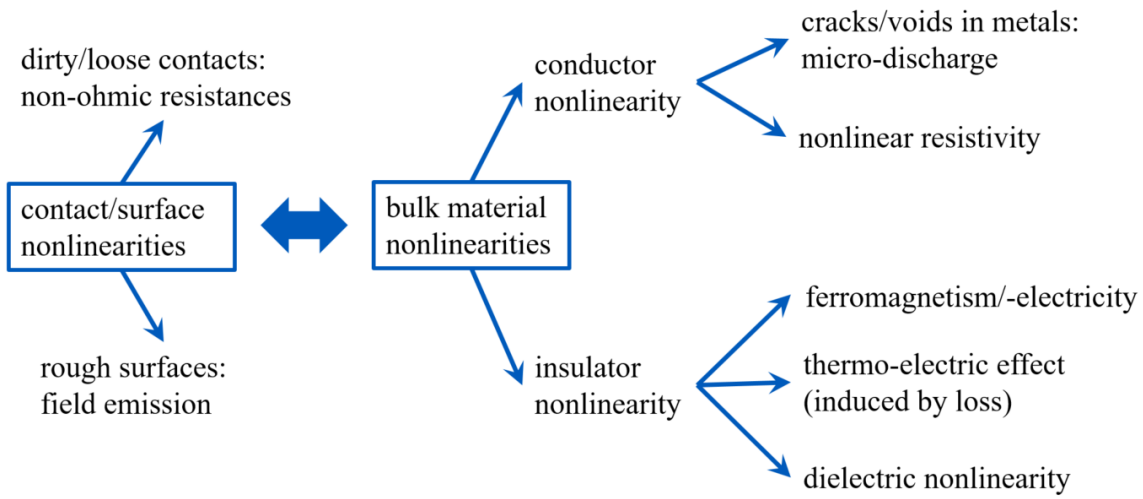

Figure 1.3: Overview of PIM sources as collected in [Sta80] and [Lui90], including the thermo-electric effect from [WKGS15].

mechanisms collected in Figure 1.3 separately. However, the dielectric nonlinearity remains a property that is hardly accessible in an isolated manner. The authors of [NIH88] were the first to isolate and characterize their sintered ceramics' nonlinear dielectric response [THNW89], which allowed them to use their sintered ceramics for cross talk reduced filters for cellular base stations [ITNW92]. Since so little data is available on dielectric nonlinearities in the microwave range, the description of the microscopic origins is limited to vague conjectures, e.g. electrostriction in [Sta80] and nonlinear phonons in [THNW89].
Nevertheless, tackling the challenge of dielectric nonlinearities in the microwave range can profit from related fields that have already been studied more extensively. Figure 1.4 puts these topics into context by overlapping adjacent fields of science that share common qualities. The fields of microwave dielectrics and PIM have already been mentioned above. Although dielectric nonlinearities have been sparsely examined at microwave frequencies so far, they have indeed been studied intensively at optical frequencies in the

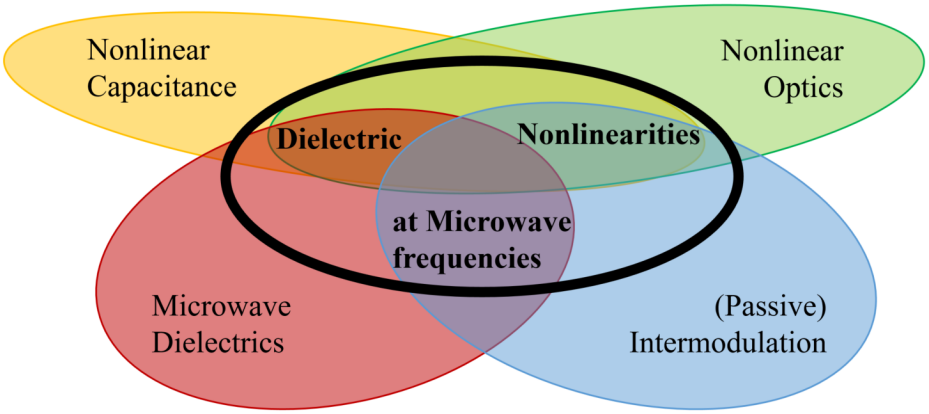

Figure 1.4: Topic of this work with its adjacent fields.

broad field of nonlinear optics [Boy08, BCD18] and in terms of nonlinear capacitance at low frequencies [JACJ+19]. Further adjacent fields are ferroelectrics, which naturally show a large nonlinear susceptibility [MDK11], and the nonlinear susceptibility of polar liquids [Ric17]. At optical frequencies, lasers easily enable high electric field amplitudes, where nonlinear dielectric responses become relevant. Despite the recent advent of continuous wave masers [BSS+18], high power phenomena are still difficult to investigate at microwave frequencies. As losses in the microwave range are orders of magnitudes larger than in optics, large microwave power dissipation gives rise to effects which are much more dominant than the nonlinear response. However, the emergence of low loss microwave dielectrics opens the field of nonlinear microwave dielectrics.
Hence, the aim of this work is the characterization of the dielectric nonlinearity of glasses and glass-ceramics at microwave frequencies. Furthermore, the connection between the macroscopic nonlinearity and the microscopic material structure is investigated to identify nonlinear mechanisms.

Chapter 2

Background

2.1 Material Classes

This section introduces the material classes that are investigated in this work, glasses and glass-ceramics. Basic physical properties are discussed together with an overview of the manufacturing process.

2.1.1 Glasses

The term "glass" refers to a special class of amorphous solids. Their atomic structure resembles that of a liquid in the sense of lacking a long-ranged order. On the other hand, they exhibit elastic properties like a solid [Pfa97]. It is helpful to observe the formation process of a glass to understand this material class better. Figure 2.1 sketches a solidification process of a liquid in a volume-temperature diagram.
Generally, the volume decreases together with the temperature. If the cooling happens sufficiently slowly (on a longer time scale than the atomic diffusion), there is a discontinuous phase transition at the melting temperature T_m. A glass is obtained by cooling on a smaller time scale than the atomic diffusion. This process accounts for the description of a glass as an "undercooled liquid" [Sch88]. Thermodynamically speaking, the glass is in a metastable state, because a state with a higher vibrational entropy exists at the temperature of concern. However, the classical terms of equilibrium thermodynamics do not apply to the out-of-equilibrium system "glass". Higher cooling rates result in a lower density glass. In contrast to the crystallization, the glass transition does not take place at a single temperature but rather in a certain range, which makes the glass transition temperature an interval. Even more so, the interval is dependent on the cooling rate. This is illustrated by the different glass transition temperatures T_{g_s} and T_{g_f}.
In theory, all atomic matter can form a glass, though the formation is practically limited by the cooling rate. Nevertheless, even metals have been shown to form glasses at sufficient cooling rates [Gre95].

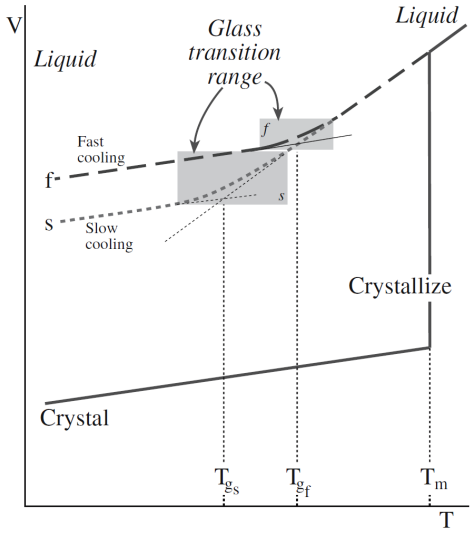

Figure 2.1: Sketch of the temperature dependency of the volume for crystal formation (solid line) and glass formation (dashed lines) [CN+07].

2.1.2 Glass-Ceramics

The term "glass-ceramic" refers to a polycrystalline solid that has been obtained by controlled crystallization of a glass [CN+07]. It therefore differs from a sintered ceramic in its manufacturing process. The term "controlled" distinguishes the crystallization from spontaneous crystallization (called "devitrification"). The base glass is also termed "green glass".

As discussed in subsection 2.1.1, a glass is in a metastable state. Under appropriate heat treatment, it can be transformed into a thermodynamically more favorable, crystalline state. This treatment of controlled partial crystallization is called "ceramization". The ceramization process consists of two steps [Pfa97]. The first step is the formation of stable crystallization nuclei. In the second step, crystallites start to grow from those nucleation sites.

Even though the crystalline phase has a favorable free enthalpy compared to the glass phase, the formation of crystallites is also associated with a surface that requires energy [Vog92]. The free enthalpy is proportional to the crystallite volume $\Delta G_V \sim r^3$ while the free enthalpy of the surface is proportional to the area $\Delta G_S \sim r^2$. At some threshold radius r_0 the drop in free enthalpy of the volume dominates the gain in free enthalpy of the surface tension.

Ceramized glasses differ from devitrified glasses by higher nucleation rates, a homogeneous distribution of crystallites and a uniform crystallite size [McM79].

The nucleation rate is more or less proportional to the diffusion coefficient [CN+07]. Furthermore, the diffusion constant is proportional to the temperature and inversely proportional to the viscosity [Ein05]. As the viscosity can increase after nucleation, the growth needs to be supported by higher temperatures. The resulting typical temperature process to produce a glass-ceramic is shown in Figure 2.2.

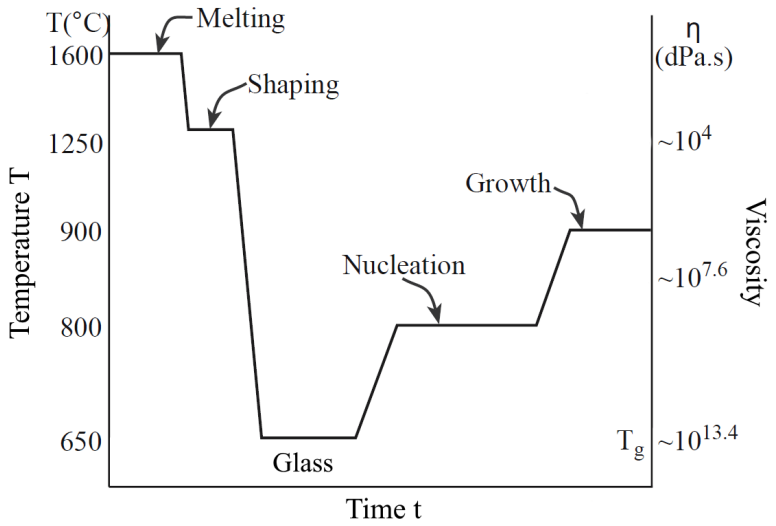

Figure 2.2: Sketch of the temperature profile to obtain a glass-ceramic [CN+07]. At the glass stage, the process can be interrupted and cooled down far below the glass transition temperature T_g to ambient temperature.

2.2 Macroscopic Dielectric Properties

This section introduces the necessary concepts for the description of dielectrics. Besides the permittivity and the loss, this includes the description of the macroscopic electric field in a dielectric. Finally, different notations for nonlinear dielectric responses are compared, as this is the central quantity that this work aims to measure and describe.

2.2.1 Relative Permittivity

An electric field $\mathbf{E}$ acting upon a dielectric causes the local displacement of charges. This displacement of charges is summarized in the macroscopic polarization $\mathbf{P}$. The susceptibility χ is the macroscopic material property that connects these two fields [Jac99]:

$$\mathbf{P} = \varepsilon_0 \chi \mathbf{E} \tag{2.2.1}$$

Here, ε_0 is the vacuum permittivity. The sum of the polarization $\mathbf{P}$ and the electric field $\mathbf{E}$ is the electric displacement field $\mathbf{D} = \varepsilon_0 \mathbf{E} + \mathbf{P}$. It defines the relative permittivity $\varepsilon = \chi + 1$:

$$\mathbf{D} = \varepsilon_0 \varepsilon \mathbf{E} \tag{2.2.2}$$

However, the relation in Equation 2.2.1 is subject to several assumptions. First, it is generally time dependent:

$$\mathbf{P}(t) = \varepsilon_0 \int_{-\infty}^{t} \chi(t - t') \, \mathbf{E}(t') \, dt' \tag{2.2.3}$$

It depends on the previous history of $\chi(t)$ and $\mathbf{E}(t)$. Equation 2.2.1 assumes that the displacement of charges follows the applied electric field instantaneously, expressed by $\chi(t-t') = \chi\,\delta(t-t')$ with $\delta(t)$ representing the Dirac delta distribution. As Equation 2.2.3 is a convolution $\chi * E$, it is convenient to take the Fourier transform $\mathcal{F}\{\chi * E\}$ and apply the convolution theorem $\mathcal{F}\{f * g\} = \mathcal{F}\{f\}\mathcal{F}\{g\}$:

$$\mathbf{P}(\omega) = \varepsilon_0 \chi(\omega)\mathbf{E}(\omega) \tag{2.2.4}$$

The susceptibility $\chi(\omega)$ is a complex quantity. The imaginary part, which is usually much smaller than the real part for dielectrics, corresponds to a loss. It is discussed in subsection 2.2.3.
Equation 2.2.1 furthermore tacitly assumed that the polarization $\mathbf{P}$ points into the same direction as the applied electric field $\mathbf{E}$. This is not necessarily the case. Promoting the susceptibility χ to tensor eliminates this restriction:

$$P_i = \varepsilon_0 \sum_j \chi_{ij} E_j \tag{2.2.5}$$

Here, P_i and E_i correspond to the ith component of $\mathbf{P}$ and $\mathbf{E}$, respectively.

2.2.2 De-electrification Field

An external electric field $\mathbf{E}_{ext}$ induces a surface polarization in a dielectric [Kit73]. In return, this polarization gives rise to an opposing electric field inside the dielectric, the de-electrification field $\mathbf{E}_{del}$. The resulting electric field is labeled $\mathbf{E}_{mac}$, the macroscopic electric field:

$$\mathbf{E}_{mac} = \mathbf{E}_{ext} - \mathbf{E}_{del} = \mathbf{E}_{ext} - N\frac{\mathbf{P}}{\varepsilon_0} \tag{2.2.6}$$

Here, N is the geometry dependent de-electrification factor. Together with the definition $\mathbf{P} = \varepsilon_0 \chi \mathbf{E}_{mac}$ this gives:

$$\mathbf{P} = \frac{\chi\varepsilon_0}{1 + N\chi}\mathbf{E}_{ext} \tag{2.2.7}$$

Three examples for the de-electrification factor N are: $N = 1$ if all field lines penetrate the surface perpendicular to the surface, as in a thin dielectric sheet like a classic capacitor, $N = 1/3$ for a sphere, and $N = 0$ if the field lines are parallel to the surface. Hence, the macroscopic electric fields for these geometries are:

$$\mathbf{E}_{mac} = \frac{1}{1 + N(\varepsilon_r - 1)}\mathbf{E}_{ext} = \begin{cases} (1/\varepsilon_r)\ \mathbf{E}_{ext} & \text{for } N = 1 \\ 3/(\varepsilon_r + 2)\ \mathbf{E}_{ext} & \text{for } N = 1/3 \\ \mathbf{E}_{ext} & \text{for } N = 0 \end{cases} \tag{2.2.8}$$

An external electric field parallel to a surface between two dielectrics extends continuously, while a perpendicular electric field is discontinuous.

2.2.3 Dielectric Loss

The quantities $\chi(\omega)$ and $\varepsilon(\omega)$ introduced in subsection 2.2.1 are complex quantities. However, the imaginary part is much smaller than the real part for low loss dielectrics. It is therefore convenient to state the real and the imaginary part as a magnitude ε_r and an angle δ [KG86]:

$$\varepsilon = \varepsilon' + i\ \varepsilon'' = \varepsilon'(1 + i\ \varepsilon''/\varepsilon') = \varepsilon_r(1 - i\ \tan\delta) \tag{2.2.9}$$

Here, $\tan\delta$ is the imaginary part of the permittivity normalized to its real part:

$$\tan\delta = -\frac{\mathrm{Im}(\varepsilon)}{\mathrm{Re}(\varepsilon)} \tag{2.2.10}$$

The loss corresponds to an AC-conductivity σ by [Hun09]

$$\sigma = \varepsilon_0\varepsilon_r\omega\ \tan\delta. \tag{2.2.11}$$

For comparability with quality factors of resonators (see subsection 3.2.3), it is common to use the inverse of the loss tangent $\tan\delta$, the dielectric quality factor:

$$Q_d = 1/\tan\delta \tag{2.2.12}$$

The notations for dielectric loss are completed by the extinction coefficient κ defined by $I = I_0\ e^{-2\kappa z}$. Here, I is the intensity of a wave after traveling for the length z through the lossy dielectric. The extinction coefficient κ is related to the loss tangent $\tan\delta$ via

$$\tan\delta = \frac{\lambda}{2\pi}\kappa \tag{2.2.13}$$

Here, λ is the wavelength in the dielectric. The extinction coefficient κ is the common measure for dielectric loss at optical frequencies. Typical extinction coefficients in optical fibers of $\sim 10\,\mathrm{dB/km}$ [KH66] result in much smaller losses in the order of $\sim \tan\delta \approx 10^{-10}$ than usually observed in the microwave range.

2.2.4 Perturbative Nonlinear Dielectric Responses

Equation 2.2.1 is a linear relation. A standard phenomenological approach to include nonlinear responses is their treatment as a perturbation. The perturbation assumes that the polarization $\mathbf{P}$ can be written in terms of a power series expansion of $\mathbf{E}$. Even though this is a very appealing approach, it has a limited validity due to the radius of convergence of the power series expansion (see section 2.3). The most general formulation of this perturbation approach is the tensor expansion as in Equation 2.2.5 [Bö73]:

$$P_i/\varepsilon_0 = \sum_j \chi_{ij}E_j + \sum_{jk} \chi_{ijk}E_jE_k + \sum_{jkl} \chi_{ijkl}E_jE_kE_l + ... \tag{2.2.14}$$

χ_{ij} is the linear susceptibility that can account for anisotropy while the following terms χ_{ijk} and χ_{ijkl} also take into account anisotropic nonlinearities. For isotropic materials, Equation 2.4.3 can be simplified considerably. Isotropy imposes high requirements on the susceptibility tensors: All off-diagonal elements vanish and the remaining diagonal elements are equal to each other. Furthermore, reversing the electric field **E** should also reverse the polarization **P**:

$$\mathbf{E}(t) \rightarrow -\mathbf{E}(t) \overset{!}{\Rightarrow} \mathbf{P}(t) \rightarrow -\mathbf{P}(t) \tag{2.2.15}$$

This implies that all even order terms of **E** vanish. Taking into account these implications of isotropy, Equation 2.4.3 can be written as a scalar equation:

$$P/\varepsilon_0 = \chi_1 E + \chi_3 E^3 + \chi_5 E^5 + ... \tag{2.2.16}$$

Here, P and E denote the amplitudes of the vectors **P** and **E**, respectively.
While the linear susceptibility χ_1 is certainly isotropic for glasses and glass-ceramics, it is generally unwary to assume the same for the nonlinear susceptibilities without the knowledge of the nonlinear mechanism. For instance, if the nonlinearity turned out to be mainly due to surface effects, the symmetry is broken. Nevertheless, for a large number of nonlinear dipoles in a homogeneous and isotropic medium, it is reasonable to assume that the nonlinear polarizabilities are distributed homogeneously and hence isotropically as well.
Depending on the problem, it is appropriate to rewrite the linear and the nonlinear susceptibilities. Besides the susceptibility χ, two other notations are common for linear responses: the relative permittivity $\varepsilon_r = \chi + 1$ and its square root, the refractive index $n = \sqrt{\varepsilon_r}$ (assuming $\mu_r = 1$). The relative permittivity is usually preferred at static fields, as it constitutes the ratio by which the de-electrification field reduces the electric field in the dielectric. In optics, the refractive index is commonly preferred because it directly gives the ratio of the speed of light in vacuum and the medium. Equivalently, analogous notations are adopted for the third order nonlinear responses:

- the nonlinear susceptibility χ_3, which already has been introduced in Equation 2.2.16,
- the nonlinear refractive index n_2, defined by $n(I) = n_0 + n_2 I$, with I being the beam intensity [Boy08],
- the change in the permittivity $\Delta\varepsilon_r$, which is given by $D(E) = \varepsilon_0 \ (\varepsilon_{r,E=0} + [\Delta\varepsilon_r/E^2]E^2) \ E$ [Bö73].

The two notations χ_3 and $\Delta\varepsilon_r/E^2$ are both given in $\mathrm{m}^2/\mathrm{V}^2$, while n_2 is usually given in cm^2/W. Actually, the notations χ_3 and $\Delta\varepsilon_r/E^2$ are equivalent to each other. The nonlinear refractive index n_2 can be related to the other notations by:

$$n_2 = \frac{1}{n_0^2 \varepsilon_0 c} \ \chi_3 \tag{2.2.17}$$

Besides those notations, it is sometimes convenient to normalize the absolute change in the permittivity to the relative permittivity. Following [THNW89], it is labeled α:

$$\alpha = \frac{\Delta\varepsilon_r}{\varepsilon_{r,E=0}\ E^2} = \frac{\chi_3}{\varepsilon_{r,E=0}} \tag{2.2.18}$$

2.3 Nonlinear Signal Theory

The general aim of this section is to compare different approaches to describe the frequency response of nonlinearities. The discussion relies on the experience of two fields: Nonlinear microwave circuits in engineering [Maa03, PC03] and nonlinear optics in physics [Boy08]. The general task is to relate an input signal $x(t)$ and an output signal $y(t)$. In nonlinear microwave circuits, the approaches separate into two classes: Time and frequency domain analysis. Time-domain analysis takes the differential equations of the nonlinear circuit and solves them in a transient numerical way. The main drawback of this method is that components are usually best characterized in the frequency domain [Maa03]. In frequency-domain analysis, three options are to be considered: Harmonic Balance Analysis, Volterra Series Analysis and analysis by a power series expansion. The Volterra Series Analysis is also a power series; however, it includes memory kernels.
In nonlinear optics, there are mainly two approaches: for resonant systems, a two-level (or few-level) approximation can be made. For non-resonant systems, the perturbative power series expansion approach is commonly relied on.
This section focuses on relations of $x(t)$ and $y(t)$ that can be represented as a function $y(x)$ in the mathematical sense: every input amplitude is assigned to exactly one output amplitude. In other words, the output amplitude depends solely on the present input amplitude. In particular, this approach excludes memory effects:

$$x(t) \overset{y(x)}{\rightarrow} y(t) = y(x(t)) \tag{2.3.1}$$

Typical problem settings require to find one out of $x(t)$, $y(t)$ and $y(x)$ with the knowledge of the other two. The following discussion is restricted to odd[1] nonlinear responses $y(x)$ (see Equation 2.2.15). Even though the third order nonlinear responses, which are in the focus of this work, actually allow four wave mixing [Boy08], the following scope is restricted by dealing with input signals consisting of only two frequencies. This is motivated by microwave engineering, were a two-tone signal is a classic method to detect nonlinear responses.

$$x(t) = A_1 \sin(\omega_1 t) + A_2 \sin(\omega_2 t) \tag{2.3.2}$$

Here, A_i are the amplitudes at the respective frequencies ω_i. Without loss of generality, $\omega_2 > \omega_1$ is assumed from now on. Furthermore, the frequencies are assumed to be

[1] An odd function exhibits inversion symmetry at the origin, $y(-x) = -y(x)$.

closely spaced $\omega_2 - \omega_1 \ll \omega_1$, which means that the nonlinear system reacts to both frequencies in the same manner. Applying this signal to the nonlinear response function $y(x)$ results in a signal of the form:

$$y(t) = \sum_{m+n>0}^{\infty} B_{mn} \sin[(m\omega_1 + n\omega_2)t] \tag{2.3.3}$$

The natural multiples of the original frequencies are called harmonics. The mixing frequencies of two frequencies are referred to as intermodulations. The most relevant frequencies for this work will be labeled $B_1 = B_{1,0}$, $B_2 = B_{0,1}$, $B_{\mathrm{H3,1}} = B_{3,0}$, $B_{\mathrm{H3,2}} = B_{0,3}$, $B_{\mathrm{IM3+}} = B_{-1,2}$, and $B_{\mathrm{IM3-}} = B_{2,-1}$:

$$\begin{aligned} y(t) = {} & B_1 \sin(\omega_1 t) + B_2 \sin(\omega_2 t) \\ & + B_{\mathrm{H3,1}} \sin(3\omega_1 t) + B_{\mathrm{H3,2}} \sin(3\omega_2 t) \\ & + B_{\mathrm{IM3+}} \sin((2\omega_2 - \omega_1)t) \\ & + B_{\mathrm{IM3-}} \sin((2\omega_1 - \omega_2)t) \\ & + \ldots \end{aligned} \tag{2.3.4}$$

The more specific aim of this section is the calculation of the input power dependency of the intermodulation level; that is to find the amplitude at the (upper) third order intermodulation product $B_{\mathrm{IM3+}}$ as a function of the input amplitudes of the two signals A_1 and A_2. Figure 2.3 sketches the resulting spectrum if a nonlinear system is exited with a two-tone signal as in Equation 2.3.2.

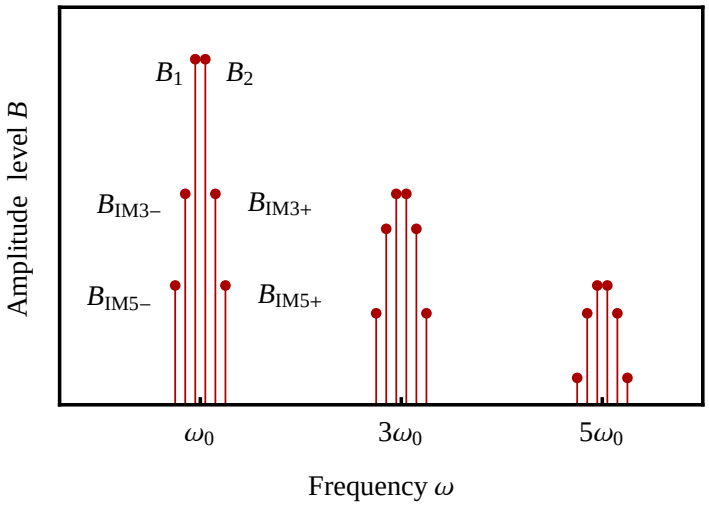

Figure 2.3: A spectrum of a two-tone signal that has been distorted by a nonlinearity. The sketch shows distortion products up to the fifth order.

2.3.1 Perturbative Intermodulation Generation

A common approach in both electrical engineering [Maa03] and nonlinear optics [Boy08] is the description of a nonlinear response as a power series expansion. The response function is assumed to be of the form:

$$y(x) = a_0 + a_1 x + a_2 x^2 + a_3 x^3 + ... \tag{2.3.5}$$

As discussed in subsection 2.2.4, the even order terms disappear for odd functions:

$$y(x) = a_1 x + a_3 x^3 + a_5 x^5 + ... \tag{2.3.6}$$

Applying the two-tone signal from Equation 2.3.2 to this response function leads to intermodulation products at $m + n =$ odd. Truncating the power series after the ith term leads to frequencies products with $m + n \leq i$. For the sake of clearness, only the original frequency components ω_1 and ω_2 and their third harmonics are shown, together with two of their third order intermodulations, $2\omega_2 - \omega_1$ and $2\omega_1 - \omega_2$:

$$\begin{aligned}
y(t) = &\left[a_1 A_1 + a_3\left(\frac{3}{4}A_1^3 + \frac{3}{2}A_1 A_2^2\right) + a_5\left(\frac{5}{8}A_1^5 + \frac{15}{4}A_1^3 A_2^2 + \frac{15}{8}A_1 A_2^4\right)\right] \sin(\omega_1 t) \\
&+ \left[a_1 A_2 + a_3\left(\frac{3}{4}A_2^3 + \frac{3}{2}A_1^2 A_2\right) + a_5\left(\frac{5}{8}A_2^5 + \frac{15}{4}A_1^2 A_2^3 + \frac{15}{8}A_1^4 A_2\right)\right] \sin(\omega_2 t) \\
&+ \left[\frac{3}{4}a_3 A_1^2 A_2 + a_5\left(\frac{5}{4}A_1^4 A_2 + \frac{15}{8}A_1^2 A_2^3\right)\right] \sin[(2\omega_1 - \omega_2)t] \\
&+ \left[\frac{3}{4}a_3 A_1 A_2^2 + a_5\left(\frac{5}{4}A_1 A_2^4 + \frac{15}{8}A_1^3 A_2^2\right)\right] \sin[(2\omega_2 - \omega_1)t] \\
&- \left[\frac{1}{4}a_3 A_1^3 + a_5\left(\frac{5}{16}A_1^5 + \frac{5}{4}A_1^3 A_2^2\right)\right] \sin(3\omega_1 t) \\
&- \left[\frac{1}{4}a_3 A_2^3 + a_5\left(\frac{5}{16}A_2^5 + \frac{5}{4}A_1^2 A_3^2\right)\right] \sin(3\omega_2 t) \\
&+ ...
\end{aligned} \tag{2.3.7}$$

For $a_5 A^2 \ll a_3$ and $a_3 A^2 \ll a_1$, the amplitudes at the selected frequencies become much simpler:

$$\begin{aligned}
B_i &= a_1 \ A_i \\
B_{\mathrm{IM3+}} &= \frac{3}{4} \ a_3 \ A_1 A_2^2 \\
B_{\mathrm{IM3-}} &= \frac{3}{4} \ a_3 \ A_1^2 A_2 \\
B_{\mathrm{H3},i} &= \frac{1}{4} \ a_3 \ A_i^3
\end{aligned} \tag{2.3.8}$$

The power series approach allows several insights: It produces the frequencies at which amplitudes different from zero are expected and it can - in theory - be extended to infinite input frequencies. It furthermore relates the order of nonlinearity a_i to the

frequency components. For instance, the fifth order nonlinearity a_5 has a contribution at third order frequency components $2\omega_2 - \omega_1$ and $2\omega_1 - \omega_2$.

Equation 2.3.8 motivates the classical expectation of intermodulation in weakly nonlinear systems: the linear components B_i rise linearly with its corresponding input amplitude A_i and the harmonics and intermodulation amplitudes rise with the third power of the input amplitude, $A_i A_j^2 \sim A^3$. In the logarithmic dB representation, all power-laws become a straight line. This straight line has a slope of 1 dB/dB for the linear relation and a slope of 3 dB/dB for the cubic dependency of the intermodulation amplitude. The term "level" refers to this logarithmic representation (e.g. power level and amplitude level):

$$A[\mathrm{dB}] = 20 \log_{10}(A) \tag{2.3.9}$$

The logarithmic representation is also used to give a figure of merit for the nonlinearity of a device, the third order intercept point IP3. It is the intersection of the linear response with a slope of 1 dB/dB and the intermodulation response with slope 3 dB/dB. The point is given by the pair (IIP3,OIP3), the input power level and the corresponding output power level. The same definition can be extended to higher order intermodulations, e.g. IP5. Fifth order intermodulations exhibit a 5 dB/dB slope. Figure 2.4 sketches the idealized intermodulation behavior of a nonlinear device.

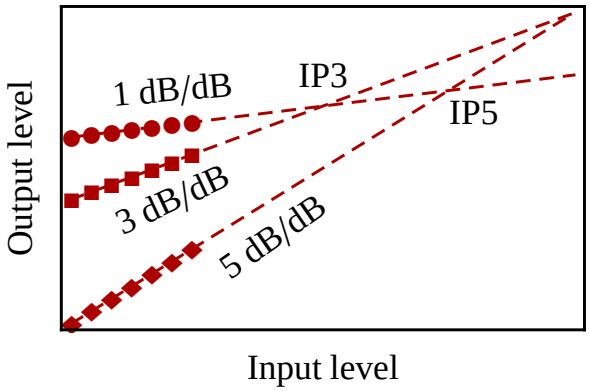

Figure 2.4: Graphical definition of IP3 and IP5.

However, the power series approach is only applicable as long as the power series converges [DP99, Boy08, PC03]. This restriction is obvious for non-analytic functions[2]. However, there are smooth functions (infinitely differentiable, all derivatives are continuous) where the power series expansion converges only within a finite radius. Examples of such functions are discussed in subsection 2.3.5. Even before the convergence limit, the amplitude terms may become ridiculously inflated with an unwieldy number of free parameters a_i. To conclude, the power series approach is applicable within a sufficient small amplitude range, and even then only for analytic response functions.

[2] A function is analytic if it is *locally* given by a convergent power series.

2.3.2 Harmonic Fourier Coefficient Method

The Harmonic Fourier Coefficient Method relies on the fact that any periodic function can be obtained by adding harmonically related sinusoids. This method is not limited to any convergence of a power series. Therefore, it is even applicable to non-analytic functions[3] (see subsection 2.3.5). This method has been applied to explain intermodulation behavior in high temperature superconductors [DS99]. However, in contrast to the Power Series Expansion Method, it actually only allows the calculation of higher harmonics, not of intermodulations. A signal of the form

$$x(t) = A\ \sin(\omega t) \tag{2.3.10}$$

is applied to a response function $y(x)$. The resulting signal $y(t)$ can be expressed as a sum of sinusoids with their corresponding Fourier coefficients:

$$y(t) = \frac{a_0}{2} + \sum_{k=1}^{\infty}(B_k \sin(k\omega t) + C_k \cos(k\omega t)) \tag{2.3.11}$$

For odd response functions $y(x)$, cosines and even order sines disappear:

$$y(t) = \sum_{k=1,3,5\ldots}^{\infty} B_k\ \sin(k\omega t) \tag{2.3.12}$$

The Fourier coefficient B_k at the frequency of interest is classically obtained via:

$$B_k = \frac{1}{\pi}\int_{-\pi}^{\pi} \mathrm{d}\varphi\ y(x(\varphi))\ \sin(k\varphi) \tag{2.3.13}$$

Here, the substitution $\varphi = \omega t$ was used to eliminate the specific time and frequency dependency. The third harmonic amplitude is just the Fourier coefficient at $k = 3$, $B_{\mathrm{H3}} = B_3$. The integral in Equation 2.3.13 does not necessarily need to have an analytic solution. Still, this method allows the numerical calculation of the third harmonic amplitude. However, it is not generally possible to apply this method to calculate intermodulation amplitudes.

2.3.3 Harmonic Balance Analysis

While the perturbative approach discussed in subsection 2.3.1 finds application in small nonlinear systems, Harmonic Balance Analysis constitutes a more generally applicable method, even incorporating memory effects [Maa03]. It is a frequency domain method to find the steady state response of a nonlinear system. The basic idea is to start with a certain set of frequencies (usually harmonics) and solve for the amplitudes of these frequencies so that the equations of the nonlinear system are sufficiently fulfilled. The concept is extendible to Multitone Harmonic Balance Analysis [Maa03, CMO01].

[3] remaining condition: the function is continuous and derivative square integrable [TS76].

The analysis can start from the nonlinear equation of motion including forth and back Fourier transformation from time to frequency domain and vice versa. However, for the discussion here, the scope is limited to the application of a known nonlinear response function as in Equation 2.3.1. This allows the application of a strongly simplified Multitone Harmonic Balance Analysis: a signal of two frequencies Equation 2.3.2 undergoes a nonlinear transformation. The resulting signal is fitted with a set of frequencies consisting of the original frequencies (2 parameters) and the third order (+6 parameters) and fifth order (+10 parameters) intermodulation frequencies. It becomes clear that this method requires an early truncation to handle the number of parameters. Figure 2.5 depicts a corresponding fit. Here, the effect of the truncation becomes visible: at the larger amplitude, the signal is not appropriately modeled with the underlying set of frequencies.

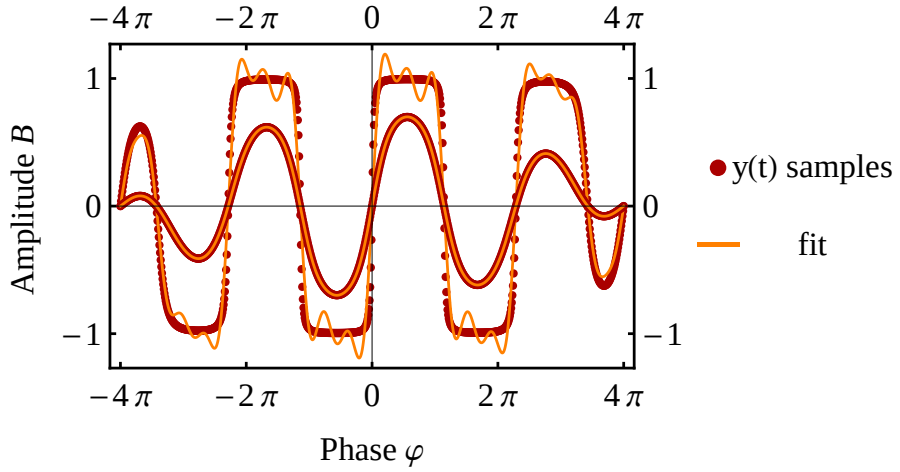

Figure 2.5: Simple Multitone Harmonic Balance Analysis applied to a two-tone signal of the form in Equation 2.3.2 with amplitude $A = 0.5$ and $A = 5$. The figure shows the signal y(t) after nonlinear processing. In this example, the underlying nonlinear response function is the saturable absorber from Equation 2.3.17.

2.3.4 Intermodulation Fourier Coefficient Method

The Harmonic Fourier Coefficient Method can be extended to intermodulations. The author of [Ben33] proposed a Fourier coefficient integral that can be used to calculate intermodulation amplitudes. For IM3+, it is a 2-dimensional integral of the form:

$$B_{\mathrm{IM3+}} = \frac{1}{2\pi^2} \int_{-\pi}^{\pi} \int_{-\pi}^{\pi} \sin(2\varphi_2 - \varphi_1)\; y\Big(A_1 \sin\varphi_1 + A_2 \sin\varphi_2\Big) \mathrm{d}\varphi_1 \mathrm{d}\varphi_2 \qquad (2.3.14)$$

Here, $y(x)$ again represents the nonlinear response function. In principle, this integral is sufficient to calculate the intermodulation amplitudes for a given nonlinear response function $y(x)$ [VdV68, PC03, DP99]. However, this integral generally cannot be solved analytically and the numerical solution of this 2-dimensional integral may become

tedious. Based on the discussion in [WKD99] and [Vel04], a different approach can be taken. It is a 1-dimensional integral of the form:

$$B_{\mathrm{IM3+}} = \frac{1}{u/2} \int_{-u/2}^{u/2} \sin(2\varphi_2 - \varphi_1)\; y\Big(A_1 \sin(\varphi_1) + A_2 \sin(\varphi_2)\Big)\; \mathrm{d}\varphi \tag{2.3.15}$$

The relation between the general variable φ, the input signal frequencies φ_1, φ_2 and the period u need to fulfill a crucial condition to obtain a valid integral: The integrand is required to be periodic. This is only the case for rational ratios of φ_1 and φ_2. In general, signals consisting of at least two frequencies do not need to show a periodicity anymore [Maa03]. However, for nonlinear relations $x(t) \to y(t)$ that can be written as a function $y(x)$, the intermodulation amplitude does not depend on the specific frequency choice[4]. Especially, it does not depend on the ratio of the frequencies. Hence, one can choose φ_1 and φ_2 in a rational ratio without the loss of generality. Furthermore, it is advisable to choose a small denominator, because the period of the integrand increases with increasing denominators of this rational ratio. A larger period with an increasing number of zero crossings requires an increasing sampling and is therefore of disadvantage if the integral is to be solved numerically. Figure 2.6 illustrates this phenomenon.

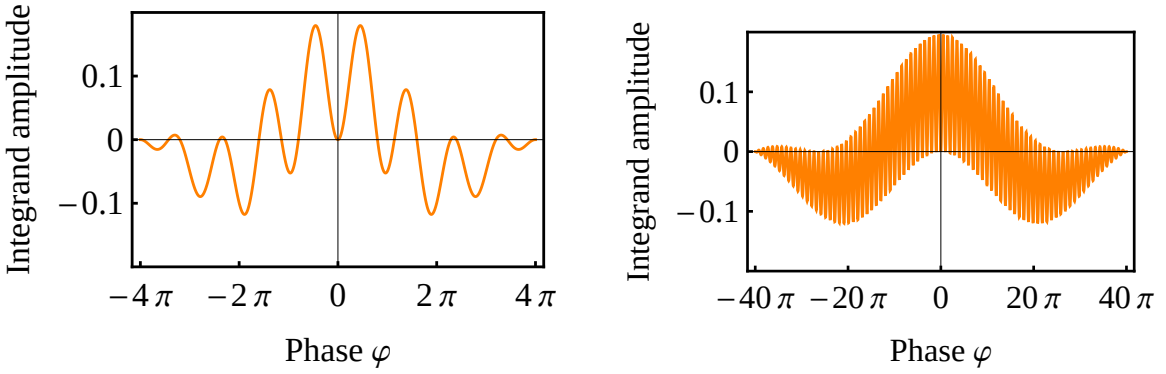

(a) Integrand with $\varphi_1 = \frac{3}{4}\varphi_2$

(b) Integrand with $\varphi_1 = \frac{39}{40}\varphi_2$

Figure 2.6: Integrands for different choices of frequency spacing.

On the other hand, the frequencies cannot be chosen in a deliberately small rational ratio, as they must not be harmonically related to each other. Otherwise, the integral returns the harmonic contributions of the input signal additionally to the intermodulation contribution. Table 2.1 lists small rational ratios of frequencies. The smallest denominator without harmonic relation between the frequencies is 4. The choice of $\varphi_1 = 3\varphi_2/4 = 3\varphi/4$ results in:

$$B_{\mathrm{IM3+}} = \frac{1}{4\pi} \int_{-4\pi}^{4\pi} y\left(A_1 \sin\left(\frac{3}{4}\varphi\right) + A_2 \sin\left(\frac{4}{4}\varphi\right)\right) \sin\left(\frac{5}{4}\varphi\right)\; \mathrm{d}\varphi \tag{2.3.16}$$

[4]This is true for the mechanisms discussed here. Generally, there are PIM mechanisms that depend on the frequency spacing (e.g. thermal IM [WKGS15]).

Table 2.1: List of rational ratios starting from small denominators. The choice $\varphi_1 = \frac{3}{4}\varphi_2$ has the smallest denominators with no harmonic relation between the frequencies.

φ_1	φ_2	$2\varphi_2 - \varphi_1$	u	Relation
$\frac{1}{2}\varphi$	$\frac{2}{2}\varphi$	$\frac{3}{2}\varphi$	$2 \times 2\pi$	φ_3 and φ_2 are harmonics of ω_1
$\frac{2}{3}\varphi$	$\frac{3}{3}\varphi$	$\frac{4}{3}\varphi$	$3 \times 2\pi$	φ_3 is harmonic of ω_1
$\frac{3}{4}\varphi$	$\frac{4}{4}\varphi$	$\frac{5}{4}\varphi$	$4 \times 2\pi$	no harmonic relation
$\frac{4}{5}\varphi$	$\frac{5}{5}\varphi$	$\frac{6}{5}\varphi$	$5 \times 2\pi$	no harmonic relation
$\frac{n-1}{n}\varphi$	φ	$\frac{n+1}{n}\varphi$	$n \times 2\pi$	(general)

A similar intermodulation Fourier coefficient method has been used in [WKD99]. However, the author of [Vel04] remarks that the method made some critical assumptions: First, the authors of [WKD99] use a sum of exponents $\exp(i\omega t)$. The author of [Vel04] argues that instead a sines/cosines representation is necessary for nonlinear problems. Second, the author of [Vel04] argues that the integration for the Fourier coefficient is evaluated over a certain period, but the argument in the integral is not periodic in the chosen period. The author of [Vel04] therefore questions the validity of the results in [WKD99]. The approach presented above compensates for the remarks in [Vel04].
The method presented here is of course still very limited in its application. [PC03] includes a very detailed discussion of more general nonlinear analysis techniques for distortion prediction.

2.3.5 Exemplary Comparisons of Methods

This section discusses the applicability of the previously introduced methods to calculate intermodulation amplitudes $B_{\mathrm{IM3+}}(A_1, A_2)$.

Polynomial
For some functions $y(x)$ the integral in Equation 2.3.16 can be solved analytically. For instance, choosing $f(x) = a_3\ x^3$ returns $B_{\mathrm{IM3+}} = \frac{3}{4}a_3 A_1 A_2^2$. This conforms to the result of the Power Series Expansion Method.

Non-analytic
In contrast to the Power Series Expansion Method, the Fourier Coefficient Method can be applied to non-analytic response functions, e.g. $y(x) = a_2 \operatorname{sgn}(x) x^2$. An analytic solution for a similar problem can be found in [WKD99] though the result has been questioned by [Vel04]. However, the numerical result can be easily calculated for a large amplitude range. Assuming $A := A_1 = A_2$, this results in $B_{\mathrm{IM3+}} \sim A^2$ or in a 2 dB/dB slope. For comparison, the nonlinear response function $y(x) = a_2 x^2$ does not return any amplitude contribution at IM3+. Another example is the cube root function $y(x) = \sqrt[3]{x}$, which leads to a 1/3 dB/dB slope. Figure 2.7 displays the intermodulation amplitudes for those two functions.

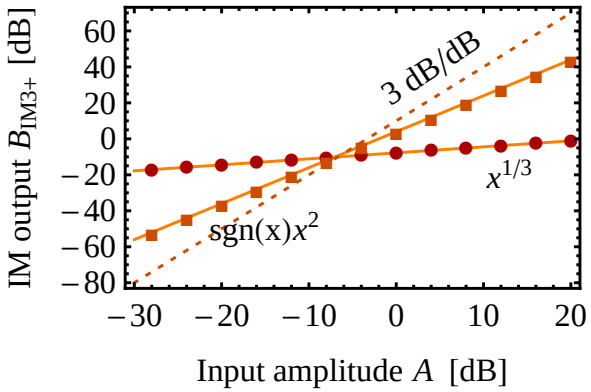

Figure 2.7: Intermodulation amplitude $B_{\mathrm{IM3+}}$ as a function of the input amplitude A for two nonlinear response functions: $y(x) = a_2|x|x$ and $y(x) = \sqrt[3]{x}$. $y(x) = a_2|x|x$ results in a 2 dB/dB slope (squares), $y(x) = \sqrt[3]{x}$ in a 1/3 dB/dB slope (circles).

Limited convergence

This example deals with an intermediate case of the two examples discussed above. It can be locally described by a polynomial, allowing an analytic intermodulation calculation with the Power Series Expansion Method. However, the convergence of the polynomial is limited and the Power Series Expansion Method ceases to be valid. The exemplifying function discussed here is the abstract saturable absorber (for the concrete physical saturable absorber, see subsection 2.4.5). It has the form:

$$y(x) = \frac{x}{\sqrt{1+x^2}} \tag{2.3.17}$$

It is sketched in Figure 2.8a together with some of its truncated power series expansions at $x = 0$. The radius of convergence (RoC) of the power series around $x = 0$ is $x = 1 = 0\,\mathrm{dB}$ [Boy08]. The fifth order power series of this function is:

$$y(x) \approx x - \frac{1}{2}x^3 + \frac{3}{8}x^5 \tag{2.3.18}$$

For low amplitudes, the power series converges. It is therefore expected that the Power Series Expansion Method returns the same results as the more general Fourier Coefficient Method. The Power Series Expansion Method up to the third order returns:

$$B_{\mathrm{IM3+}} = \frac{3}{8}A_1A_2^2 \tag{2.3.19}$$

The third intermodulation level is shown in Figure 2.8b for the Power Series Expansion Method and the Intermodulation Fourier Coefficient Method. As expected, the two methods agree for low amplitudes. However, beyond a certain amplitude, the Power Series Expansion Method does not correctly predict the intermodulation level anymore. Instead, the Intermodulation Fourier Coefficient method predicts a saturating intermodulation level. Furthermore, Figure 2.8 illustrates that simple extension of the power series description to higher order terms does not improve the predictive power of the Power Series Expansion Method.

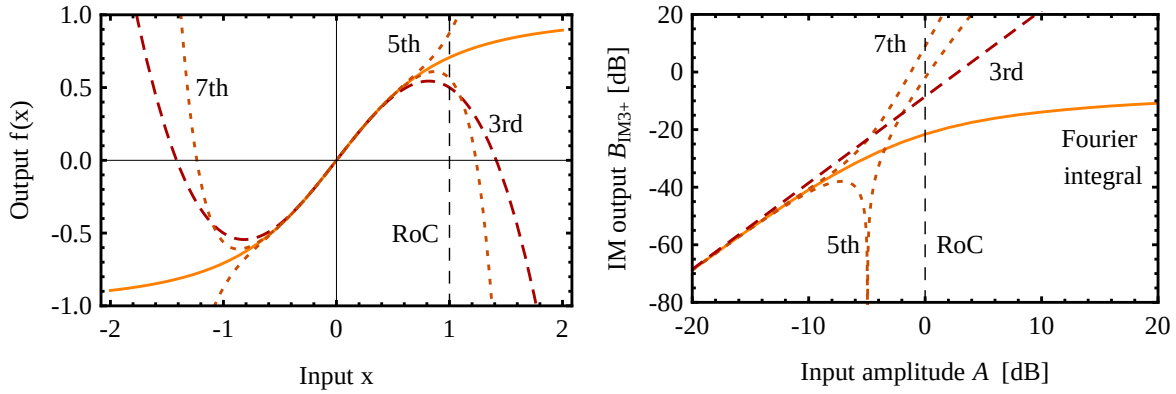

(a) Power series expansions (b) Intermodulation levels

Figure 2.8: Nonlinear response function from Equation 2.3.17 (left) and its intermodulation level as a function of input amplitude (right). RoC marks the radius of convergence ($x_{\mathrm{RoC}} = 1 = 0\,\mathrm{dB}$). For low amplitudes, the power series expansion gives the correct response but diverges from both the function and the intermodulation calculated by the Intermodulation Fourier Coefficient Method. The inclusion of higher order terms does not lead to better agreement.

The example of the saturable absorber is suitable to compare the Harmonic Balance Analysis and the Intermodulation Fourier Coefficient Method. Figure 2.9 shows the intermodulation amplitude level $B_{\mathrm{IM3+}}$ for different computations: Figure 2.9a compares two different numerical integration methods for two different frequency spacing: Numerical Quadrature (NQ) and Monte Carlo (MC)[5]. In the medium amplitude range, all methods agree within numerical precision. For low amplitudes, the Monte Carlo integration fails and deviates from the analytical perturbation solution, while the Numerical Quadrature conforms to the analytical solution. However, the low power range is not of interest because analytical perturbation descriptions exist. At the high amplitude end, all methods show similar qualitative behavior. However, they produce significantly different results. For smaller frequency spacing, the Numerical Quadrature becomes unstable at smaller amplitudes than for larger frequency spacing. This is likely to be explained by the geometry of the integral (see Figure 2.6). The Monte Carlo integration seems continuing being stable. However, the different frequency spacing return distinguishable intermodulation amplitudes as well.

Figure 2.9b compares the Monte Carlo integration to the Harmonic Balance Analysis. The Harmonic Balance Analysis is performed on the basis of all third order intermodulation frequencies (HB3) and then also including all fifth order intermodulation frequencies (HB5). As visible in Figure 2.9b, the inclusion of the fifth order intermodulation frequencies does not lead to a visible change.

As the Monte Carlo integration fails at low amplitudes, they are only compared at intermediate and high amplitudes. They agree in the intermediate amplitude range within numerical precision. At high amplitudes, they deviate from each other, though

[5]For NQ, the *Mathematica* default function `NIntegrate` was used, for MC the `QuasiMonteCarlo` option.

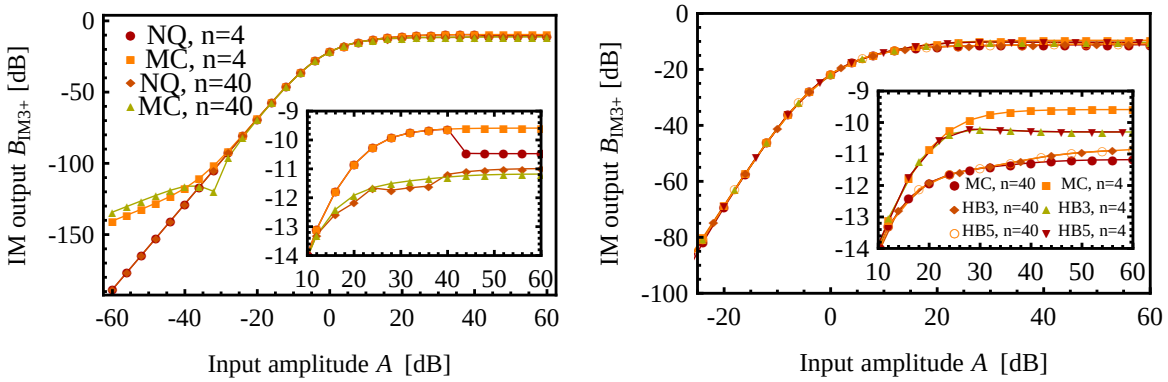

(a) Numeric Quadrature (NQ) and Monte Carlo (MC) integration of Equation 2.3.16.

(b) Fourier Coefficient Integral with MC integration and simple Harmonic Balance (HB).

Figure 2.9: Comparison of methods to predict the input amplitude dependency of the intermodulation amplitude. n is the denominator of the frequency ratio, see Table 2.1. Hence, $n = 40$ corresponds to close frequency spacing, $n = 4$ to far frequency spacing.

the first distinction is due to the frequency spacing while Monte Carlo integration and Harmonic Balance still agree. Only at even higher amplitudes, the Harmonic Balance Analysis deviates from the Monte Carlo integration. It is supposed that the Harmonic Balance Analysis does not include sufficient terms to model the distorted signal at high amplitudes accurately (see Figure 2.5).

Still, the major discrepancy is due to the choice of the frequency spacing. For the frequency spacing $\varphi_1 = \frac{3}{4}\varphi_2$, an 11th order intermodulation coincides with the upper third order intermodulation ($7\varphi_1 - 4\varphi_2 = 7 \cdot 3\varphi - 4 \cdot 4\varphi = 5\varphi$). This gives an additional unwanted contribution to the integrand. In summary, the prediction of the discussed methods should not be applied beyond the intermediate amplitude range, i.e. only within the saturation of the intermodulation level and not in the range when the signal is already saturated. As long as they agree, the methods allow the determination of intermodulation levels beyond the analytical perturbative Power Series Expansion Method.

Inverse polynomial

This example is a special of case of limited convergence. It shows the critical differences that the choice of modeling nonlinear circuits can make. The nonlinear response function $y(x)$ shall be given by the implicit equation:

$$x = y(x) + a\ y(x)^3 \tag{2.3.20}$$

Its explicit form is:

$$y(x) = \frac{2\sqrt[3]{3} - \sqrt[3]{2}\left(\sqrt{81a\ x^2 + 12} - 9\sqrt{a}\ x\right)^{2/3}}{6^{2/3}a\ \sqrt[3]{\sqrt{81a\ x^2 + 12} - 9a^2\ x}} \tag{2.3.21}$$

Again, the convergence of the power series of this nonlinear response function is limited.

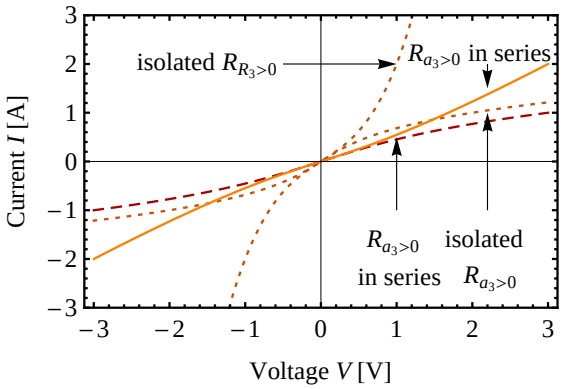

(a) Nonlinear response functions of the different nonlinear resistors in series and isolated circuits.

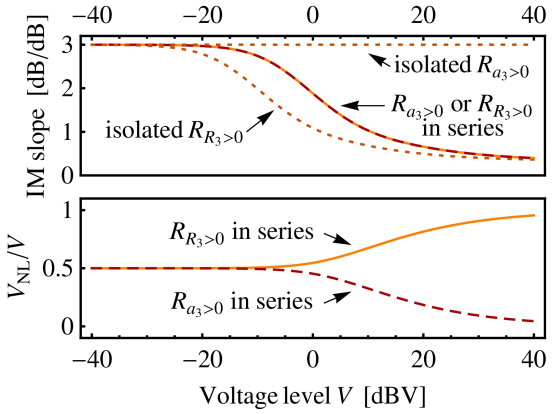

(b) Top: Intermodulation slope of the different circuits. Bottom: Voltage share of the nonlinear resistor.

Figure 2.10: Nonlinear response of four different circuits: an isolated decreasing nonlinear resistor $R_{a_3>0}$ characterized by $I = a_1 V_{\mathrm{NL}} + a_3 V_{\mathrm{NL}}^3$, an isolated increasing nonlinear resistor $R_{R_3>0}$ characterized by $V_{\mathrm{NL}} = R_1 I + R_3 I^3$ and each of them in series with a linear resistor, for the arbitrary choice $R_1 = 1/a_1 = 1/a_{\mathrm{L}} = 1\,\Omega$ and $R_3 = 1/a_3 = 1\,\Omega/\mathrm{V}^2$.

It is $x_{\mathrm{RoC}} = 2/(3\sqrt{3})$ for a=1 (see Equation A.0.13).

The function in Equation 2.3.21 is equivalent to the model discussed in [HCC09b] and [HCC10], termed "linear-nonlinear interaction": a nonlinear resistor is connected in series with a linear resistor. The nonlinear resistor is characterized by $I = a_1 V_{\mathrm{NL}} + a_3 V_{\mathrm{NL}}^3$ and the linear resistor by $I = a_{\mathrm{L}} V_{\mathrm{L}}$, V being the voltage and I the current. The resistor of the nonlinear resistor decreases with increasing voltage. The resulting response function of this system produces a saturation in the intermodulation level. The authors of [HCC09b] argue that this is the result of a decreasing voltage share of the overall voltage at the nonlinear resistor when the overall voltage is increased. This voltage share is sketched in Figure 2.10.

However, the intermodulation level also decreases for an increasing nonlinear resistor, which is characterized by $V = R_1 I + R_3 I^3$. For an increasing overall voltage, the voltage share at the nonlinear resistor increases. Following the argument in [HCC09b], this should lead to an increasing nonlinear response, rather than a saturation. The increasing nonlinear resistor even results in a saturation of the intermodulation level by its own, without being connected in series with a linear resistor. Instead, all three response functions have one thing in common: The power series has a limited radius of convergence for all those functions. Just in the case of the isolated decreasing nonlinear resistor, the radius of convergence of the power series is infinite. This suggest that the cause of the saturating intermodulation level in the model of [HCC09b] is rather the mathematical behavior of the chosen function than a physical one [4].

Finally, it is worth noting that the intermodulation slope tends towards 1/3 dB/dB, which is consistent with the slope of the cubic root function $y(x) = \sqrt[3]{x}$. On the other hand, the intermodulation of the saturable absorber saturates completely to 0 dB/dB.

Saturating intermodulation of a positive nonlinearity

So far, the presented models that show a saturating intermodulation all exhibit negative third order nonlinear responses. The upcoming model is an example for a positive nonlinearity, which still shows a saturation in the intermodulation. Thereby it shows that saturating intermodulation is not connected to the "saturation" (i.e. negative curvature) of the nonlinear response function itself. The model is based on a mechanical spring system [DH04] and is sketched in Figure 2.11. Its restoring force is given by:

$$F(x) = \frac{2F_v x}{\sqrt{l^2 + x^2}} + 2cx\left(1 - \frac{l}{\sqrt{l^2 + x^2}}\right) \tag{2.3.22}$$

Here, l is half the length between the holding plates, c is the spring constant and F_v is preload force. These parameters can be adjusted so that the restoring force either saturates with increasing displacement x ($F_v > cl$) or instead overdrives with increasing displacement x ($F_v < cl$), which can be easily seen in the power series expansion:

$$F(x) \approx \frac{2F_v}{l}x + \frac{cl - F_v}{l^3}x^3 \tag{2.3.23}$$

However, both nonlinear response functions result in a saturating intermodulation trend, even the one with the positive nonlinear third order term.

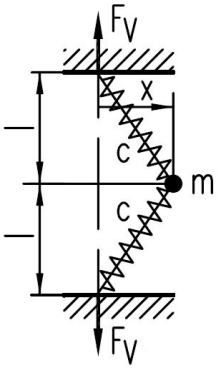

Figure 2.11: Sketch of mechanical geometric nonlinearity [DH04]

Separate amplitudes variation

In the examples above, the excitation signal was chosen to have two frequencies of equal amplitudes, $x(t) = A\,[\sin(\omega_1 t) + \sin(\omega_2 t)]$. Generally, the amplitudes are independent, $x(t) = A_1\,\sin(\omega_1 t) + A_2\,\sin(\omega_2 t)$. The Intermodulation Fourier Coefficient Method allows the calculation of the intermodulation level for independent amplitudes. The result for the saturable absorber of Equation 2.3.17 ($x_{\mathrm{RoC}} = 1$) is plotted in Figure 2.12. Three domains can be distinguished:

$$B_{\mathrm{IM3+}} \sim \begin{cases} A_1 A_2^2 \sim A^3 & \text{for } A_1 \ll x_{\mathrm{RoC}} \text{ and } A_2 \ll x_{\mathrm{RoC}} \\ A_1 A_2^{-1} \sim A^0 & \text{for } A_2 \gg x_{\mathrm{RoC}} \text{ and } A_2 \gg A_1 \\ A_1^{-2} A_2^2 \sim A^0 & \text{for } A_1 \gg x_{\mathrm{RoC}} \text{ and } A_1 \gg A_2 \end{cases} \tag{2.3.24}$$

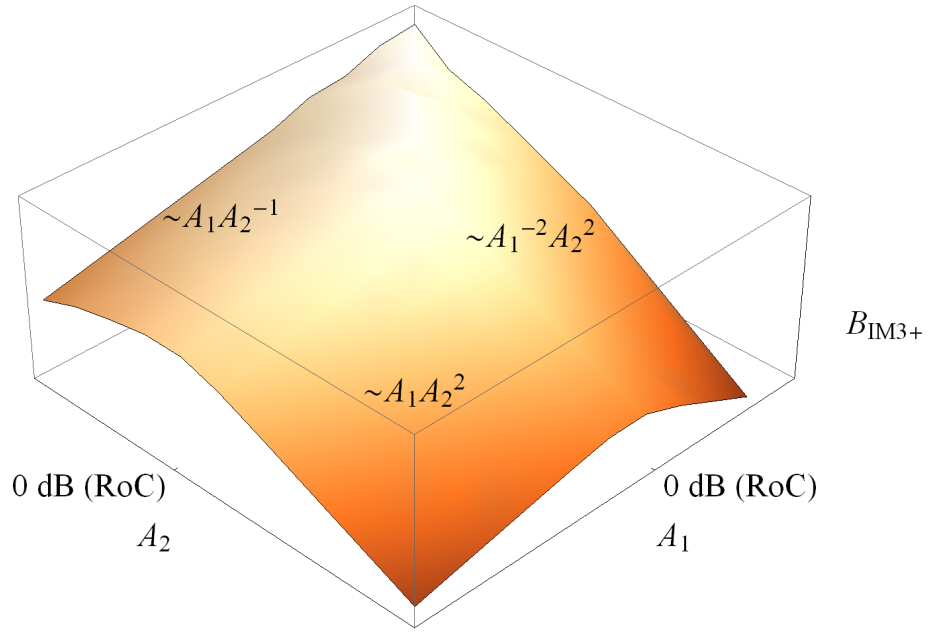

Figure 2.12: Upper third intermodulation level $B_{\mathrm{IM3+}}$ as a function of two input amplitudes A_1 and A_2 in a triple logarithmic plot. The area facing towards the contemplator is the regime in which the power series expansion model is applicable.

The inverse polynomial defined by Equation 2.3.20 with $x_{\mathrm{RoC}} = -4.1\,\mathrm{dB}$ (see Equation A.0.13) even results in broken exponent scaling:

$$B_{\mathrm{IM3+}} \sim \begin{cases} A_1 A_2^2 \sim A^3 & \text{for } A_1 \ll x_{\mathrm{RoC}} \text{ and } A_2 \ll x_{\mathrm{RoC}} \\ A_1 A_2^{-2/3} \sim A^{1/3} & \text{for } A_2 \gg x_{\mathrm{RoC}} \text{ and } A_2 \gg A_1 \\ A_1^{-5/3} A_2^2 \sim A^{1/3} & \text{for } A_1 \gg x_{\mathrm{RoC}} \text{ and } A_1 \gg A_2 \end{cases} \tag{2.3.25}$$

2.3.6 Conclusions for Dielectric Nonlinearities

So far, the intermodulation response of nonlinear systems has been discussed in an abstract manner. However, there are concrete physical nonlinear response functions, which have a limited convergence of their power series and a saturating intermodulation response. Figure 2.13 shows intermodulation responses for three nonlinear response functions: Langevin-like polarization P_{Lgv}, the polarization of a saturable absorber P_{sat} and the polarization of a binary state system P_{bin}. They will be associated with physical models in section 2.4. All presented nonlinear response functions show a similar saturating intermodulation trend, 3 dB/dB at low amplitudes, 0 dB/dB at high amplitudes. Nevertheless, the intermodulation trends are distinct from each other.
Measuring a classical 3 dB/dB slope of an intermodulation allows extracting the nonlinear susceptibility χ_3 (details in subsection 3.5.3). However, measuring χ_3 offers a limited interpretation only: with the sole knowledge of χ_3, it is impossible to decide if the nonlinearity stems from a highly nonlinear mechanism, which is barely present in the material, or if it is actually due to a less nonlinear but more abundant mechanism.

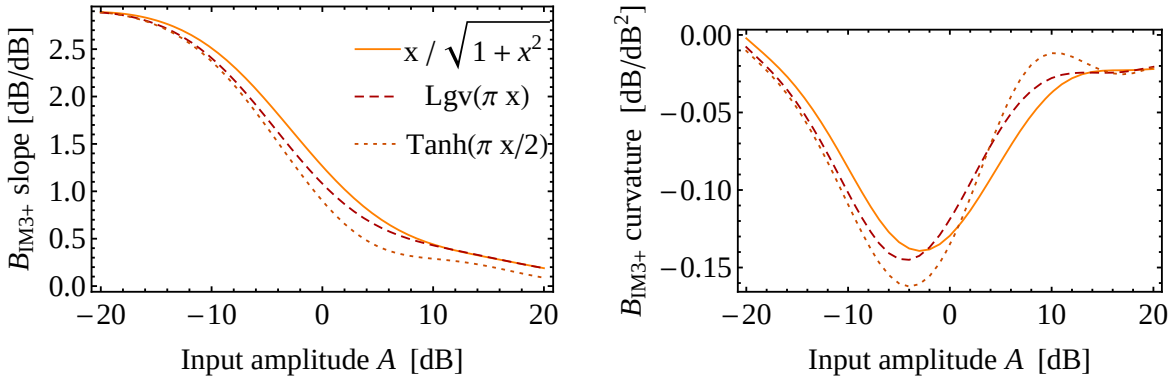

(a) Intermodulation slope

(b) Intermodulation curvature

Figure 2.13: Comparison of the intermodulation response of different mechanisms: The saturable absorber, the Langevin function Lgv(x) and tanh(x). They are scaled by the radius of convergence of their corresponding power series: it is $x = 1 = 0\,\mathrm{dB}$ for all three models. The mechanisms show a distinct intermodulation trend, which becomes most obvious in the curvature of the intermodulation signal. However, as discussed in subsection 2.3.5, the derivative and curvature data beyond 10 dB is not reliable anymore.

In more mathematical terms, e.g. for a Langevin response, (Equation 2.4.27) it is only possible to determine the product Np^4, not the separate density N of dipoles p.

The observation of a saturating intermodulation level allows determining an additional parameter. This parameter can be chosen somewhat deliberately, however, the "bending electric field amplitude of the intermodulation level" E_b seems to be the best-suited choice. E_b offers a second parameter to determine both N and p and therefore helps to identify the nonlinear mechanisms. E_b is a suitable parameter, as all arguments of the nonlinear response models can be written in terms of the applied field amplitude E normalized to the bending field strength E_b:

$$\begin{aligned} P_{\mathrm{Lgv}}(E) &\sim \mathrm{Lgv}\left(\pi \frac{E}{E_b}\right) \\ P_{\mathrm{bin}}(E) &\sim \tanh\left(\frac{\pi}{2}\frac{E}{E_b}\right) \\ P_{\mathrm{sat}}(E) &\sim \frac{E/E_b}{\sqrt{1+(E/E_b)^2}} \end{aligned} \tag{2.3.26}$$

The factors in the functions are chosen such that E_b furthermore represents the radius of convergence of the power series of each function, π for the Langevin function, $\pi/2$ for tanh(x) [Zuc72] and 1 for the saturable absorber [Boy08]. Then, E_b can be extracted by comparing the arguments to Equation 2.4.27, Equation 2.4.66 and Equation 2.4.44, respectively. The relation for the saturable absorber is already simplified under the assumptions of no detuning ($\Delta = 0$) and similar life times $t_1 = t_2 = t$:

$$\begin{aligned} E_b^{\mathrm{Lgv}} &= \frac{\pi}{L}\frac{k_\mathrm{B}T}{p_{per}} \\ E_b^{\mathrm{bin}} &= \frac{\pi}{2L}\frac{k_\mathrm{B}T}{qd/2} \\ E_b^{\mathrm{sat}} &= \frac{\hbar}{2L}\frac{\sqrt{1+\Delta^2 t_2^2}}{p_{21}\sqrt{t_1 t_2}} \approx \frac{\hbar}{2L}\frac{1}{p_{21}t} \end{aligned} \tag{2.3.27}$$

This shows that E_b is independent of the density N of the mechanism. Hence, E_b turns out to be a characteristic footprint for a mechanism.
Together with χ_3, which actually depends on the density N of the mechanism in the material, the linear contribution χ_1 of the respective mechanism can be determined:

$$\begin{aligned} \chi_1^{\mathrm{Lgv}} &= -\frac{15}{\pi^2}\chi_3 E_b^2 \\ \chi_1^{\mathrm{bin}} &= -\frac{12}{\pi^2}\chi_3 E_b^2 \\ \chi_1^{\mathrm{sat}} &= -2\chi_3 E_b^2 \end{aligned} \tag{2.3.28}$$

2.4 Microscopic Description of Dielectrics

This section deals with microscopic concepts and models of dielectric polarization. The connection of microscopic polarizability to the macroscopic dielectric response is discussed. In this framework, various local electric field models are introduced, which are crucial for addressing nonlinear polarization. The linear and nonlinear response of classical main polarization mechanisms is evaluated. Various additional nonlinear polarization models are introduced. Despite of being macroscopic effects, electrostriction and Maxwell stress are discussed together with these microscopic mechanisms for comparability. The section concludes with a literature review on the microscopic descriptions of linear microwave and nonlinear low frequency dielectric responses.

2.4.1 Polarizability and Local Electric Field

The electric field locally displaces charges by inducing (or orientating) dipoles. The polarization is the density of those dipoles [Bö73]:

$$\varepsilon_0 \chi \mathbf{E}_{mac} = \mathbf{P} = \frac{\Delta \mathbf{p}}{\Delta V} \tag{2.4.1}$$

The polarizability γ connects the charge displacement in a certain local electric field:

$$\mathbf{p} = \gamma \mathbf{E}_{loc} \tag{2.4.2}$$

The actual local electric field $\mathbf{E}_{loc}$ that a charge experiences in a dielectric differs from the macroscopic applied electric field $\mathbf{E}_{mac}$. Comparable to the susceptibility χ (see

Equation 2.4.3), the polarizability γ generally is a tensor and is written as a power series for nonlinear polarizabilities:

$$p_i = \sum_j \gamma_{ij} E_j^{loc} + \sum_{jk} \gamma_{ijk} E_j^{loc} E_k^{loc} + \sum_{jkl} \gamma_{ijkl} E_j^{loc} E_k^{loc} E_l^{loc} + ... \tag{2.4.3}$$

In contrast to the susceptibility χ, the macroscopic symmetry of Equation 2.2.16 does not apply to the microscopic polarizabilities γ_i. However, for simplicity, the polarizability and the susceptibility are written in equivalent manners:

$$\begin{aligned} p &= \gamma_1 E_{loc} + \gamma_3 E_{loc}^3 \\ P/\varepsilon_0 &= \chi_1 E_{mac} + \chi_3 E_{mac}^3 \end{aligned} \tag{2.4.4}$$

By relating p and P via the density N, $P = Np$, comparison of coefficients leads to:

$$\begin{aligned} \chi_1 &= \frac{N}{\varepsilon_0} L \ \gamma_1 \\ \chi_3 &= \frac{N}{\varepsilon_0} L^3 \ \gamma_3 \end{aligned} \tag{2.4.5}$$

Here, L is the local electric field correction factor, given by:

$$\mathbf{E}_{loc} = L \ \mathbf{E}_{mac} \tag{2.4.6}$$

The most common way to account for the electric field of all other charges in the dielectric is an imaginary sphere around a point in the dielectric, a concept introduced by Lorentz [Kit73]. This sphere is sufficiently large so that the dielectric can be assumed to be homogeneously polarized outside of the sphere. The field from the surface charge density gives rise to the Lorentz field in the center of this sphere:

$$\mathbf{E}_{Lor} = \frac{1}{3} \frac{\mathbf{P}}{\varepsilon_0} \tag{2.4.7}$$

If the atoms have a surrounding with cubic lattice, it can be shown that the resulting field from the dipoles within that sphere vanishes. The Lorentz field leads to the local electric field:

$$\mathbf{E}_{loc} = \left(\frac{\varepsilon_r + 2}{3} \right) \mathbf{E}_{mac} \tag{2.4.8}$$

To arrive at this classic field correction factor, two assumptions were made: First, cubic symmetry was presumed. For other symmetries, the field within the sphere is different from zero [Kit73]. In the perovskite structure, the local field correction can even significantly deviate from the simple Lorentz model [Sla50]. However, the authors of [AOK19] claim that the Lorentz relation can be derived by just assuming a homogeneous and isotropic dielectric.

The Clausius-Masotti equation relies on the local field factor by Lorentz. It connects the polarizability γ with the relative permittivity ε_r:

$$\varepsilon_r = 1 + \frac{3N\gamma}{3\varepsilon_0 - N\gamma} \tag{2.4.9}$$

Here N is the density of the polarizabilities γ. From the denominator, it is clear that this model fails for $N\gamma \geq 3\varepsilon_0$. [AOK19] collects other field correction factors, which can be obtained as special cases of the Onsager-Böttcher (OB) model:

$$L_{\mathrm{OB}} = \frac{L_{\mathrm{L}}}{1 - 2\frac{(\varepsilon_r - 1)^2}{9\varepsilon_r}\frac{\delta}{\alpha}} \tag{2.4.10}$$

Here, $\delta = \gamma - \alpha$, and γ is the polarizability of the dipole of interest and α is the polarizability of the removed sphere around that dipole. For $\gamma \ll \alpha$ this leads to the empty cavity (EC) model:

$$L_{\mathrm{EC}} = \frac{3\varepsilon_r}{2\varepsilon_r + 1} \tag{2.4.11}$$

Another special case ($\gamma = \alpha$) is the classical Lorentz field correction (L):

$$L_{\mathrm{L}} = \frac{\varepsilon_r + 2}{3} \tag{2.4.12}$$

Of course, the validity of the Onsager-Böttcher model is also limited, as can be seen from the denominator. It is only applicable as long as the following relation holds:

$$\frac{\alpha}{\delta} < \frac{9\varepsilon_r}{2(\varepsilon_r - 1)^2} \tag{2.4.13}$$

In conclusion, the calculation of the local electric field that is experienced by the actual charges is anything but trivial, especially for nonhomogeneous dielectrics. The effect of the local electric field is just a minor correction in optics where $\varepsilon_r \approx 2$. However, in the microwave range, the local electric field correction factor can lead to differences of several orders of magnitude in the nonlinear susceptibility. The nonlinear mechanism crucially depends on the local electric field and can lead to different results [BCA06]. This needs to be taken into account when discussing nonlinear mechanisms.

2.4.2 Overview of Polarization Mechanisms

Figure 2.14 sketches a standard representation of the frequency dependency of the relative permittivity. Every mechanism has its characteristic frequency response. There are three basic polarization mechanisms [Bö73]:

- Dipolar polarization represents the orientation of permanent electric dipoles. It is therefore only present in materials containing permanent dipoles. Dipolar polarization contributes up to the microwave range.

- Ionic polarization summarizes the displacement of ions from their equilibrium position. Though most condensed matter dielectrics rely on some kind of bond

with ionic character, there are materials (e.g. diamond) with covalent bonds. Those materials lack ionic polarization. Ionic polarization contributes up the infrared range.

- Electronic polarization summarizes electronic contributions, such as the displacement of the electrons against their appended atomic nucleus or band transitions in a solid. Electronic polarization contributes up to the ultraviolet range and is present in all dielectrics.

All these polarization mechanisms exhibit a nonlinear response that becomes relevant at high electric fields. An overview of nonlinear dielectric responses is given in [Bö73] with the focus on static fields. [Boy08] on the other hand collects nonlinear mechanisms at optical frequencies. The following list sums up all the effects. The list does not include secondary effects such as change of the permittivity due to heating and thermal expansion.

- Permanent dipole alignment: The orientation of dipoles contributes to the polarizability as long as they are not completely aligned. This saturation leads to a negative nonlinear susceptibility χ_3.
- Hyperpolarizabilities: Higher order polarizabilities of the constituents directly translate into higher order susceptibilities, including χ_3. This effect can return both negative and positive susceptibilities.
- Equilibrium shifting: If the constituents of a material have an anisotropic polarizability or there is an equilibrium between constituents of different polarizability, they are directed with their axis of high polarizability in the direction of the electric field or the equilibrium is shifted towards more polar constituents. In this case, higher electric fields lead to higher polarizability of the material, so the susceptibility χ_3 is positive.
- Electrostriction: The applied electric field increases the density of the material, leading to a larger permittivity, corresponding to a positive χ_3.
- Saturable atomic absorption: A photon is resonantly absorbed by an electron, which thereby transits into a different electronic state. As this is a resonant effect, it does not appear at static fields, and depending on the detuning, the resulting χ_3 can be either positive or negative.

In the following, the mechanisms from the list are compared in their theoretical linear and nonlinear response. First, the hyperpolarizabilities are discussed in the framework of an anharmonic oscillator as a first approach.
In nonlinear processes, many frequencies can be involved. These frequencies can lie in very different frequency ranges. For simplicity, however, the following discussion, assumes that the applied frequencies and the resulting mixing frequencies of interest

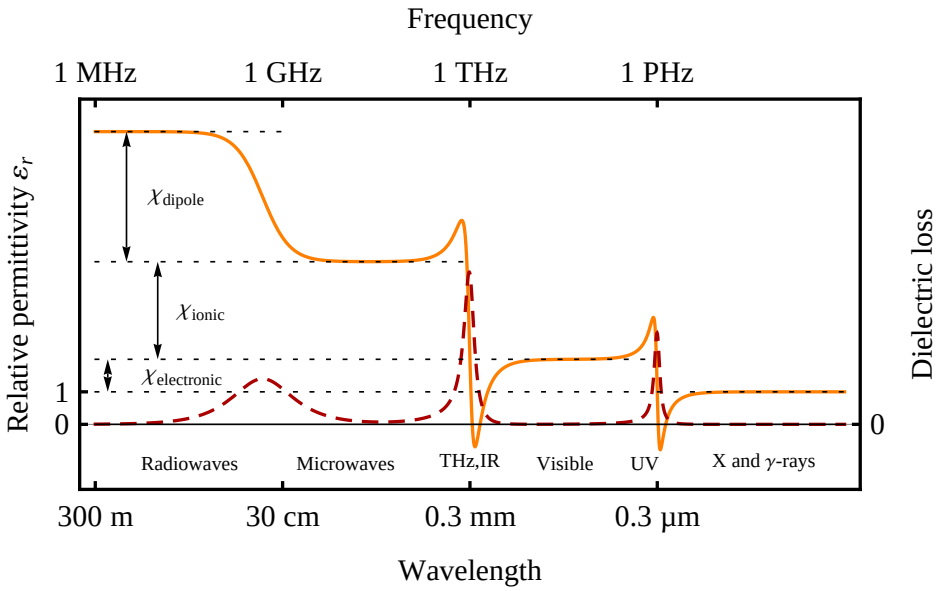

Figure 2.14: Sketch of the real and imaginary parts of the dielectric function illustrating the main polarization mechanisms. The dipolar polarization is a relaxation process, which lacks a restoring force to exhibit resonant behavior.

all lie in a small region around a single frequency ω. The region is so small that the material properties can be expected to be constant. A discussion of more general frequency mixing can be found in e.g. [Boy08].

2.4.3 The Anharmonic Oscillator

In the surrounding of a potential minimum the potential's derivative vanishes and the first nonzero term is a linear restoring force $F = kx$ with x being the displacement from the potential minimum. The corresponding potential reads:

$$U(x) = \frac{1}{2}kx^2 \tag{2.4.14}$$

For a particle in such a potential with mass m and charge q in an electric field $E(t)$ the equation of motion is that of the driven harmonic oscillator:

$$\ddot{x} + 2\alpha\dot{x} + \omega_0^2 x = \frac{q}{m}E(t) \tag{2.4.15}$$

Here, the resonance frequency is given by $\omega_0^2 = \frac{k}{m}$ and the phenomenological damping α was introduced. For larger amplitudes, the harmonic oscillator can be extended with a symmetric nonlinearity to a classical anharmonic oscillator [Boy08]. Its potential is given by:

$$U(x) = \frac{1}{2}m\omega_0^2 x^2 - \frac{1}{4}mbx^4 \tag{2.4.16}$$

Here, b is a weighting parameter for the nonlinear term. The minus is introduced to

obtain a positive nonlinear susceptibility χ_3 for a positive b. The equation of motion is thus modified accordingly:

$$\ddot{x} + 2\alpha\dot{x} + \omega_0^2 x - bx^3 = \frac{q}{m}E(t) \tag{2.4.17}$$

The equation of motion is solved in a perturbative manner by replacing $E(t)$ with $\lambda E(t)$. The solution for $x(t)$ shall have the form of power series in λ^n:

$$x(t) = \lambda x_1(t) + \lambda^2 x_2(t) + \lambda^3 x_3(t) + ... \tag{2.4.18}$$

The equations of motion can be separated for each exponent n of λ:

$$\begin{aligned} \ddot{x}_1 + 2\alpha\dot{x}_1 + \omega_0^2 x_1 &= \frac{q}{m}E(t) \\ \ddot{x}_2 + 2\alpha\dot{x}_2 + \omega_0^2 x_2 &= 0 \\ \ddot{x}_3 + 2\alpha\dot{x}_3 + \omega_0^2 x_3 &= b\ x_1^3 \end{aligned} \tag{2.4.19}$$

The solution of the first equation is the damped harmonic oscillator. Setting $E(t) = E\exp(-i\omega t)$, the solution is $x_1(t) = \hat{x}_1\exp(-i\omega t)$, with the amplitude

$$\hat{x}_1 = \frac{q}{m}\frac{E}{D(\omega)}. \tag{2.4.20}$$

Here, $D(\omega) = \omega_0^2 - \omega^2 - i\ 2\alpha\omega$. The steady state solution of the second equation is zero, $x_2(t) = 0$. The solution $x_1(t)$ of the first equation can be inserted into the third equation. Here, the solution appears to the power of three, $x_1(t)^3$. In general, these three solutions are independent, having distinct amplitudes x_l, x_m, x_n and frequencies ω_l, ω_m, ω_n:

$$\ddot{x}_3 + 2\alpha\dot{x}_3 + \omega_0^2 x_3 = b\ \frac{q^3}{m^3}\frac{E_l}{D(\omega_l)}\frac{E_m}{D(\omega_m)}\frac{E_n}{D(\omega_n)}e^{-i(\omega_l+\omega_m+\omega_n)t} \tag{2.4.21}$$

Denoting $\omega_j = \omega_l + \omega_m + \omega_n$, the ansatz $x_3(t) = \hat{x}_3\exp(-i\omega_j t)$ yields:

$$\hat{x}_3 = \frac{b}{D(\omega_j)}\frac{q^3}{m^3}\frac{E_l}{D(\omega_l)}\frac{E_m}{D(\omega_m)}\frac{E_n}{D(\omega_n)} \tag{2.4.22}$$

For equal amplitudes and similar frequencies, this becomes:

$$\hat{x}_3 = b\frac{q^3}{m^3}\frac{E^3}{D(\omega)^4} \tag{2.4.23}$$

The linear and nonlinear polarizability are obtained by translating the displacement x into the induced dipole $p = qx$, $\gamma_1 = q\hat{x}_1/E_{loc}$ and $\gamma_3 = q\hat{x}_3/E_{loc}^3$, respectively:

$$\begin{aligned} \gamma_1 &= \frac{q^2}{mD(\omega)} \\ \gamma_3 &= \frac{b\ q^4}{m^3 D(\omega)^4} \end{aligned} \tag{2.4.24}$$

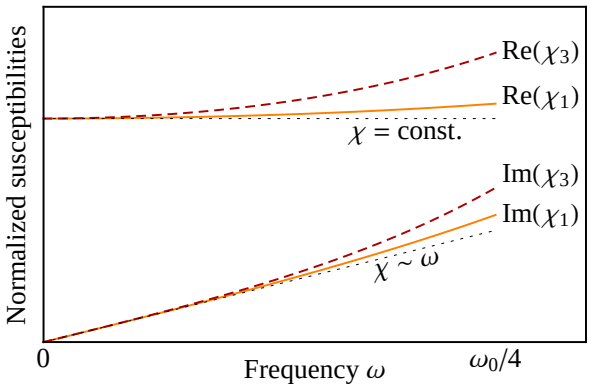

Figure 2.15: Response of an anharmonic oscillator for frequencies far below the resonance frequency. $\mathrm{Re}(\chi_3)$ and $\mathrm{Re}(\chi_1)$ are normalized to their magnitude at $\omega = 0$.

The linear and nonlinear susceptibility are obtained by correcting for the local electric field using Equation 2.4.5

$$\begin{aligned} \chi_1 &= \frac{N\ q^2}{\varepsilon_0\ m\ D(\omega)} L \\ \chi_3 &= \frac{b\ N\ q^4}{\varepsilon_0\ m^3\ D(\omega)^4} L^3 \end{aligned} \tag{2.4.25}$$

Depending on the sign of b, χ_3 may take different signs as well. However, it is important to note the limitations of that model. Even though $D(\omega)$ suggest a broad frequency range applicability of the model, this perturbative approach holds for small amplitudes $\chi_3 E^2 \ll \chi_1$ only. This is only the case far below the resonance frequency ω_0.
Figure 2.15 sketches the frequency trend of the linear imaginary and real susceptibilities. For frequencies far below the resonance frequency, the real parts of the susceptibilities are constant while the imaginary part increases linearly. For the nonresonant mechanism discussed above, the nonlinear susceptibility $\mathrm{Re}(\chi_3)$ can be assumed to be weakly frequency dependent comparable to the linear susceptibility $\mathrm{Re}(\chi_1)$. The nonlinear imaginary susceptibility $\mathrm{Im}(\chi_3)$ scales linearly with the frequency comparable to the linear imaginary susceptibility $\mathrm{Im}(\chi_1)$.

2.4.4 Saturating Dipole Orientation

The frequency response of permanent dipoles in an alternating electric field is described by Debye relaxation [Kit73]:

$$\chi(\omega) = \frac{\chi_{stat}}{1 - i\omega\tau} \tag{2.4.26}$$

Here, χ_{stat} is the static susceptibility, given by the Langevin function [Kit73]. The Langevin function arises from the Boltzmann distribution in the potential $W = \mathbf{p}_{per} \cdot \mathbf{E}_{loc} = p_{per} E \cos\theta$ of the permanent dipole $\mathbf{p}_{per}$ in the electric field $\mathbf{E}_{loc}$:

$$\mathbf{p}_{ind} = \mathbf{p}_{per}\mathrm{Lgv}(x) \tag{2.4.27}$$

Here, $x = p_{per}E_{loc}/(k_\mathrm{B}T)$, k_B being the Boltzmann constant and T the temperature. The Langevin function and its power series' first terms read

$$\mathrm{Lgv}(x) = \coth(x) - \frac{1}{x} \approx \frac{x}{3} - \frac{x^3}{45} \tag{2.4.28}$$

Hence, the third order power series of the induced dipole p_{ind} returns:

$$p_{ind} = \frac{p_{per}^2}{3\ k_\mathrm{B}T}E_{loc} - \frac{p_{per}^4}{45\ (k_\mathrm{B}T)^3}E_{loc}^3 \tag{2.4.29}$$

Thus, the polarizabilities of the dipole relaxing system are:

$$\begin{aligned}\gamma_1^{relax} &= \frac{1}{3}\frac{p_{per}^2}{k_\mathrm{B}T} \\ \gamma_3^{relax} &= -\frac{p_{per}^4}{45\ (k_\mathrm{B}T)^3}\end{aligned} \tag{2.4.30}$$

And finally translating to the macroscopic susceptibility using Equation 2.4.5:

$$\begin{aligned}\chi_1 &= \frac{Np^2}{3\varepsilon_0 k_\mathrm{B}T}L \\ \chi_3 &= -\frac{Np^4}{45\varepsilon_0(k_\mathrm{B}T)^3}L^3\end{aligned} \tag{2.4.31}$$

The static susceptibility χ_{stat} in Equation 2.4.26 is the sum of the linear and all nonlinear susceptibilities. In contrast to the anharmonic oscillator discussed further above, the sign of the relaxation nonlinearity is certainly negative.

Estimation of the nonlinear susceptibilities

The magnitude of the effects discussed above shall be calculated for typical dielectrics. The magnitude of the nonlinear parameter b in Equation 2.4.25 is estimated by assuming the nonlinear restoring force mbx^3 to have an comparable magnitude to the linear restoring force $m\omega_0^2 x$ when the displacement x is in the order of d. In optics, d is the size of an atom [Boy08]. This distance is also chosen for estimation in the microwave range. b then turns out to be:

$$b = \pm\frac{\omega_0^2}{d^2} \tag{2.4.32}$$

So far, no choice for the sign of b has been made. The sign is discussed in more concrete models later in this section. The resonant model is only applicable far below the resonances. Setting $\omega = 0$ in Equation 2.4.25 and hence $D(\omega) = \omega_0^2$ leads to the estimates in Table 2.2.

The estimate for optics is rather good for both the linear and nonlinear susceptibility [Boy08]. However, the model is highly sensitive to the assumptions ($\sim \omega_0^6, q^4, m^3, d^2$).

Table 2.2: Estimates for the linear and nonlinear susceptibility in optics, the microwave range and the radio wave range. $m_p = 1.67 \times 10^{-27}\,\mathrm{kg}$ and $m_e = 9.1 \times 10^{-31}\,\mathrm{kg}$. The $L = 1$ line neglects local field corrections to calculate both the linear and the nonlinear susceptibility, while the $L = Lor$ line takes experimental dielectric permittivity to calculate the nonlinear susceptibility with the Lorentz field model.

	dipolar	ionic	electronic
model parameters	$N = 4 \times 10^{28}\,\mathrm{m}^{-3}$ $p = 6.15 \times 10^{-30}\,\mathrm{C\,m}$ $T = 300\,\mathrm{K}$	$N = 4 \times 10^{28}\,\mathrm{m}^{-3}$ $\omega_0 = 7 \times 10^{12}\,\mathrm{s}^{-1}$ $m = 50\ m_p$ $d = 3 \times 10^{-10}\,\mathrm{m}$	$N = 4 \times 10^{28}\,\mathrm{m}^{-3}$ $\omega_0 = 7 \times 10^{15}\,\mathrm{s}^{-1}$ $m = m_e$ $d = 3 \times 10^{-10}\,\mathrm{m}$
$\chi_{1,L=1}$	20	28	2.6
$\chi_{3,L=1}$	$-2 \times 10^{-18}\,\mathrm{m}^2/\mathrm{V}^2$	$\pm 5 \times 10^{-19}\,\mathrm{m}^2/\mathrm{V}^2$	$+4 \times 10^{-22}\,\mathrm{m}^2/\mathrm{V}^2$
$\chi_{1,exp}$	80	20	2
$\chi_{3,L=Lor}$	$-4 \times 10^{-14}\,\mathrm{m}^2/\mathrm{V}^2$	$\pm 2 \times 10^{-16}\,\mathrm{m}^2/\mathrm{V}^2$	$+2 \times 10^{-21}\,\mathrm{m}^2/\mathrm{V}^2$

Still, the oscillator model allows predicting the nonlinear optical response of a glass from its linear ones [ACP87]. To translate this estimation into the microwave range, d and N are chosen equal, and ω_0 is shifted to a typical magnitude of optical phonon resonances. m is chosen to be close to that of a medium sized atom, Titanium ($m = 47\ u$). The magnitude of the nonlinearity also depends strongly on the local field correction, $\chi_3 \sim L^3$. This results in estimates of several orders of magnitude larger than when simply assuming $L = 1$. Applying the Clausius-Masotti equation with its Lorentz correction factor $L = (\varepsilon_r + 2)/3$ leads to meaningless negative linear susceptibilities χ_1, beyond the validity of Clausius-Masotti. As the Clausius-Masotti model fails for high permittivity, the final line in Table 2.2 uses typical experimental permittivity as a basis to estimate L and hence the magnitude of the nonlinearity (80 for water [MM56]). However, the $L = 1$ model should be reasonable for a gas. For a typical value of $10\,\mathrm{g/m}^3$ of water vapor ($p = 6.15 \times 10^{-30}$ C m) in air at ambient temperature this yields $\chi_1 = 10^{-4}$ and $\chi_3 = 1.7 \times 10^{-23}\,\mathrm{m}^2/\mathrm{V}^2$.

Instead of just estimating the nonlinear parameter b by assuming the nonlinear term to be equal to the linear term at certain displacements, real data of other nonlinear phenomena are consulted. These models also give a prediction of the sign of the nonlinearity. For instance, thermal expansion is a phenomenon of nonlinear interactions. Hence, there is already data on the nonlinear potential of atoms in a solid.

Before the discussion of this model, the force constants k of the potential $U(x) = \frac{1}{2}k_1x^2 + \frac{1}{4}k_3x^4$ are related to the polarizabilities γ. The restoring force reads:

$$F(x) = k_1 x + k_3 x^3 \tag{2.4.33}$$

The restoring force $F(x)$ is balanced by the electrical force $F(x) = qE_{loc}$. Solving for x and considering the power series' first nonlinear term only returns:

$$p = \frac{q^2}{k_1} E_{loc} - \frac{q^4\ k_3}{k_1^4} E_{loc}^3 \tag{2.4.34}$$

Comparing this to Equation 2.4.4 yields:

$$\begin{aligned} \gamma_1 &= \frac{q^2}{k_1} \\ \gamma_3 &= -\frac{q^4\ k_3}{k_1^4} \end{aligned} \tag{2.4.35}$$

Returning to a model for thermal expansion, a very simplistic estimation is performed by taking a repellent potential of the form $\lambda \exp(-r/\rho)$ and an attractive Coulomb potential $\sim 1/r$. The parameters of the potential are deduced from the equilibrium distance and the bulk modulus [Kit73]:

$$\Phi(r) = 2.4 \times 10^4\,\mathrm{eV}\,\exp(-r/0.3\,\mathrm{\AA}) - 25.2\,\mathrm{\AA}/r \tag{2.4.36}$$

The power series of this potential at r_0 up to the fourth term is:

$$\Phi(r - r_0) = 3.53\,\mathrm{eV/\AA^2}(r - r_0)^2 - 4.59\,\mathrm{eV/\AA^3}(r - r_0)^3 + 3.97\,\mathrm{eV/\AA^4}(r - r_0)^4 \tag{2.4.37}$$

Neglecting the local field correction factor and using the relations in Equation 2.4.5 yields

$$\begin{aligned} \chi_1 &= \frac{N}{\varepsilon_0}\frac{q^2}{k_1} = 2 \\ \chi_3 &= -\frac{N}{\varepsilon_0}\frac{q^4 k_3}{k_1^4} = -2 \times 10^{-21}\,\mathrm{m^2/V^2} \end{aligned} \tag{2.4.38}$$

A more elaborate model deduces the interatomic potential for lead from measured phonon widths [MF62]. Lead is a metal and hence the bonding is of metal character. In general, it is wrong to conclude properties for ionic bonds. Nevertheless, it gives a comparative point. From the data given in [MF62], the potential reads (see Equation A.0.1 for explicit calculation):

$$\Phi(r - r_0) = 0.56\,\mathrm{eV/\AA^2}(r - r_0)^2 - 1.01\,\mathrm{eV/\AA^3}(r - r_0)^3 + 1.04\,\mathrm{eV/\AA^4}(r - r_0)^4 \tag{2.4.39}$$

Neglecting the local field correction factor and using the relations from Equation 2.4.5

$$\begin{aligned} \chi_1 &= \frac{N}{\varepsilon_0}\frac{q^2}{k_1} = 13 \\ \chi_3 &= -\frac{N}{\varepsilon_0}\frac{q^4 k_3}{k_1^4} = -7 \times 10^{-19}\,\mathrm{m^2/V^2} \end{aligned} \tag{2.4.40}$$

These two estimations of the nonlinear characteristics of a nonlinear polarization are

very simplistic. Especially the former example needs to be treated carefully, as it is originally only used to estimate thermal expansion, which is a result of the $\Phi \sim r^3$ term, not of the $\Phi \sim r^4$ term, which is relevant for χ_3. However, they lead to results of similar order of magnitude and are even comparable to the anharmonic oscillator, summarized in Table 2.2. In contrast to optics, it is worth noting that the nonlinear restoring constants k_3 are positive in both models, resulting in a negative χ_3. While in optics, the hand-waving argument for positive nonlinearities was a decreasing restoring force when the electron is moved from the nucleus, an opposing argument can be offered for ionic responses: The further the ion is displaced, the stronger the repulsion from its neighboring ion becomes.
The neglect of the local field correction factor underestimates the nonlinear susceptibility by a factor of L^3. Assuming a Lorentz field correction factor from Equation 2.4.7, this corresponds to a factor of 10^3 in the nonlinear susceptibility for $\varepsilon_r = 28$.
To complete the different ranges for the nonlinearities, it shall be mentioned that even the vacuum permittivity ε_0 becomes nonlinear at some point due to photon-photon scattering [EK35]. However, the effect is tremendously small: $\chi_3 = 3.4 \times 10^{-41}\,\mathrm{m^2/V^2}$ [Boy08].

2.4.5 Saturating Resonant Absorbtion

While the discussion of the anharmonic oscillator in subsection 2.4.3 is suitable for far off-resonance description, the resonant response of a two level system [Boy08] is better described by:

$$\chi = \frac{N}{\varepsilon_0}(\rho_2 - \rho_1)p_{21}^2 \frac{t_2}{\hbar} \frac{\Delta\ t_2 - i}{1 + \Delta^2 t_2^2 + E^2/E_s^2} \tag{2.4.41}$$

E_s is the saturation field amplitude and reads:

$$E_s^2 = \frac{\hbar^2}{4p_{21}^2 t_1 t_2} \tag{2.4.42}$$

The detuning factor is given by $\Delta = \omega - \omega_{21}$ with ω_{21} being the resonant transition frequency. t_1 is the lifetime of the upper level, t_2 the characteristic dephasing time. $(\rho_2 - \rho_1)$ is the difference of the occupation of the two states in equilibrium, p_{21} is the transition dipole moment. Defining $E_b^2 = E_s^2(1 + \Delta^2 t_2^2)$ returns:

$$\chi = \frac{N}{\varepsilon_0}(\rho_2 - \rho_1)p_{21}^2 \frac{t_2}{\hbar} \frac{\Delta\ t_2 - i}{1 + \Delta^2 t_2^2} \frac{1}{1 + E^2/E_b^2} \tag{2.4.43}$$

So both the imaginary and the real part of the susceptibility are proportional to $1/(1 + E^2/E_b^2)$. However, [HHH+03] and [HvS81] arrive at a proportionality to $1/\sqrt{1 + E^2/E_b^2}$. The small amplitude linear response of both systems is the same; however, they certainly qualitatively deviate from each other at high field amplitudes: While the polarization of $1/\sqrt{1 + E^2/E_b^2}$ tends towards a constant value for high field amplitudes, the polarization of the $1/(1 + E^2/E_b^2)$ susceptibility goes to zero. This seems physically implausible.

Hence, this work continues with the formulation including the square root, though the contradiction remains unsolved. The following notation will be used:

$$P/\varepsilon_0 = \frac{\chi_1 E}{\sqrt{1+(E/E_b)^2}} \tag{2.4.44}$$

The saturating resonant absorption can result in highly nonlinear responses. Following the estimate for optical nonlinearities in [Boy08] and setting $N = 10^{20}\,\mathrm{m}^{-3}$, $(\rho_2 - \rho_1) = -1$, $p_{21} = 2 \times 10^{-29}\,\mathrm{Cm}$, $t_1 = 16\,\mathrm{ns}$, $t_2 = 2t_1$ and $\Delta t_2 = 6000$ (corresponding to $\Delta = 2\pi c\ 1\,\mathrm{cm}^{-1}$) results in $\chi_3 = 10^{-16}\,\mathrm{m}^2/\mathrm{V}^2$. A resonant two level system has been considered to be the source of nonlinearity in high temperature superconductor microwave devices [HOH+02, HHH+03]. Depending on the detuning Δ, this mechanism generates both negative and positive nonlinear susceptibilities.

2.4.6 Electrostriction and Maxwell Stress

Electrostriction connects the dielectric properties of a material with its mechanical properties, namely its bulk modulus $K = -V\frac{\partial p}{\partial V}$ [Bö73]. In contrast to the piezoelectric effect, electrostriction is quadratic in the applied electric field and thus corresponds to a third order nonlinear susceptibility χ_3:

$$\chi_3^{\Delta\varepsilon} = \frac{(\varepsilon_r - 1)^2}{3}\frac{\varepsilon_0}{K} \tag{2.4.45}$$

The $\Delta\varepsilon$ emphasizes a real change in the permittivity. This distinction is important in a capacitor geometry, as electrostriction additionally induces a change in the thickness d of the dielectric [WLL+08]:

$$\frac{\Delta d}{d} = \epsilon = \frac{\sigma}{Y} = -\frac{\varepsilon_0}{Y}\frac{3\varepsilon_r^2 - \varepsilon_r - 2}{10}E_{ext}^2 \tag{2.4.46}$$

Here, ϵ is the strain, σ the stress and Y the Young's modulus of elasticity. By attributing the change in capacitance $\Delta C = C\Delta d/d$ to an equivalent dielectric nonlinearity $\chi_3^{\Delta d,eq.}$, it is possible to compare the order of magnitude of those effects:

$$\frac{\chi_3^{\Delta d,eq.} E_{mac}^2}{\varepsilon_r} = \frac{\Delta C}{C} = -\frac{\Delta d}{d} = \frac{\varepsilon_0}{Y}\frac{3\varepsilon_r^2 - \varepsilon_r - 2}{10}E_{ext}^2 \tag{2.4.47}$$

Solving for $\chi_3^{\Delta d,eq.}$ yields:

$$\chi_3^{\Delta d,eq.} = \frac{\varepsilon_0}{Y}\frac{3\varepsilon_r^2 - \varepsilon_r - 2}{10}\varepsilon_r^3 \tag{2.4.48}$$

In a capacitor geometry, the electric field additionally gives rise to an attraction between the electrodes. This attraction (Maxwell stress) leads to a compression of the dielectric. In contrast to the electrostrictive change in thickness, this effect only occurs with charged electrodes attached to the surface of the dielectric [WLL+08]:

$$\frac{\Delta d}{d} = \varepsilon = \frac{\sigma}{Y} = -\frac{\varepsilon_0}{Y}\frac{\varepsilon_r}{2}E_{ext}^2 \tag{2.4.49}$$

Comparable to Equation 2.4.47, this chance in capacitance is attributed to an equivalent nonlinear susceptibility $\chi_3^{Mxw.,eq.}$:

$$\chi_3^{Mxw.,eq.} = \frac{\varepsilon_0}{Y}\frac{\varepsilon_r^4}{2} \tag{2.4.50}$$

To estimate the magnitude, the values for Fused Silica ($K = 37\,\mathrm{GPa}$, $\varepsilon_r = 3.75$, Poisson number $\nu = 0.17$) are taken [Mun02]. With $Y = 3(1-2\nu)K = 73\,\mathrm{GPa}$, this yields:

$$\begin{aligned} \chi_3^{\Delta\varepsilon} &= 6 \times 10^{-22}\,\mathrm{m^2/V^2} \\ \chi_3^{Mxw.,eq.} &= 1 \times 10^{-20}\,\mathrm{m^2/V^2} \\ \chi_3^{\Delta d,eq.} &= 6 \times 10^{-21}\,\mathrm{m^2/V^2} \end{aligned} \tag{2.4.51}$$

These values are of the same order of magnitude as electronic hyperpolarizabilities and all exhibit a positive sign. Electrostriction has been expected to be the principal source of nonlinearity in good nonpolar dielectrics in the microwave range [Sta80]. All estimates strongly depend on the permittivity ε_r because of the de-electrification field that relates E_{mac} and E_{ext}.

2.4.7 Equilibrium Shift

Among the models discussed so far, only the permanent dipole orientation included nonzero temperature. For electronic resonance nonlinearities, it is reasonable to neglect thermal effects, as the thermal energy $k_\mathrm{B}T = 25\,\mathrm{meV}$ is much smaller than the energies of interest (some eV). In contrast to the optical range, the thermal energy at room temperature is way above the optical phonon energy, which contribute to the polarization in the microwave range.

In analogy to the Doulong-Petit law for heat capacity, a rough estimation of thermal time length scales is possible. According to the virial theorem, the thermal energy is equally distributed between potential and kinetic energy:

$$\frac{1}{2}k_B T = \frac{1}{2}mv^2 = \frac{1}{2}k\Delta x^2 \tag{2.4.52}$$

The spring constant k can be estimated by the frequency of the optical phonon resonance $\omega_0 = \sqrt{k/m}$ with the mass of the ions known. For $f_{opt.Ph.} = 10^{12}\,\mathrm{Hz}$ and $m = 47\,\mathrm{u}$, this yields $k = 3\,\mathrm{N/m}$. Then, inserting this k into Equation 2.4.52 gives:

$$\Delta x_{therm.} = \sqrt{\frac{k_B T}{k}} = \sqrt{\frac{k_B T}{m\,\omega^2}} = 40\,\mathrm{pm}. \tag{2.4.53}$$

This is 20 % of a typical interatomic distance of 200 pm.

A typical displacement by an electric field is estimated by comparing $P = \varepsilon_0\chi E$ and $P = Np = Nq\Delta x$. For an electric field of $1\,\mathrm{V/mm}$, a susceptibility $\chi = 10$, a density

$N = 10^{28}\,\mathrm{m}^{-3}$ and a single elementary charge q, this yields:

$$\Delta x_{dielec.} = \frac{\varepsilon_0 \chi E}{q\ N} = 10^{-4}\,\mathrm{pm} \tag{2.4.54}$$

This is five orders of magnitude smaller than the thermal displacement, $\Delta x_{therm.} \gg \Delta x_{dielec.}$. On the other hand, $t_{therm.} \ll t_{dielec.}$, as the frequency of interest $f_{elec.} = 1\,\mathrm{GHz}$ is far below $f_{opt.Ph.}$.

Those two estimates, $\Delta x_{therm.} \gg \Delta x_{dielec.}$ and $t_{therm.} \ll t_{dielec.}$ imply that it is appropriate to consider the thermal mean values rather than the trajectory $x(t)$. On the other hand, it is also necessary to consider the thermal mean values instead of just the values at absolute zero, as the ions experience a much wider range of the potential than under an electric field at absolute zero.

This is especially crucial for nonlinear restoring forces: When a linear restoring force counterbalances an electric force, the thermal mean value of the displacement at a finite temperature T, $\langle x_{T>0} \rangle$, is just equal to the displacement at absolute zero, $x_{T=0}$. However, this does not hold any longer for a nonlinear restoring force:

$$\langle x_{T>0} \rangle \neq x_{T=0} \tag{2.4.55}$$

Boltzmann distribution in an anharmonic potential

As discussed above, it is possible but also necessary to consider thermal mean values in the microwave range. A potential with a third order nonlinear restoring force and an electric field reads:

$$U(x) = qE_{loc}x + \frac{1}{2}k_1x^2 + \frac{1}{4}k_3x^4 \tag{2.4.56}$$

E_{loc} is the local electric field. The expectation value of x in this potential cannot be computed analytically. However, setting $k_1 = 0$ and $k_3 > 0$ enables analytic solutions that are helpful to observe the dependencies on different variables. Under these assumptions, $\langle x \rangle$ has the form:

$$\langle x \rangle = \frac{\int \mathrm{d}x\ x\ \exp[-\beta(\frac{k_3}{4}x^4 + qxE_{loc})]}{\int \mathrm{d}x\ \exp[-\beta(\frac{k_3}{4}x^4) + qxE_{loc})]} \tag{2.4.57}$$

Here, $\beta = 1/(k_\mathrm{B}T)$ For simplicity, the intricate explicit form of $\langle x \rangle$ is omitted and only the power series expansion up to the third order is stated:

$$p = q\langle x \rangle = 2\frac{\Gamma(3/4)}{\Gamma(1/4)}\sqrt{\frac{\beta}{k_3}}q^2E_{loc} - \left(2\frac{\Gamma(3/4)^2}{\Gamma(1/4)^2} - \frac{1}{6}\right)\frac{\beta^2}{k_3}q^4E_{loc}^3 \tag{2.4.58}$$

Here, Γ is the Euler Gamma-function. In a numerical representation, the polarizabilities of this system yield:

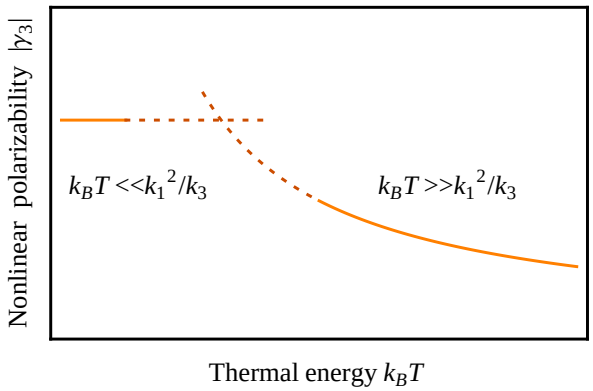

Figure 2.16: Nonlinear response of an anharmonic oscillator in the low temperature and high temperature limit. The response at temperatures different from zero is smaller than the nonlinear response at $T = 0$.

$$\begin{aligned} \gamma_1 &= 0.676 \frac{q^2}{\sqrt{k_3 k_\mathrm{B} T}} \\ \gamma_3 &= -0.062 \frac{q^4}{k_3 (k_\mathrm{B} T)^2} \end{aligned} \tag{2.4.59}$$

Even though the original potential had no linear response at all, the effective potential, which the particle experiences at $T > 0$, has a linear restoring force. Even more so, the nonlinear polarizability γ_3 decreases stronger than the linear polarizability γ_1 with increasing k_3. Hence, steepening the potential leads to a more linear response. The restoring force due to the thermal occupation of the nonlinear potential can dominate the actual linear restoring k_1. This is the case for high temperatures. Here, the linear contribution k_1 can be neglected, as in Equation 2.4.57. For low temperatures, the $T = 0$ model (Equation 2.4.35) becomes more appropriate. This is sketched in Figure 2.16. This calculation suggest that the nonlinearities originating from nonlinear potentials are largest at $T = 0$ and that thermal occupation "linearizes" the nonlinear response, even though the thermal energy allows the particle to experience more of the potential landscape with larger amplitudes, which intuitively would result in a more nonlinear response.

Still, taking the values from Equation 2.4.37 and Equation A.0.4 reveals $k_\mathrm{B} T \ll k_1^2/k_3 \approx 10\,\mathrm{eV}$ for ambient temperature. Hence, for the nonlinear response it is appropriate to assume $T = 0$, even though $\Delta x_{therm.} \gg \Delta x_{dielec.}$

Charge in a box

This model is motivated by a locally free charge that diffuses on a much smaller time scale than the period of the applied electric field. Such locally mobile charges are known to exist in glasses in form of electrons or even ions [Ste80]. The potential is assumed to be of the form of a box of width b:

$$U(x) = \begin{cases} \infty & \text{for } x < -b/2 \\ 0 & \text{for } -b/2 < x < b/2 \\ \infty & \text{for } x > b/2 \end{cases} \tag{2.4.60}$$

Under an electric field E_{loc}, the partition function of this potential is:

$$Z = \int_{-b/2}^{b/2} \mathrm{d}x \, \exp(-\beta q x E_{loc}) \tag{2.4.61}$$

The expectation value $\langle x \rangle$ is obtained via:

$$\langle x \rangle = \frac{1}{qE_{loc}} \frac{\partial}{\partial \beta} \ln(Z), \tag{2.4.62}$$

which results in the Langevin function $\mathrm{Lgv}(a)$ with $a = \frac{bqE}{2k_\mathrm{B}T}$. The induced dipole p becomes:

$$p = q\langle x \rangle = \frac{bq}{2} \mathrm{Lgv}(a) \tag{2.4.63}$$

The polarizabilities are obtained from the power series expansion of the polarization p and read:

$$\begin{aligned} \gamma_1 &= \frac{1}{12} \frac{b^2 q^2}{k_\mathrm{B}T} \\ \gamma_3 &= -\frac{1}{720} \frac{b^4 q^4}{(k_\mathrm{B}T)^3} \end{aligned} \tag{2.4.64}$$

Binary state system

A very similar model is a flipping model between just two states: a charge q can be either at position $-d/2$ or $d/2$. These states have opposing dipoles $qd/2$. For simplicity, there is no a priori energy difference, so if no field is applied, the two states are equally occupied. The model is equivalent to any standard two state thermal population model. The heat capacity anomaly at low temperatures in glasses motivates the existence of such states [SRTO94]. Its total dipole is given as the sum of the two opposed dipole states:

$$p = q\frac{d}{2} \left(\frac{\exp(-\beta dqE)}{1 + \exp(-\beta dqE)} \right) - q\frac{d}{2} \left(\frac{1}{1 + \exp(-\beta dqE)} \right) \tag{2.4.65}$$

$$p = \frac{1}{2} d \; q \left(\frac{\exp(-\beta dqE) - 1}{\exp(-\beta dqE) + 1} \right) = \frac{d}{2} q \; \tanh\left(\frac{\frac{d}{2} qE}{k_\mathrm{B}T} \right) \tag{2.4.66}$$

The polarizabilities γ are obtained from the power series expansion of the polarization p and read:

$$\begin{aligned}\gamma_1 &= \frac{1}{4}\frac{d^2q^2}{k_\mathrm{B}T} \\ \gamma_3 &= -\frac{1}{24}\frac{d^4q^4}{(k_\mathrm{B}T)^3}\end{aligned} \tag{2.4.67}$$

2.4.8 Magnetic Nonlinearity

So far, the discussion dealt with dielectric nonlinear responses. However, the method of coupled dielectric resonators (subsection 3.5.1) does not allow a strict separation between dielectric and magnetic properties, as magnetic and electric fields alternate (see subsection 3.2.2). Therefore, intermodulation generation by magnetic nonlinearities cannot be excluded: If all magnetic dipole moments in the material are aligned, the magnetization is saturated, corresponding to a strong nonlinear response. Similar to Equation 2.2.16, the magnetization M can be written in terms of the magnetic field H and the magnetic susceptibilities χ_i^m:

$$M(H) = \chi_1^m H + \chi_3^m H^3 + ... \tag{2.4.68}$$

The magnetic nonlinear response is compared with the electric nonlinearity by introducing a equivalent electric nonlinearity $\chi_3^{e,eq.}$:

$$\chi_3^{e,eq.} E^2 = \chi_3^m H^2 \tag{2.4.69}$$

To translate the magnetic field into an electric, comparable energy densities are assumed, which is reasonable for dielectric resonators:

$$\frac{1}{2}\mu_r\mu_0 H^2 = \frac{1}{2}\varepsilon_r\varepsilon_0 E^2 \tag{2.4.70}$$

Inserting Equation 2.4.70 into Equation 2.4.69 gives:

$$\chi_3^{e,eq.} = \frac{\varepsilon_r\varepsilon_0}{\mu_r\mu_0}\chi_3^m \tag{2.4.71}$$

For the estimation, a paramagnetic material with noninteracting spins is assumed. Thus, the magnetization M is given by:

$$M = Nm\mathrm{Lgv}(x) \tag{2.4.72}$$

Here, N is the density of magnetic dipoles and $\mathrm{Lgv}(x)$ the Langevin function, with $x = mB/(k_\mathrm{B}T)$. m is a single magnetic dipole moment. Assuming $\mu_r = 1$, the magnetic flux density can be written as $B = \mu_0 H$. Hence, the power series of the magnetization including the first nonlinear term of the Langevin function reads:

$$M = Nm^2\frac{\mu_0}{3k_BT}H - Nm^4\frac{\mu_0^3}{45(k_BT)^3}H^3 \tag{2.4.73}$$

This allows obtaining the nonlinear magnetic susceptibility χ_3^m

$$\chi_3^m = -Nm^4 \frac{\mu_0^3}{45(k_B T)^3} \tag{2.4.74}$$

Equation 2.4.71 is used to translate the magnetic into the equivalent nonlinear electric susceptibility $\chi_3^{e,eq.}$. Again, μ_r is set to unity.

$$\chi_3^{e,eq.} = -Nm^4 \frac{\varepsilon_r \varepsilon_0 \mu_0^2}{45(k_B T)^3} \tag{2.4.75}$$

To estimate the influence of the magnetic nonlinear response by magnetic dipole saturation, fused silica (density $\rho = 2203$ kg/m^3, molar mass $M_m = 0.030$ kg/mol, relative permittivity $\varepsilon_r = 3.75$) is contaminated with $x = 1000$ ppm of iron. Iron has a magnetic dipole moment corresponding to $m = 6\,\mu_\mathrm{B}$, with μ_B being the Bohr magneton. With these values, the density of magnetic dipoles can be estimated with $N = xN_A\rho/M_m$ with the Avogadro constant N_A. One obtains $\chi_3^{e,eq.} = -5 \times 10^{-27}\,\mathrm{m}^2/\mathrm{V}^2$. This nonlinearity is far below dielectric nonlinearities discussed so far, despite assuming a high proportion of iron doping. From this estimate, it seems reasonable to neglect nonresonant magnetic nonlinearities.

2.4.9 Linear Microwave Dielectric Properties

A brief introduction into the linear properties of microwave dielectric is necessary before dealing with nonlinear responses. The linear properties of microwave materials, the relative permittivity ε_r and the loss tanδ, have already been thoroughly studied theoretically and experimentally. The permittivity ε_r can be influenced by only a few parameters [RI06]: It increases with either greater ionic polarizability or a smaller unit cell volume, corresponding to packing more charges in the same volume. The dielectric loss tanδ on the other hand has far more complex causes and is therefore still subject to research [RI06], especially for low losses dielectrics.

The very baseline for damping is the anharmonicity of the ionic potentials. These anharmonicities cause coupling to acoustic modes and transfer energy to these modes, corresponding to energy conversion into heat [GT91]. This fundamental relation of nonlinearity and loss was also proposed by [THNW89] to be the source of the dielectric nonlinearity that they measured in their sintered ceramics.

Although this fundamental loss is always present, usually other types dominate the dielectric loss [Seb08]. Dominant losses are due to lattice defects, such as impurities, microstructural defects, grain boundaries, porosity, microcracks, disorder [ZWKU97, Sch64, MTHT95, Tam06], random crystalline orientation, dislocations, and oxygen vacancies [RI06]. Additionally, electronic spin flips were found to be responsible for dielectric loss [LFN12].

2.4.10 Low Frequency Nonlinear Dielectric Properties

Nonlinear dielectric responses have been investigated at low frequencies ($\sim$ kHz) for applications of metal-isolator-metal capacitors (MIMs). In contrast to voltage tunable varactors, which can be realized with ferroelectrics, MIMs based on dielectrics are designed for linear applications. MIMs can be found in integrated circuits (IC) serving for analog-to digital converters, DC voltage decoupling, electrostatic discharge protection and dynamic random access memory [JACJ+19]. The nonlinear voltage response of MIMs is especially critical for radio frequency analog and mixed signal ICs and the fundamental origin of the nonlinear response is still under debate [JACJ+19].
MIMs are required to show a high capacitance density, which favors thin isolator sheets ($7\,\mathrm{nm} \sim 30\,\mathrm{nm}$). These sheets are bottom-up manufactured by physical vapor deposition. In return, the thin sample leads to high electric fields, which provoke nonlinear responses even at low voltages ($1\,\mathrm{V}/10\,\mathrm{nm} = 100\,\mathrm{kV/mm}$). The capacitance of MIMs is usually characterized with a DC bias voltage and a kHz test signal. The figure of merit that is used to describe the nonlinear response is based on the change in capacitance C with the applied voltage V:

$$\frac{\Delta C}{C_0} = \beta_{\mathrm{VCC}} V + \alpha_{\mathrm{VCC}} V^2 \tag{2.4.76}$$

Here, C_0 is the capacitance at $V = 0\,\mathrm{V}$. For setups with inversion symmetry, β_{VCC} is expected to be zero (see subsection 2.2.4). Most measurements confirm a negligible β_{VCC} [AHHC17, PSW+11, BDB09, WLL+08].
Comparing the nonlinear capacitance relation in Equation 2.4.76 to the nonlinear susceptibility in Equation 2.2.16 leads to the following translation:

$$\chi_3 = \varepsilon_r \left(\frac{E_{ext}}{E_{mac}}\right)^2 \frac{\alpha_{\mathrm{VCC}}}{d^2} = \varepsilon_r^3 \frac{\alpha_{\mathrm{VCC}}}{d^2} \tag{2.4.77}$$

Here, it is important to include the de-electrification field in the capacitor geometry (see subsection 2.2.2). Typical nonlinear voltage responses lie in the order of $\alpha_{\mathrm{VCC}} \approx 100\,\mathrm{ppm/V^2}$. For an estimate with $\varepsilon_r = 10$ and $d = 10\,\mathrm{nm}$, this leads to a nonlinear susceptibility of $\chi_3 \approx 10^{-17}\,\mathrm{m^2/V^2}$. This estimate is especially sensitive to ε_r (see Equation 2.4.77). In [BCA06], a value of $\chi_3 \approx 10^{-16}\,\mathrm{m^2/V^2}$ for an Al_2O_3 based MIM was presented, which was reproduced by [AHHC17] though [WLL+08] obtained half their value. [WLL+08] furthermore presents the nonlinear response of further metal oxides up to $\chi_3 = 10^{-14}\,\mathrm{m^2/V^2}$ for $Pr_2Ti_2O_7$ ($\varepsilon_r = 27$) with a linear correlation of higher nonlinearity for higher permittivity.
A majority of dielectrics exhibit a positive α_{VCC} [JACJ+19]. However, SiO_2 ($\chi_3 \approx -10^{-18}\,\mathrm{m^2/V^2}$), crystalline $SrTiO_3$ and a few other materials are known to show a negative α_{VCC} [PSW+11, BDB09]. The sign of α_{VCC} in $SrTiO_3$ was even shown to reverse after crystallization [BDB09] (amorphous $\chi_3 \approx 10^{-14}\,\mathrm{m^2/V^2}$, crystallized $\chi_3 \approx -10^{-11}\,\mathrm{m^2/V^2}$). By compensating the nonlinear responses of different dielectrics, highly linear MIMs were obtained [KCL+04].

A variety of mechanisms has been proposed for being responsible for nonlinear voltage response in MIMs: metal oxygen bond polarizability [BCA06], thermodynamic relation of the susceptibility similar to that of the thermal expansion [Blo07], electrostriction and Maxwell stress [WLL+08], dipolar orientation [PSW+11] and interface effects such as double layer formation [VGJEK10] and lateral expansion induced stress [AHHC17]. MIMs are based on dielectrics and are designed for a linear response. However, nonlinear dielectric responses are also investigated at material classes that show nonlinearity as a dominant property: Ferroelectrics, relaxors and dipolar glasses [MDK11]. All these material classes consist of permanent electric dipoles, which form domains on different spatial scales. The larger the domain size, the larger the nonlinearity. The materials measured in [MDK11] exhibit a $\chi_3 \approx 10^{-6}\,\mathrm{m^2/V^2}$ for ferroelectrics, $\chi_3 \approx 10^{-7}\,\mathrm{m^2/V^2}$ for relaxor ferroelectrics and $\chi_3 \approx 10^{-9}\,\mathrm{m^2/V^2}$ for dipolar glasses. In contrast to other nonlinear measurements, [MDK11] does not use static bias field but instead probes at AC electric field amplitudes of $0.5\,\mathrm{V/mm} \sim 5\,\mathrm{V/mm}$ and measures harmonics.
Finally, a brief summary of nonlinear dielectric spectroscopy at polar liquids shall be given. These measurements are usually performed in the Hz to kHz range, though extensions to the MHz range and even beyond have been developed [HDM75, VH88]. Typically, relative changes in the capacitance of 10^{-3} at electric field amplitudes of $10\,\mathrm{kV/mm}$ are measured over samples of $10\,\mu\mathrm{m}$ [Ric17]. This corresponds to nonlinear susceptibilities in the order of $\chi_3 \approx 10^{-17}\,\mathrm{m^2/V^2}$. Two major effects that contribute to the nonlinear response with opposite signs have been identified: Langevin-like dipole orientation saturation (negative) and chemical equilibrium shift (positive) [Ric17].
The re-entrant cavity developed in [VH88] enabled measuring nonlinear dielectric responses up to $3\,\mathrm{GHz}$ with quasi-static bias field of $10\,\mathrm{kV/mm}$ and a sensitivity of 10^{-5} to the relative change in the permittivity [DSKJH96, KJDH98, KJH01, KJH02]. For $\varepsilon_r = 10$, this corresponds to a sensitivity down to $\chi_3 = 10^{-16}\,\mathrm{m^2/V^2}$.

Chapter 3

Methods

3.1 Microwave Techniques

This section introduces the methodology of microwave equipment, such as signal generators and amplifiers, network analyzers, signal analyzers and filters.

3.1.1 Signal Generators and Amplifiers

Classical microwave sources are electron tubes such as the magnetron, klystron and gyrotron. They were first used to produce microwaves and are still used for high power microwaves. Nevertheless, they are unsuitable for narrowband and phase stable microwave generation. Instead, microwave signals are produced by active nonlinear devices such as diodes or transistors in conjunction with a passive circuit such as crystal resonators [Poz11]. Higher frequencies are achieved by phase locked loops or nonlinear frequency multipliers. Amplifiers used to be vacuum tubes but today transistor (solid state) devices can be used to frequencies above 100 GHz.

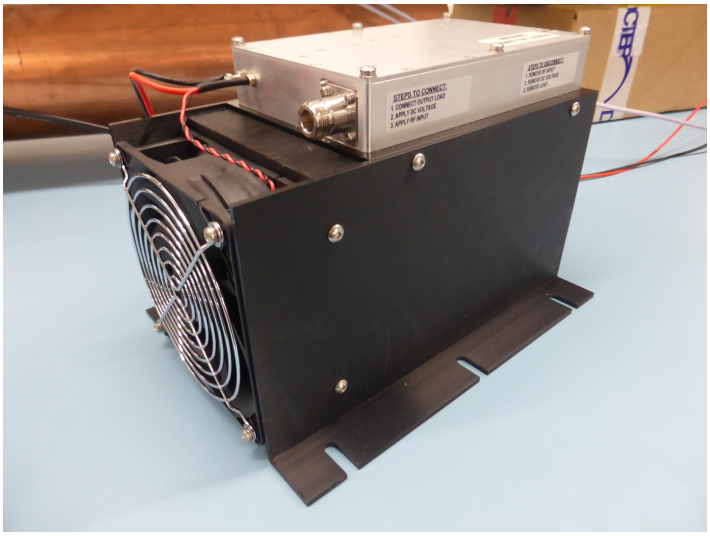

Figure 3.1: Solid-state amplifier mounted on air cooled heat sink for cooling.

Figure 3.1 shows a ZHL-100W-13+ amplifier by Mini Circuits with a nominal frequency span from 750 to 1050 MHz and a typical gain of 50 dB delivering up to 100 W corresponding to 50 dBm. Together with the noise discussed in subsection 3.1.3, this limits the range of the main setup in this work.

3.1.2 Network Analyzers and S-Parameters

Networks are usually described by ratios between their input waves a_i and output waves b_i. This ratio can be formulated in a variety of different parameters. For this work, the classical scattering parameters (or just S-parameters) S_{ji} are best suited. S-parameters are directly displayed by Vector Network Analyzers (VNA). They are ratios of incoming power wave a_i and the outgoing power wave b_j at port i and j [Poz11]. The power waves are measured in $\sqrt{\text{W}}$. An abstract two-port network is sketched in Figure 3.2.

Figure 3.2: A two-port network with ports 1 and 2 and incoming power waves a and outgoing power waves b.

In general, the scattering parameters are complex as the incoming and outgoing signals have a phase. A two-port system can be described by four S-parameters:

$$\begin{pmatrix} b_1 \\ b_2 \end{pmatrix} = \begin{pmatrix} S_{11} & S_{12} \\ S_{21} & S_{22} \end{pmatrix} \begin{pmatrix} a_1 \\ a_2 \end{pmatrix} \tag{3.1.1}$$

If a signal is applied at port 1 and no signal at port 2 ($a_2 = 0$), Equation 3.1.1 can be simplified to a transmission parameter S_{21} and a reflection parameter S_{11} only:

$$S_{21} = \left.\frac{b_2}{a_1}\right|_{a_2=0}, \; S_{11} = \left.\frac{b_1}{a_1}\right|_{a_2=0} \tag{3.1.2}$$

S-parameters are dimensionless. The square of the S-parameters corresponds to the power ratio:

$$|S_{ji}|^2 = \frac{P_{j,out}}{P_{i,in}} \tag{3.1.3}$$

S-parameters are usually represented on the dB-scale. Applying the logarithm to Equation 3.1.3 yields:

$$20 \log(S_{ji}) = 10 \log(P_{j,out}) - 10 \log(P_{i,in}) \tag{3.1.4}$$

Together with $S_{ji}[\text{dB}] = P_{j,out}[\text{dBm}] - P_{i,in}[\text{dBm}]$ the transformation of the S-parameter from linear to logarithmic is:

$$S_{ji}[\text{dB}] = 20\ \log(S_{ji}) \tag{3.1.5}$$

If no signal is applied at port j, the output power $P_{i,out}$ is just the reflected power $P_{i,ref} = P_{i,out} = S_{ii}^2\ P_{i,in}$. Energy conservation leads to the absorbed power $P_{i,abs}$:

$$P_{i,abs} = P_{i,in} - P_{i,out} = (1 - |S_{ii}|^2)\ P_{i,in} \tag{3.1.6}$$

3.1.3 Signal Analyzers and Bandwidth

This work aims to perform high sensitivity measurements with noise limiting the sensitivity. Therefore, the most important terms of noise and bandwidth are briefly introduced in this section. Together with the maximum amplifier power introduced in subsection 3.1.1, this limits the range of the main setup in this work.

Thermal Noise and Displayed Average Noise Level (DANL)

The ultimate limit for measuring small signals is the thermal noise. For frequencies smaller than $k_\text{B}T/h$, which lies at about 6 THz at room temperature, the energy per frequency bandwidth is rather constant [Poz11]. At ambient temperature, it is given by:

$$P/\Delta f = k_\text{B}T = -174\ \text{dBm/Hz} \tag{3.1.7}$$

Due to additional noise sources, spectrum analyzers however have a higher noise floor, the Displayed Average Noise Level (DANL). The Analyzer N9020A by Agilent Technologies used in this work enables to detect signals down to $-140\,\text{dBm/Hz}$ in FTT-mode (see below).

Resolution Bandwidth (RBW)

The DANL is given in dBm/Hz. It incorporates a dependency on the bandwidth of the filter that is used for scanning the signal, the resolution bandwidth (RBW). Larger RBW allow quicker measurements with an increased noise floor. Smaller RBW decrease the noise level, however, the scanning time increases. Furthermore, the RBW sets the resolution limit at which two signals can be separated in frequency.

Video Bandwidth (VBW)

The VBW averages the noise after detection. A small VBW leads to a smoother displayed signal and can be used to distinguish noise peaks from permanent peaks.

Both larger RBW and VBW decrease the sensitivity of the analyzer. However, a tradeoff needs to be found, as the scanning time increases rapidly with the bandwidth [Key14]:

$$t_\text{sweep} \sim \frac{\Delta f}{\text{RBW VBW}} \tag{3.1.8}$$

For small bandwidths, the analyzer can change to a FFT mode. A time series of the signal is digitally stored in the signal analyzer and analyzed with Fast-Fourier-Transform. It increases sensitivity but with the cost of a reduced dynamic range.

3.1.4 Filters

Filters are essential components in microwave techniques. While lumped components filter techniques are still feasible up to several hundred MHz, their performance decreases at higher frequencies. Microwave filters are based on planar filters, cavity or dielectric resonators (see subsection 3.2.2) and electroacoustic filters such as surface acoustic wave (SAW) or bulk acoustic wave (BAW) structures [DCS+19]. Filters are mainly characterized by their center frequency, insertion loss and bandwidth. As long as space is not a limiting factor, cavity resonators outperform all other resonators in insertion loss, tunability and power handling, though dielectric resonators show better temperature stability [Seb08]. For this work, a 5BT-500/1000-1N/N cavity resonator by K&L with a tunable 1% nominal 3 dB bandwidth between 500 MHz and 1000 MHz being able to handle continuous wave power up to 10 W = 40 dBm was best suited. Figure 3.3 shows an image of this filter.

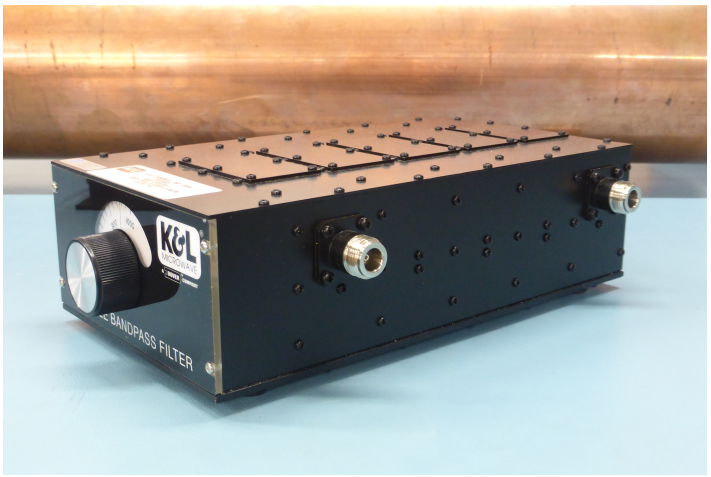

Figure 3.3: Tunable band pass filter (BPF) with manual dial for tuning.

3.2 Microwave Resonators

This section deals with the concepts of waveguides, cavities and dielectric resonators. The central experimental setup of this work (see subsection 3.5.1) is based on these concepts. Resonator losses and excitation is discussed. At the end of the section, the Split Post Dielectric Resonator, which is used for linear dielectric characterization in this work, is introduced.

3.2.1 Waveguides and Cavities

Maxwell's equations induce Helmholtz equations for the electric field **E** and magnetic field **H** in a homogeneous medium [KG86]. These are:

$$(\nabla^2 + k^2)\varphi = \mathbf{0} \tag{3.2.1}$$

Here, φ is either the electric field **E** or the magnetic field **H**. The time dependency $e^{-i\omega t}$ has already been separated. k is the material dependent wave vector:

$$k = \frac{2\pi}{\lambda} = \frac{2\pi\sqrt{\varepsilon_r}}{c_0} f \tag{3.2.2}$$

Here, ε_r is the relative permittivity, c_0 the vacuum velocity of light and f the frequency of the wave. As the experimental setup (see subsection 3.5.1) reveals cylindrical symmetry, the Laplace operator in Equation 3.2.1 is written in cylindrical coordinates. The radial direction is termed r, the axis of rotation z and the angle of rotation ϕ:

$$\frac{1}{r}\,\partial_r(r\,\partial_r\varphi) + \frac{1}{r^2}\,\partial_\phi^2\varphi + \partial_z^2\varphi + k^2\,\varphi = 0 \tag{3.2.3}$$

By using the separation ansatz $\varphi(r, z, \phi) = P(r)Z(z)\Phi(\phi)$ the equation rearranges to:

$$\frac{1}{r}\,\partial_r(r\,\partial_r P) + ((k_r r)^2 - m^2) = 0 \tag{3.2.4}$$

Here, k_r is the radial wave vector. The wave vector in z direction is usually called propagation constant k_z, separated in the following equation:

$$\frac{d^2 Z}{dz^2} = -k_z^2 Z \tag{3.2.5}$$

This differential equation is solved by a plain wave $Z(z) = e^{-ik_z z}$. For k_z being imaginary, this will correspond to an exponential attenuation. m represents the tangential wave number, separated in the following equation:

$$\frac{d^2\Phi}{d\phi^2} = -m^2\Phi \tag{3.2.6}$$

Equation 3.2.4 is a Bessel differential equation of degree m solved by Bessel functions of the first kind $J_m(k_r r)$. For k_r becoming imaginary, they change to the modified Bessel functions of the second kind $K_m(k_r r)$. The squares of k_r and k_z add up to the total wave vector k:

$$k^2 = k_r^2 + k_z^2 \tag{3.2.7}$$

A certain frequency f is put in the system, resulting in a certain wave vektor k. This k needs to be distributed between k_r and k_z. In a circular waveguide with metallic boundary conditions allowing only certain values of k_r, there are two possibilities: Either $k_r < k$ and k_z is a real number, resulting in a propagating wave in z, or $k_r > k$, forcing

k_z to be imaginary. Thus, the wave is attenuated in z, a so-called evanescent wave. Hence, only wave vectors above a certain value k_{cut} lead to a propagating wave within a waveguide. The corresponding frequency is called cutoff frequency f_{cut}. The modes can be separated into two classes: transverse electrical (TE) with $E_z = 0$ and transverse magnetic (TM) with $H_z = 0$. Each mode has its own cutoff frequency:

$$f_{mn} = \frac{c_0}{2\pi} \frac{1}{\sqrt{\varepsilon_r}} \frac{x_{mn}}{R} \tag{3.2.8}$$

Here, x_{mn} stands for the nth root of the mth degree Bessel functions J_m for TM-modes and of the derivative of the mth degree Bessel function J'_m for TE-modes. The modes are therefore given two subscripts m and n, e.g. TE_{01}. R is the radius of the cylindrical waveguide. A cross section of two important modes is shown in Figure 3.4. Inserting numerical values for the Bessel roots, the cutoff frequencies of a cylindrical waveguide filled with vacuum (or air) are given by:

$$\begin{aligned} f_{cut}(\mathrm{TE}_{11}) &= \frac{c_0\ 1.841}{2\pi R} \\ f_{cut}(\mathrm{TE}_{01}) &= \frac{c_0\ 3.832}{2\pi R} \end{aligned} \tag{3.2.9}$$

By closing the waveguide at both ends, also the z direction is restricted to certain k_z. The created cavity of length d has a set of resonance frequencies:

$$f_{mnp} = \frac{c_0}{2\pi} \frac{1}{\sqrt{\varepsilon_r}} \sqrt{\frac{x_{mn}^2}{R^2} + \frac{p^2\pi^2}{d^2}} \tag{3.2.10}$$

The resonant modes are again labeled TE or TM, but with a third subscript p. The $p\pi/d$ term originates from sinusoidal field distribution along the z-axis.

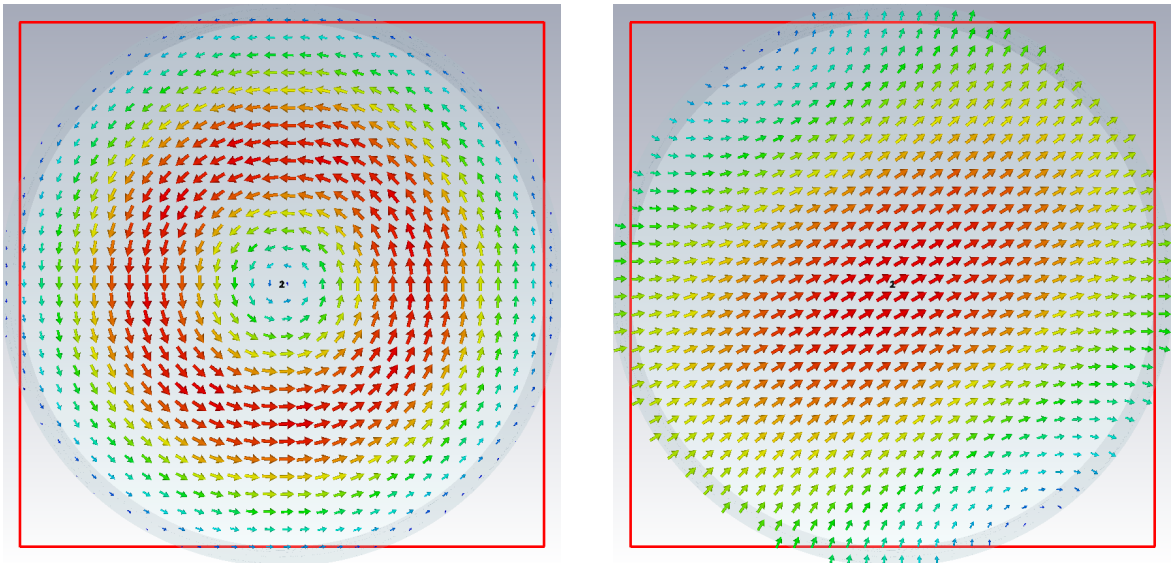

(a) Electric field **E** of the TE_{01}-mode. (b) Electric field **E** of the TE_{11}-mode.

Figure 3.4: Simulated fields of two modes in a cylindrical waveguide.

3.2.2 Dielectric Resonators

It was already shown in 1939 that dielectric objects of the size comparable to the microwave wavelength can serve as resonators at these frequencies [Ric39]. Moreover, dielectric objects radiate energy into free space. In contrast to the potential well and the Schrödinger equation in quantum mechanics, no bound state exists. Hence, the eigenvalues cannot be purely real but always have an imaginary part [KG86]. The resonances are then defined as the minima of the imaginary part, the loss $1/Q$, or maxima in Q. This loss due to radiation is labeled $1/Q_r$.
Nevertheless, under metallic boundary conditions, the radiation loss is zero. The eigenvalues become real, which makes bound states possible, comparable to the potential well in quantum mechanics. As the setup in this work has a complete metal enclosure, this case is discussed in more detail below.
Going back to Equation 3.2.7 and Equation 3.2.2, k depends on the relative permittivity ε_r. In a dielectric with $\varepsilon_r > 1$, a lower frequency f is needed to exceed the cutoff wave vector k_{cut}. Hence, it is possible that a solution for the electric and magnetic field with real wave vectors k_r and k_z exists within the dielectric, while outside the dielectric the fields are still evanescent.
The modes of dielectric resonators are named similarly to the cavity modes. However, as fields extend outside the resonator, the dielectric contains less than a half wavelength. This is denoted by a third subscript δ being smaller than unity. In contrast to cavity resonators, it is no longer possible to separate in TE and TM modes for $m \neq 0$. As higher modes include both transverse magnetic and transverse electric fields, they are called hybrid electromagnetic (HEM). Field plots for two important modes are shown in Figure 3.5.
In spite of the cylindrical symmetry, the solution of the Helmholtz equation for dielectric resonators turns out to be very complex [KG86]. Various analytical approaches try to model the system as close as possible with suitable assumptions [Coh68, She07]. However, all models require numerical solutions of an implicit equation in the end. Nevertheless, finite element methods (FEM) predict field distributions and resonance frequencies with sufficient precision. The field distributions in Figure 3.5 originate from such FEM simulations with CST Microwave Studio. Figure 3.6 shows a more quantitative picture of the $\mathrm{TE}_{01\delta}$-mode field distribution.
A rule of thumb for the $\mathrm{TE}_{01\delta}$-mode resonance frequency of a free dielectric resonator [KG86] is given by:

$$f = \frac{34\,\mathrm{mm\ GHz}}{a\sqrt{\varepsilon_r}} \left(\frac{a}{L} + 3.45\right) \tag{3.2.11}$$

Here, a and L are the radius and the length of the cylindrical resonator, respectively. This rule has an accuracy of 2 % within $0.5 < a/L < 2$ and $30 < \varepsilon_r < 50$. When metallic shields are brought towards the resonator, it can be shown with perturbation calculations that the resonance frequency shifts upwards if the excluded volume contains more magnetic than electric energy [KG86]. As the electric energy is mostly located in

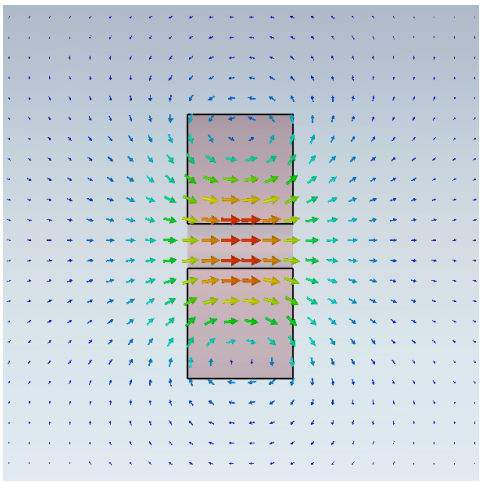

(a) Magnetic field **H** of the $TE_{01\delta}$-mode.

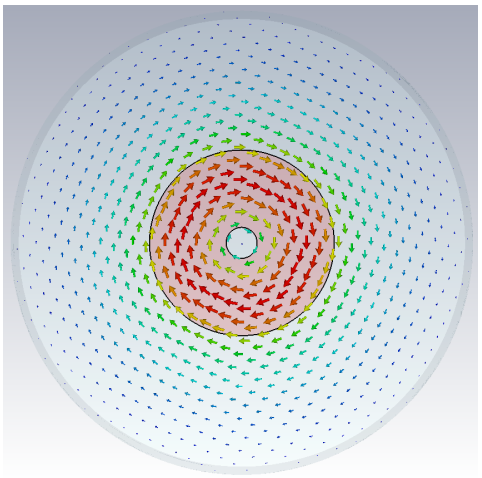

(b) Electric field **E** of the $TE_{01\delta}$-mode.

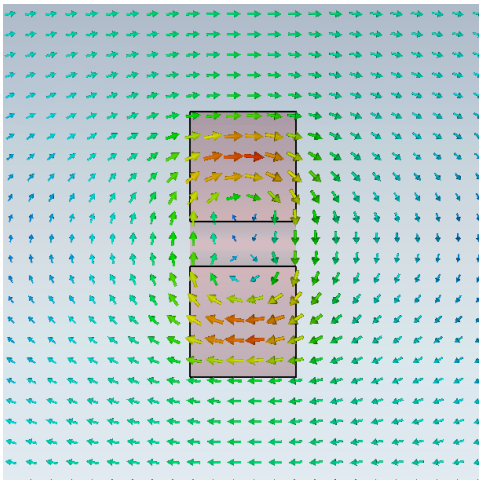

(c) Magnetic field **H** of the $HEM_{11\delta}$-mode.

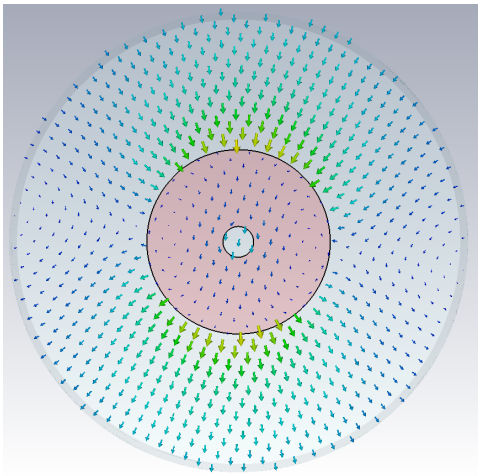

(d) Electric field **E** of the $HEM_{11\delta}$-mode.

Figure 3.5: Simulated fields of the two lowest modes of a cylindrical dielectric resonator for a dielectric of $\varepsilon_r = 32$ of length $L = 24\,\text{mm}$ and of radius $a = 30\,\text{mm}$ in a cylindrical waveguide of radius $R = 75\,\text{mm}$. The resonance frequency of the $TE_{01\delta}$-mode is 971.6 MHz and 1100.5 MHz for the $HEM_{11\delta}$-mode. The center hole has mechanical support reasons in the experiment.

the resonator itself ($\varepsilon_r \gg 1$) while the magnetic energy is rather distributed all over the volume ($\mu_r = 1$), the resonance frequency is expected to be higher than the estimate with the rule of thumb for a free resonator.

Comparing the fields in Figure 3.4 and Figure 3.5, the TE_{01}-mode of the waveguide has a similar field distribution as the $TE_{01\delta}$-mode of the dielectric resonator. This leads to a strong coupling of the TE_{01}-mode of the resonator to the $TE_{01\delta}$-mode of the resonator. In the same way, the field distributions of the TE_{11}-mode of the waveguide and the $HEM_{11\delta}$-mode are akin and excite each other.

For the dielectric resonator, the $TE_{01\delta}$-mode has a lower frequency than the $HEM_{11\delta}$-mode. On the other hand, the cutoff frequency of the TE_{11}-mode of the waveguide is lower than of the TE_{01}-mode. This seems contradictory; however, this is due to the

different aspect ratios of the waveguide and the dielectric resonator. Elongating the dielectric resonator leads to the $\mathrm{HEM}_{11\delta}$-mode to be lower [KG86].
The $\mathrm{HEM}_{11\delta}$-mode reveals a degeneracy in the angle. This has a major drawback, as the mode will split into distinct modes when the cylindrical symmetry is broken. One advantage of the $\mathrm{TE}_{01\delta}$-mode is its non-degeneracy [Kru06].
To determine the nonlinear susceptibility, the electric field amplitude in the resonators needs to be known. This section completes by relating the electric field amplitude E to the stored energy W_s in the dielectric resonator. This energy W_s oscillates between the electric and the magnetic field. At a point in time, the energy is only stored in the electric field and the energy W is just the integral of the electric energy density:

$$\begin{aligned} W &= \int_{Cav.} w(\mathbf{x})\ \mathrm{d}V = \int_{Cav.} \frac{1}{2}\varepsilon_0\varepsilon_r(\mathbf{x})\ \mathbf{E}(\mathbf{x})^2\ \mathrm{d}V \\ &= \frac{1}{2}\varepsilon_0\ \hat{E}^2\ \int_{Cav.} \varepsilon_r(\mathbf{x})\ \varphi(\mathbf{x})^2\ \mathrm{d}V \end{aligned} \tag{3.2.12}$$

Here, $\varphi(\mathbf{x})^2 = (\mathbf{E}(\mathbf{x})/\hat{E})^2$ was introduced. $\hat{E}$ is the maximum absolute value of $\mathbf{E}(\mathbf{x})$, hence $-1 < \varphi(\mathbf{x}) < 1$. It is useful to introduce the geometric parameter c_{EW} that relates the electric field maximum $\hat{E}$ in the resonator to the stored energy W_s.

$$\hat{E} = c_{\mathrm{EW}}\ \sqrt{W_s} \tag{3.2.13}$$

This geometric parameter is:

$$c_{\mathrm{EW}} = \sqrt{2 \Big/ \left(\varepsilon_0 \int_{Cav.} \varepsilon_r(\mathbf{x})\ \varphi(\mathbf{x})^2\ \mathrm{d}V\right)} \tag{3.2.14}$$

The $\mathrm{TE}_{01\delta}$-mode has an electric field component in $\hat{e}_\phi$ direction only ($\mathbf{E} = E_\phi \hat{e}_\phi$) with no component in z nor r. The component E_ϕ is plotted in Figure 3.6.

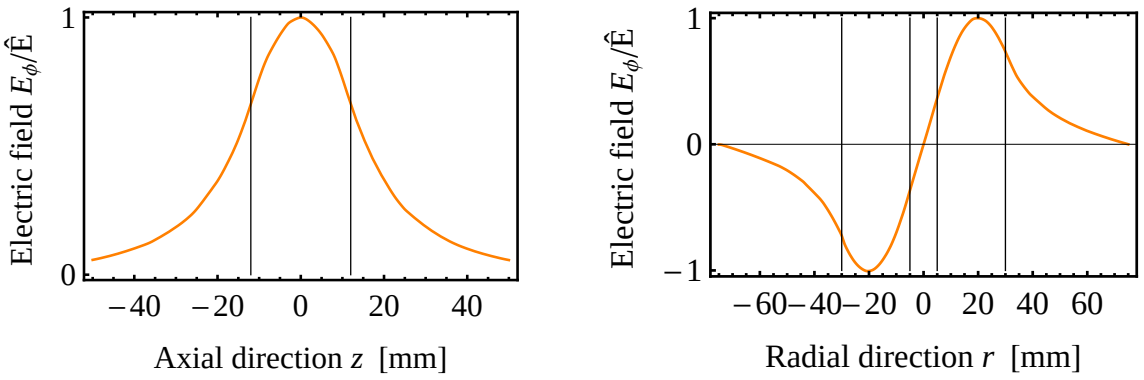

Figure 3.6: Simulated electric field of the $\mathrm{TE}_{01\delta}$-mode of a cylindrical dielectric resonator with outer diameter $D = 60\,\mathrm{mm}$, inner drilling $D_i = 10\,\mathrm{mm}$ and $L = 24\,\mathrm{mm}$ and $\varepsilon_r = 32.0$ in a cylindrical cavity with diameter $D_\mathrm{C} = 150\,\mathrm{mm}$. The vertical lines represent the size of the dielectric resonator.

3.2.3 Resonator Losses

Besides its resonance frequency ω_0, a resonator is characterized by its quality factor Q. It is defined as the ratio between the stored energy W and dissipated energy V per cycle [Jac99]:

$$Q = 2\pi W/V \tag{3.2.15}$$

Q is the resonance enhancement, the ratio between the amplitude at resonance ω_0 and the amplitude at $\omega = 0$. By replacing $V = -2\pi/\omega_0 \frac{\mathrm{d}W}{\mathrm{d}t}$ in Equation 3.2.15, it merges into the differential equation:

$$P = \frac{dW}{dt} = -\frac{\omega_0}{Q} W \tag{3.2.16}$$

This equation is solved by $W(t) = W_0 e^{-\omega_0 t/Q}$. For the amplitude of the electric field, this means:

$$E(t) = E_0 \; e^{-\omega_0 t/(2Q)} e^{-i\omega_0 t} \tag{3.2.17}$$

Here, it is assumed, that there is no essential frequency shift due to damping. This is appropriate for $Q > 300$, as the shift is about 1 kHz at a 1 GHz resonance frequency ($\Delta\omega \approx \omega_0/(8Q^2)$). The Fourier transform of Equation 3.2.17 is given by:

$$E(\omega) \sim \frac{1}{(\omega - \omega_0)^2 + (\omega_0/(2Q))^2} \tag{3.2.18}$$

This corresponds to a Lorentzian profile around the resonance frequency ω_0 with FWHM[1] ω_0/Q. The stronger the system is damped, the broader the peak becomes. So Q can be deduced by measuring the width of the resonance peak when performing a frequency sweep.
There are several factors contributing to the resonator losses: Radiation ($1/Q_r$), finite metallic conductivity ($1/Q_c$) and dielectric losses ($1/Q_d$). All these losses add up to the resonator loss ($1/Q_0$):

$$1/Q_0 = 1/Q_r + 1/Q_c + 1/Q_d \tag{3.2.19}$$

Additionally, any external coupling also shows up as loss $1/Q_{ext}$. The new loss is called the loaded loss $1/Q_l$ of the resonator, in contrast to the unloaded loss Q_0:

$$1/Q_l = 1/Q_0 + 1/Q_{ext} \tag{3.2.20}$$

For a dielectric resonator with no metallic boundaries, the radiation loss Q_r usually accounts for the largest loss. However, in closed metallic cavity the radiation loss is essentially zero [KG86].

[1] Full Width Half Maximum: Peak width at half the maximum level. On the dB scale, this is at −3 dB from the peak maximum.

3.2.4 Resonator Excitation

Among the different methods to excite a resonator, the inductive coupling by a loop is looked at in more detail. A resonator excited by a loop can be modeled by a lumped element circuit. Such representations are shown in Figure 3.7. As a resonator usually has several modes, each single resonator circuit represents a mode of the resonator. Both the descriptions of Figure 3.7a and Figure 3.7b are valid and can be transformed into each other [MDP48].

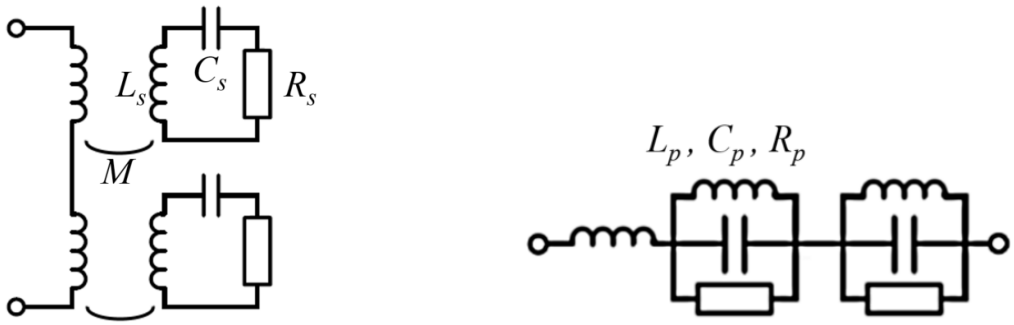

(a) Series resonators with L_s, R_s, C_s (b) Parallel resonators with L_p, R_p, C_p

Figure 3.7: Two valid lumped element circuit representations of a multimode resonator excited by a loop.

The transformation requires definitions of adjusted circuit elements. However, the resonance frequency and the quality factor remain the same:

$$\begin{aligned} \omega_s^2 &= \omega_p^2 = \frac{1}{L_p C_p} = \frac{1}{L_s C_s} \\ Q_s &= Q_p = \omega_p R_p C_p = \frac{\omega_s L_s}{R_s} \\ R_p &= \frac{(\omega M)^2}{R_s} \\ L_p &= \frac{M^2}{L_s} \end{aligned} \tag{3.2.21}$$

Here, M is the exchange inductance of the exciting loop and the resonator inductance. While the representation in Figure 3.7a is more intuitive, the representation in Figure 3.7b is more suitable for calculations. It is a series circuit of parallel resonators. Each parallel resonator contributes with its impedance:

$$\frac{1}{Z(\omega)} = \frac{1}{R_p} + \frac{1}{i\omega L_p} + i\omega C_p \tag{3.2.22}$$

Replacing $\omega_0^2 = 1/(L_p C_p)$ and $Q_0 = \omega_0 R_p C_p$ in a parallel circuit yields:

$$Z(\omega) = \frac{1}{1 + iQ_0\left(\frac{\omega}{\omega_0} - \frac{\omega_0}{\omega}\right)} R_p = \frac{i\omega_0\omega/Q_0}{\omega_0^2 - \omega^2 + i\omega_0\omega/Q_0} R_p \tag{3.2.23}$$

This result allows calculating the reflection S_{ii} of a signal that is fed into the resonator. The reflection depends on the impedance matching:

$$|S_{ii}| = \left|\frac{Z_2 - Z_1}{Z_1 + Z_2}\right| = \left|\frac{\frac{Z_2}{Z_1} - 1}{\frac{Z_2}{Z_1} + 1}\right| = \left|\frac{\kappa - 1}{\kappa + 1}\right| \tag{3.2.24}$$

Here, κ is the so-called coupling parameter[2]. For impedance matching, $\kappa = 1$. $\kappa < 1$ is called subcritical coupling and $\kappa > 1$ overcritical coupling. The transmission line impedance is usually set to $50\,\Omega$. The resonator impedance at resonance is $Z(\omega_0) = R_p$. While R_s is fixed, R_p is adjustable by varying the exchange inductance M. M depends on the perturbation of the resonator mode by the coupling loop. It usually increases with further insertion of the loop to the resonator.
Coupling the resonator to the exterior results in an additional loss:

$$\begin{aligned} Q_0 &= \frac{\omega_0 L_p}{R_p} \\ Q_l &= \frac{\omega_0 L_p}{R_p + Z} \end{aligned} \tag{3.2.25}$$

The loaded loss Q_l is related to the unloaded loss Q_0 by:

$$Q_l = \frac{1}{1 + Z/R_p}\, Q_0 = \frac{1}{1 + \kappa}\, Q_0 \tag{3.2.26}$$

Inverting the relation of S_{ii} and κ in Equation 3.2.24 returns:

$$\kappa = \frac{1 \mp |S_{ii}|}{1 \pm |S_{ii}|} \tag{3.2.27}$$

The upper sign holds for subcritical coupling, the lower sign for overcritical coupling. To obtain the loaded loss Q_l as a function of S_{ii} instead of the coupling parameter κ, insert Equation 3.2.27 in Equation 3.2.26:

$$Q_l = \frac{1 \pm |S_{ii}|}{2}\, Q_0 \tag{3.2.28}$$

Here, "+" applies to subcritical coupling and "−" to overcritical coupling.

Application

As described in subsection 3.5.4, the loaded Q_l of the f_2-mode of the coupled resonators needs to be known to determine the dielectric nonlinearity of the material under test. However, the experimental setup (see subsection 3.5.1) does not allow the determination of Q_l of the f_2-mode by measuring the FWHM of the resonance peak. Instead, it is deduced from S_{22} and the unloaded Q_0. To validate this indirect approach and to check the proper working of the input, the loaded loss Q_l is determined for a single dielectric resonator by measuring the FWHM of the resonance. It is then compared to

[2]The coupling κ is not to be confused with c introduced in subsection 3.4.1. Both are dimensionless but $\kappa \approx 1$ and $c \ll 1$.

the result obtained by Equation 3.2.28. The comparison is shown in Figure 3.8. The agreement is good for low couplings. At high couplings, the FWHM measurements shows a systematic deviation from the prediction by Equation 3.2.28. It is suspected that this is due an onset of additional loss processes that do not contribute to the coupling. The conduction loss of the input system is such a non-contributing loss. If $\kappa > 1$ had been reached, a decrease in Q_0/Q_l would be accompanied by increasing reflection S_{ii}. This was not observed.

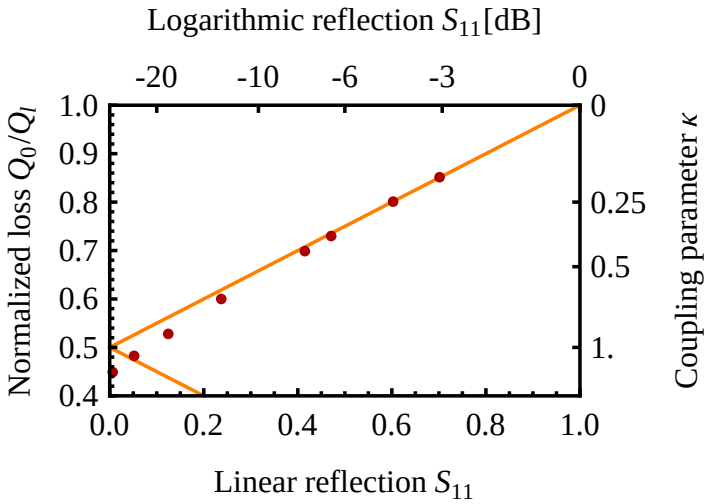

Figure 3.8: Control of the coupling/loss relation Equation 3.2.28. The lines are the prediction for $Q_0 = 1985$. The dots are measured reflections S_{11} and corresponding Q_l determined with the FWHM of the resonance. Q_0 was chosen to match with the small coupling measurements. For strong couplings, the data deviates from the prediction towards lower Q.

3.3 Split Post Dielectric Resonator Method

There is a broad field of linear dielectric characterization setups for the microwave range, each being best suited for different material properties and precision requirements [Seb08]. Besides Fabry-Ferot setups [KSKK18, YMM+15], the Split Post Dielectric Resonator method is most suitable for high precision loss measurements of low permittivity materials [MKJL04]. The principle is sketched in Figure 3.9.

The sample is a thin disc that is inserted via a slit in the fixture into the cavity. A split dielectric resonator is positioned in the center of the cavity. The sample shifts the resonance frequency and the quality factor of the resonance toward lower values. From the shift, the permittivity and the loss of the sample material are determined:

$$\begin{aligned} \varepsilon_r &= 1 + \frac{f_0 - f_s}{h f_0 K_\varepsilon(\varepsilon_r, h)} \\ \tan\delta &= \left(1/Q_u + 1/Q_{\mathrm{DR}} + 1/Q_c\right)/\varphi_e \end{aligned} \tag{3.3.1}$$

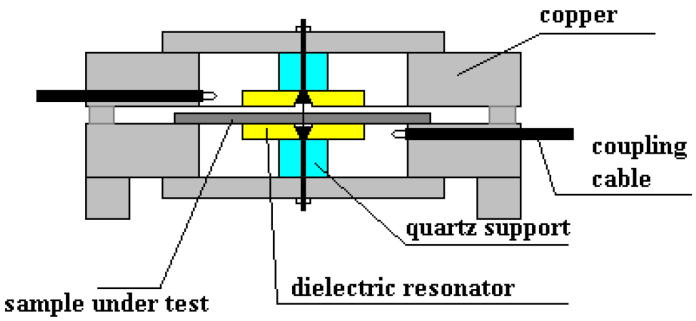

Figure 3.9: Sketch of the split post dielectric resonator dielectric characterization principle [MKJL04].

Here, f_0 is the resonance frequency of the empty cavity, f_s is the resonance frequency with the sample with thickness h. K_ε is a function that corrects for the changes in the electric field geometry in the cavity. The equation for ε_r is solved iteratively. Q_u and Q_{DR} denote the quality factor without and with the sample. Q_c^{-1} is the conduction loss and φ_e is an electric energy filling factor from the sample. Being a resonant method, each frequency point requires a differently sized fixture.

3.4 Coupled Resonators

The central experimental setup of this work (see subsection 3.5.1) consists of coupled dielectric resonators. Hence, the concept of coupling is discussed in this section. Two models are considered: The coupling of three lossless dielectric resonators and the coupling of two lossy dielectric resonators. Each model is appropriate to describe a particular part of the setup. The model of coupled lossy resonators focuses on the determination and maximization of the amplitudes in the resonators, which is required for experimental evaluation and optimal experimental conditions.

3.4.1 Resonance Splitting of Coupled Resonators

The central setup in this work consists of three coupled dielectric resonators. This section discusses the effect of the coupling on resonance splitting. For simplification, loss is neglected and the resonance frequencies of the single resonators are assumed equal to each other. The coupled equations of motion for three resonators with respective amplitudes $I(t)$, $J(t)$ and $K(t)$ with resonance frequency ω_0 and a dimensionless coupling[3] c between next neighbors read:

$$\begin{aligned} \ddot{I}(t) + \omega_0^2 I(t) - c\omega_0^2 J(t) &= 0 \\ \ddot{J}(t) + \omega_0^2 J(t) - c\omega_0^2 I(t) - c\omega_0^2 K(t) &= 0 \\ \ddot{K}(t) + \omega_0^2 K(t) - c\omega_0^2 J(t) &= 0 \end{aligned} \tag{3.4.1}$$

[3]The coupling c is not to be confused with κ introduced in subsection 3.2.4. Both are dimensionless but $\kappa \approx 1$ and $c \ll 1$.

Taking $I(t) = I\ e^{i\omega t}$, $J(t) = J\ e^{i\omega t}$, and $K(t) = K\ e^{i\omega t}$ as an ansatz and writing the equations as a matrix yields:

$$\begin{pmatrix} \omega_0^2 - \omega^2 & -c\omega_0^2 & 0 \\ -c\omega_0^2 & \omega_0^2 - \omega^2 & -c\omega_0^2 \\ 0 & -c\omega_0^2 & \omega_0^2 - \omega^2 \end{pmatrix} \begin{pmatrix} I \\ J \\ K \end{pmatrix} = \mathbf{0} \tag{3.4.2}$$

The eigenvalues for ω^2 are the resonance frequencies of the coupled system:

$$\begin{aligned} \omega_1 &= \omega_0\sqrt{1-\sqrt{2}c} \approx \omega_0(1 - c/\sqrt{2}) \\ \omega_2 &= \omega_0 \\ \omega_3 &= \omega_0\sqrt{1+\sqrt{2}c} \approx \omega_0(1 + c/\sqrt{2}) \end{aligned} \tag{3.4.3}$$

For couplings $c \ll 1$, the three resonances are equally distanced ($\Delta\omega = \omega_3 - \omega_2 = \omega_2 - \omega_1$) and thereby follow the intermodulation relation $\omega_3 = \omega_{\mathrm{IM3+}} = 2\omega_2 - \omega_1$ (see section 2.3). The coupling coefficient c can then be directly related to the frequency splitting $c = \sqrt{2}\Delta\omega/\omega_0$. The corresponding eigenvectors $\mathbf{v} = (I, J, K)$ read:

$$\begin{aligned} \mathbf{v}_1 &= (1, \sqrt{2}, 1) \\ \mathbf{v}_2 &= (1, 0, -1) \\ \mathbf{v}_3 &= (1, -\sqrt{2}, 1) \end{aligned} \tag{3.4.4}$$

Equivalently, the coupling of two equal and lossless resonators return the resonance frequencies:

$$\begin{aligned} \omega_1 &= \omega_0\sqrt{1-c} \approx \omega_0(1 - c/2) \\ \omega_2 &= \omega_0\sqrt{1+c} \approx \omega_0(1 + c/2) \end{aligned} \tag{3.4.5}$$

The distance between the resonances of just two resonators is therefore $c = \Delta\omega/\omega_0$. The eigenvectors yield:

$$\begin{aligned} \mathbf{v}_1 &= (1, 1) \\ \mathbf{v}_2 &= (1, -1) \end{aligned} \tag{3.4.6}$$

$\mathbf{v}_1$ and $\mathbf{v}_2$ correspond to a symmetric and anti-symmetric mode, respectively.

Application

The core of the measurement setup (see subsection 3.5.1) consists of three coupled dielectric resonators. Figure 3.10 depicts the detection of the mode splitting in the transmission S_{31} and a variation of the coupling by changing the distance between the dielectric resonators. The experimental results are compared to finite element (FEM) electromagnetic field simulations that were performed with CST Microwave Studio. The simulated data returned slightly elevated resonances, 972 MHz for a single resonator versus 951 MHz observed in the experiment. The simulated data in Figure 3.10 was

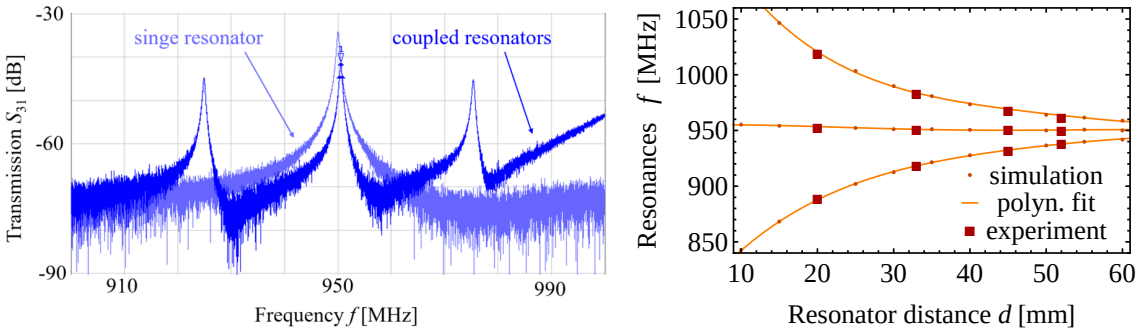

(a) Mode detection in transmission (b) distance dependency

Figure 3.10: Realization of resonance splitting. Left: Transmission S_{31} with visible resonances of a single resonator and three coupled resonators. Right: Resonance frequencies for different resonator distances and hence different couplings.

adjusted by that constant factor of 2 %. After this correction, the simulation and the experiment match, which is a good indicator for the control of the $TE_{01\delta}$-mode.
The model above assumed equal resonance frequencies and equal coupling and nearest neighbor coupling only. The most critical assumption turned out to be equal resonance frequencies [Ber18]. Unequal couplings do not influence the equal splitting relation, however unequal frequencies indeed lead to a violation of the equal splitting relation and hence to a violation of the intermodulation relation ($\omega_3 = 2\omega_2 - \omega_1$). The violation can partly be mitigated by arranging the resonators according to the their resonance frequency.

3.4.2 Coupling of Lossy Resonators

The model discussed in subsection 3.4.1 does not account for losses in the coupling. In theory, the tiniest coupling between two resonators at any distance would result in an equal amplitude in both resonators. However, this is not the case in a lossy system. This section has the aim to describe the relative amplitudes in weakly coupled resonators in a more appropriate way. Figure 3.11 depicts a lumped element circuit of two coupled resonators. One of them is excited inductively.
The coupling of the excited resonator I and the exciting loop A can be described by a lumped element circuit that is directly driven. The new circuit is depicted in Figure 3.12. The equivalence of the two circuits is shown with Equation A.0.7.
The new lumped element circuit has a modified resonance frequency and a modified

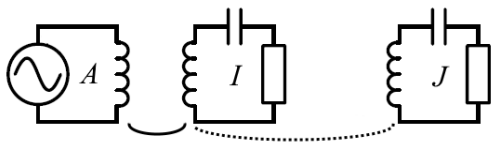

Figure 3.11: Lumped element circuit of two coupled dielectric resonators. Circuit I is inductively excited.

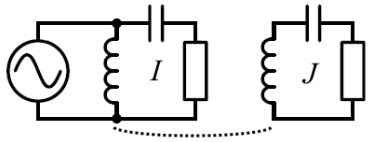

Figure 3.12: Modified Lumped element circuit of the model. It is equivalent to the circuit in Figure 3.11 and is taken as a basis for Equation 3.4.7.

loss. This model can now be used to investigate the influence of different couplings between the resonators. The corresponding set of differential equations looks like:

$$\begin{aligned} \ddot{I} + 2\gamma_\mathrm{I}\dot{I} + \omega_\mathrm{I}^2 I - c\omega_\mathrm{I}^2 J &= A\ e^{i\omega t} \\ \ddot{J} + 2\gamma_\mathrm{J}\dot{J} + \omega_\mathrm{J}^2 J - c\omega_\mathrm{J}^2 I &= 0 \end{aligned} \tag{3.4.7}$$

with periodic driving $A\ e^{i\omega t}$. I, J, and A are complex numbers corresponding to an amplitude with phase that allows a phase shift between the amplitudes. For $\gamma_\mathrm{I} = \gamma_\mathrm{J}$ and $\omega_\mathrm{I} = \omega_\mathrm{J}$ these equations decouple. Here, however, a more general solution is of interest. To solve this general case, the time dependence is separated:

$$\begin{aligned} \omega^2 I + 2i\omega\gamma_\mathrm{I} + \omega_\mathrm{I}^2(I - cJ) &= A \\ \omega^2 J + 2i\omega\gamma_\mathrm{J} + \omega_\mathrm{J}^2(J - cI) &= 0 \end{aligned} \tag{3.4.8}$$

Solving the latter equation leads to the relation between the amplitudes in the circuits I and J:

$$J = \frac{\omega_\mathrm{J}^2 c}{\omega_\mathrm{J}^2 - \omega^2 + 2i\omega\gamma_\mathrm{J}} I \tag{3.4.9}$$

Hence, the ratio of the amplitudes J and I does not depend on the properties of the circuit I. Instead, it depends on the damping γ_J, the frequency matching $\omega_\mathrm{J}^2 - \omega^2$ and the coupling factor c. The phase between I and J is not of interest and the relation for the amplitudes is:

$$|J| = \frac{c}{\sqrt{\left(\frac{\omega^2}{\omega_\mathrm{J}^2} - 1\right)^2 + \left(\frac{\omega}{\omega_\mathrm{J}}\frac{1}{Q}\right)^2}}\ |I| \tag{3.4.10}$$

Here, the relation between the damping and the quality factor $\gamma_\mathrm{J} = \omega_\mathrm{J}/(2Q_\mathrm{J})$ was used. Eventually, by inserting Equation 3.4.9 into the former equation of Equation 3.4.8, I can be calculated:

$$I = \frac{1}{\omega_\mathrm{I}^2 - \omega^2 + 2i\omega\gamma_\mathrm{I} - \frac{\omega_\mathrm{I}\omega_\mathrm{J}^2 c^2}{\omega_\mathrm{J}^2 - \omega^2 + 2i\omega\gamma_\mathrm{J}}} A \tag{3.4.11}$$

There are five frequencies that need to be distinguished: The resonance frequency of the inductively excited circuit I, ω_I, the resonance frequency of the second resonator ω_J, the new eigenfrequencies of the two modes that appear due to the coupling, ω_1 and

ω_2, and finally the frequency that the system is actually excited with, ω_e.
From now on, only the case of equal resonances $\omega_0 \coloneqq \omega_\mathrm{I} = \omega_\mathrm{J} = \omega_e$ is of interest: First, ω_I can be accurately adjusted to the frequency ω_J by changing the coupling to the input inductance. Then, ω_e can be accurately adjusted to $(\omega_2 + \omega_1)/2$. For low couplings c, the new eigenfrequencies are simply given by $\omega_{2,1} = (1 \pm c/2)\omega_0$. Under these circumstances, Equation 3.4.10 simplifies to:

$$|J| = c\, Q_\mathrm{J}\, |I| \tag{3.4.12}$$

With this equation, a known Q_J and coupling c, which can be determined by the frequency splitting, the amplitude ratio J/I can be determined. It is important to note that the amplitude distribution between two coupled resonators does not change if the two resonators have different losses. It solely depends on the coupling c and Q_J. It is handy to term the coupling c of equal amplitudes:

$$c_\mathrm{I=J} = \frac{1}{Q_\mathrm{J}} \tag{3.4.13}$$

Besides the bare knowledge of the amplitudes in the resonators, the amplitude J is to be maximized. Equation 3.4.11 simplifies with $\omega_0 \coloneqq \omega_\mathrm{I} = \omega_\mathrm{J} = \omega_e$ in the following way:

$$|I| = \frac{|A|}{\omega_0^2}\, \frac{1}{Q_\mathrm{J}}\, \frac{1}{c^2 + 1/(Q_\mathrm{I}Q_\mathrm{J})} \tag{3.4.14}$$

Plugging this into Equation 3.4.12 leads to:

$$|J| = \frac{|A|}{\omega_0^2}\, \frac{c}{c^2 + 1/(Q_\mathrm{I}Q_\mathrm{J})} \tag{3.4.15}$$

Equation 3.4.14 and Equation 3.4.15 are the result of the relative amplitudes in coupled resonators with loss. They are visualized in Figure 3.13: No energy is forwarded to resonator J at low couplings, corresponding to large distances. For strong couplings ($c \gg 1/Q_J$), the amplitudes at ω_1 and ω_2 approach another and the loss can be neglected, as done in subsection 3.4.1. The maximum of $|J|$ in terms of the coupling c is given at:

$$c_{\,\mathrm{J}\to\mathrm{max}} = \frac{1}{\sqrt{Q_\mathrm{I}Q_\mathrm{J}}} \tag{3.4.16}$$

Comparing this to $c_\mathrm{I=J}$ in Equation 3.4.13, the two special couplings are equal, $c_{\,\mathrm{J}\to\mathrm{max}} = c_\mathrm{I=J}$ for $Q_\mathrm{I} = Q_\mathrm{J}$.
For $Q_\mathrm{I} = Q_\mathrm{J}$, the maximum of the amplitude $|J|$ in the resonator mode coincides with the amplitude $|I|$. In fact, the loading of the excited resonator reduces its quality factor $Q_\mathrm{I} < Q_\mathrm{J}$. This results in a slightly stronger coupling to maximize $|J|$ (see Equation 3.4.16).

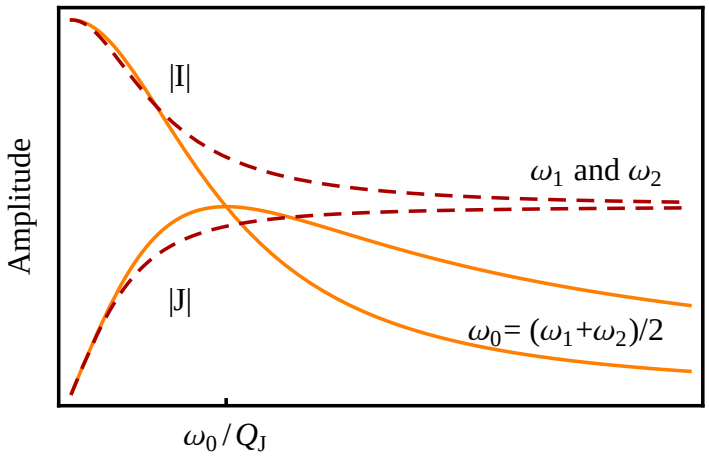

Figure 3.13: The amplitude of the driven resonator $|I|$ and the resonator $|J|$ for different couplings, represented by the splitting between the symmetric and the antisymmetric mode $\Delta\omega = c\omega_0$. Smaller couplings correspond to larger distances. Hence, large distances are found on the left hand side of the plot. The solid lines correspond to the amplitude at the center frequency $\omega_0 = (\omega_1 + \omega_2)/2$ while the dashed lines amplitudes are at amplitudes at ω_1 and ω_2.

Application

The determination of the nonlinear susceptibility requires the knowledge and preferably the optimization of the electric field amplitude in the dielectric resonators (see subsection 3.5.4). The amplitude distribution cannot be probed directly; however, the coupling $c_{\mathrm{I=J}}$ is visible in the reflection parameter S_{11} and therefore accessible.

Equation 3.2.23 introduced the impedance of a single mode in series circuit representation. Therefore, the impedance of two modes is just given by the sum of the impedances:

$$Z(\omega) = \frac{1}{1 + iQ\left(\frac{\omega}{\omega_1} - \frac{\omega_1}{\omega}\right)} R_p + \frac{1}{1 + iQ\left(\frac{\omega}{\omega_2} - \frac{\omega_2}{\omega}\right)} R_p \tag{3.4.17}$$

The resulting reflection S_{11} of Equation 3.4.17 using Equation 3.2.24 is sketched in Figure 3.14. Strong couplings lead to separated resonances. Weak couplings result in a single peak. The coupling $c_{\mathrm{I=J}}$ has the least reflection.

To maximize the electric field amplitude, the coupling needs to be arranged to $c_{\mathrm{J\to max}}$. However, this coupling cannot be qualitatively determined experimentally. Moreover, the gain associated with the optimization $c_{\mathrm{J\to max}}$ is comparatively small to the coupling $c_{\mathrm{I=J}}$. Hence, the coupling $c_{\mathrm{I=J}}$ is sufficient for optimization.

Still, $c_{\mathrm{I=J}}$ coupling is also hard to achieve experimentally, as some reflection always remains and the reflection does not drop to zero (see Figure 3.15). Hence, $c_{\mathrm{I=J}}$ coupling cannot be qualitatively distinguished from lower coupling, as both result in just a single peak. Instead, the coupling is chosen slightly above $c_{\mathrm{I=J}}$ so that the peaks are just distinguishable.

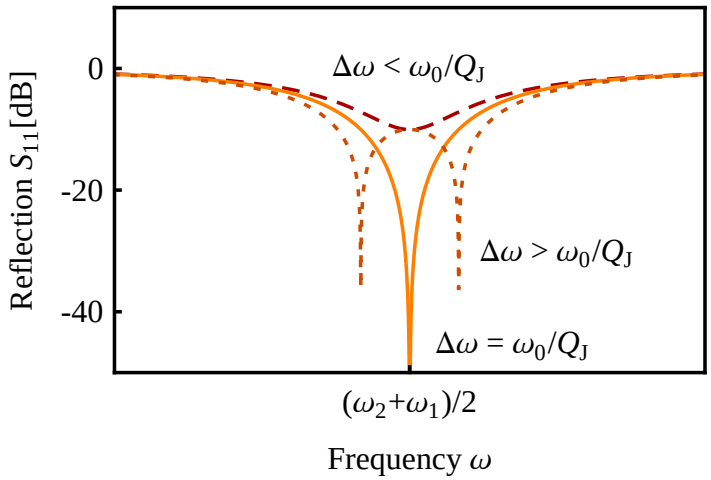

Figure 3.14: Theoretical reflection parameter S_{11} for couplings $c < 1/Q_J$, $c = 1/Q_J$ and $c > 1/Q_J$.

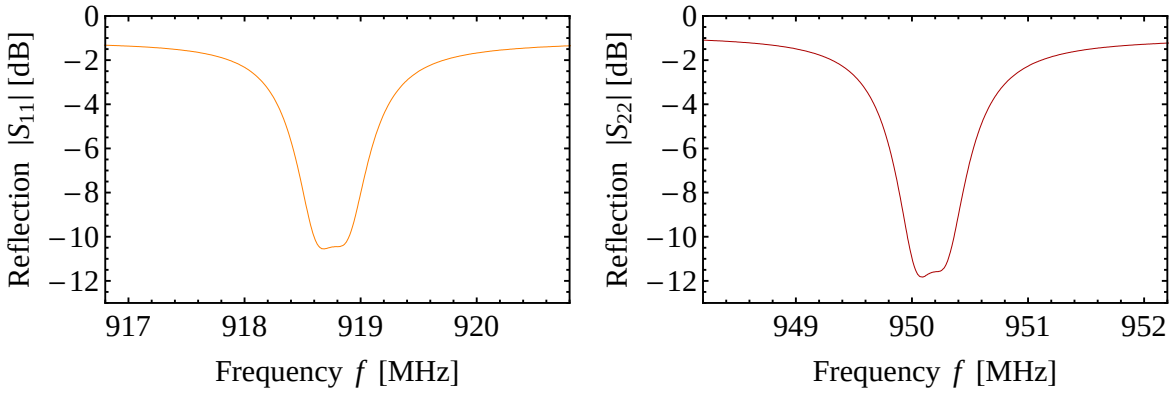

(a) Input f_1 (b) Input f_2

Figure 3.15: Experimental reflection S-parameters, adjusted to a coupling slightly above $c_{I=J}$ coupling. The two peaks are barely distinguishable.

3.5 Coupled Dielectric Resonator Method

3.5.1 Setup Principle

The challenge of measuring dielectric nonlinearities lies in the separation from other nonlinearities. A corresponding setup solving that challenge was designed by the authors of [NIH88]. The principle mainly relies on a favorable property of intermodulation generation in comparison to harmonic generation: Intermodulation only takes place in the presence of two tones. By designing a setup that restricts the two tones to a designated part of the setup, any measured intermodulation signal can be attributed to this part. A sketch of the setup is given in Figure 3.16.

Three cylindrical dielectric resonators made of the material under test (MuT) and of the same resonance frequency f_0 are lined up in a cutoff waveguide. The cutoff waveguide ensures that the energy transfer between the resonators happens only by coupling of the resonators and no traveling waves exist in the system. Assuming sufficiently weak

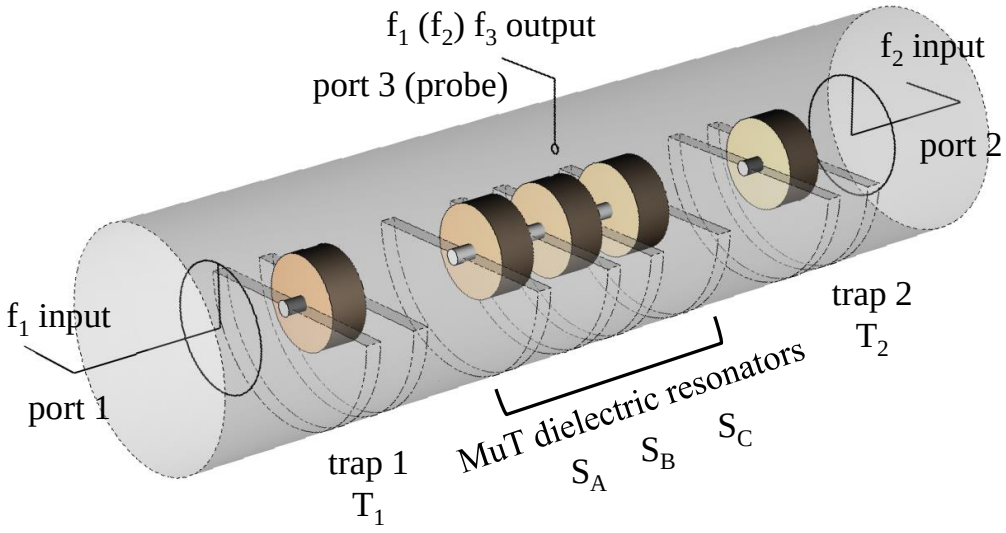

Figure 3.16: Sketch of the coupled dielectric resonator (CDR) setup. The core consists of three coupled resonators made from the material under test (MuT). This system is flanked by a filter resonator ("trap") on each side. The two tones are separately fed via the loops at both ends of the cavity. The intermodulation signal is probed above the resonator at the very center.

coupling between next neighbors, the system has three eigenfrequencies f_1, f_2, and f_3 following the relation $f_3 = 2f_2 - f_1$ (see subsection 3.4.1). These equally spaced frequencies correspond to the upper third order intermodulation product at frequency $f_3 = f_{\mathrm{IM3+}}$, generated by the tones f_1 and f_2 (or tones f_2 and f_3 with the lower third order intermodulation frequency $f_1 = f_{\mathrm{IM3-}}$). As the "coupled dielectric resonators" are the core of the setup, it will be referred to as the CDR setup. Based on the eigenvectors in Equation 3.4.4, the three modes are visualized in their theoretical and their experimental realization in Figure 3.17.

The resonant structure enables high sensitivity measurements by two manners: First, the field amplitudes of frequencies f_1 and f_2 are enhanced by the quality factor of the

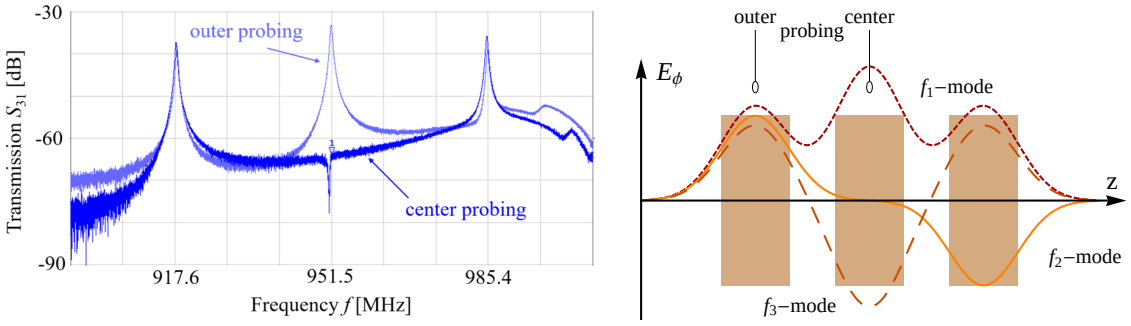

(a) Detection of the three central modes in S_{31} (b) Sketch of the three central modes

Figure 3.17: Comparison of the three central modes in experiment (left) and in theory (right). The signal of the f_2-mode is suppressed above the center resonator.

resonance. Second, the intermodulation signal is also enhanced by the quality factor of the resonance.

While classic PIM setups use two tone excitation from one common port (e.g. [KSB+20, WKSA18]), this setup feeds the tones from different inputs. To prevent leakage of the signal from the opposed input and thereby intermodulation generation in the inputs, the three MuT dielectric resonators are flanked by an additional dielectric resonator at each input. These "trap" resonators are tuned to the frequencies of their corresponding input and block the frequency from the opposed input.

Overall, the setup consists of five dielectric resonators, three of which are coupled with distinctive frequency splitting. The trap resonators are weakly coupled to the three MuT resonators without significant splitting. Hence, the resonances of the traps f_{T1} and f_{T2} coincide with the resonance frequency f_1 and f_2, respectively. The five resulting modes are sketched in Figure 3.18.

The intermodulation frequency f_3 is blocked by both trap resonators. Instead, the

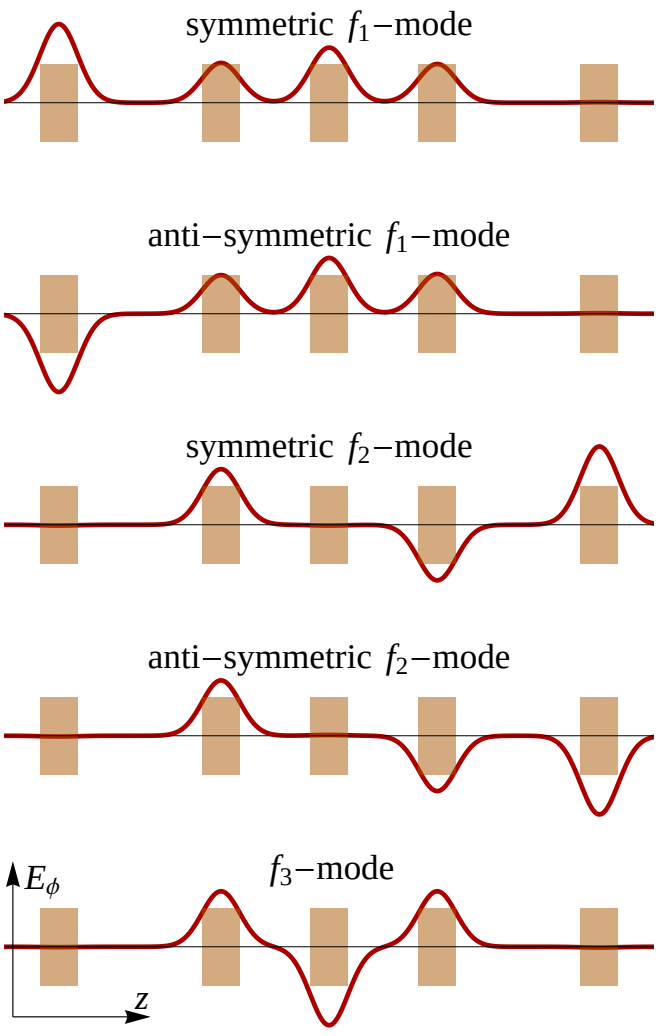

Figure 3.18: Sketch of five modes by five coupled dielectric resonators, ordered by their frequency (low to high).

intermodulation signal is probed above the center MuT resonator. Above this resonator, the amplitude of the second base frequency is suppressed due to the node of the second mode at the center resonator. This ensures that no intermodulation occurs in the output system (see Figure 3.17a). The f_1 and the f_3-mode have equivalent energy distributions and their amplitude above the center resonator can directly be compared. subsection 3.5.3 deals with the extraction of the material nonlinear susceptibility from the measurands.

3.5.2 Extension to Split Dielectric Resonators

The very general requirement for materials to be tested in the CDR setup is their suitability for dielectric resonators. Mostly, these requirements are a high permittivity and low dielectric loss. However, materials that are suitable for single dielectric resonators are not necessarily suitable for the CDR setup. This is mostly due to the $\mathrm{HEM}_{11\delta}$-mode resonance frequency approaching the $\mathrm{TE}_{01\delta}$-mode resonance frequency for the same geometry as the permittivity of the material goes down. This is further discussed later in this section when covering the limit of the "coupled split dielectric resonator method" (CsDR): that is to say, it is nevertheless possible to combine certain materials in a CsDR setup. This method relies on the properties of very suitable materials and the fact that the nonlinear response goes with the electric field to the power of three [3]: the MuT, which is unsuitable for the CDR method, is introduced as a slice between two discs of a material that is suitable for the CDR setup (see Figure 3.26b). Thereby, it uses the linear properties of the resonator material while probing the nonlinear properties of the MuT disc. The quantitative description can be found in subsection 3.5.3. With the knowledge of the nonlinearity of the resonator material, the MuT disc nonlinearity can be determined. The $\mathrm{TE}_{01\delta}$-mode is especially suited for this method, as the electric field is parallel to the surface and the electric field amplitude is not reduced in the MuT with lower ε_r.

Still, it is unavoidable to lower the average permittivity of the dielectric resonator and hence lowering the frequency of the $\mathrm{HEM}_{11\delta}$-mode. In addition, the $\mathrm{HEM}_{11\delta}$-mode has a larger energy ratio outside of the resonator than the $\mathrm{TE}_{01\delta}$-mode. This leads to a stronger coupling and hence a larger splitting of the modes, which drives the lowest $\mathrm{HEM}_{11\delta}$-mode to even lower frequencies. The simulation results in Figure 3.19a visualize this behavior. Three dielectric resonators with a MuT slice of 14 mm of $\varepsilon_r = 5$ between discs of 14 mm thickness of a $\varepsilon_r = 33$ material are coupled at different separations. In contrast to the $\mathrm{TE}_{01\delta}$-mode, the $\mathrm{HEM}_{11\delta}$-mode does not split symmetrically. Furthermore, the splitting already starts at much larger distances. As the $\mathrm{HEM}_{11\delta}$-modes lead to larger transmissions, they dominate the $\mathrm{TE}_{01\delta}$-modes, which hinders the proper functioning of the setup. The $\mathrm{HEM}_{11\delta}$-mode can be tamed by keeping a larger distance to the cutoff with larger dielectric resonators. This is shown in Figure 3.19b. In this way, the $\mathrm{TE}_{01\delta}$-modes can be nicely separated from the influence of the disturbing $\mathrm{HEM}_{11\delta}$-modes. However, the lower average ε_r does not only change the behavior of the $\mathrm{HEM}_{11\delta}$-modes,

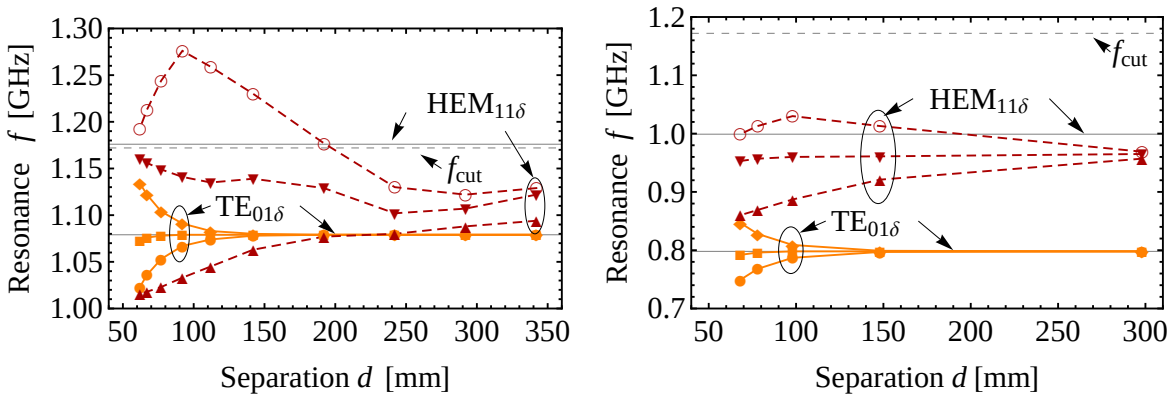

(a) Close cutoff splitting (b) Far cutoff splitting

Figure 3.19: Simulated $TE_{01\delta}$-modes and $HEM_{11\delta}$-modes of three coupled dielectric resonators. Solid horizontal lines: Respective $TE_{01\delta}$-mode and $HEM_{11\delta}$-mode of a single dielectric resonator. Dashed horizontal line: waveguide cutoff frequency f_{cut}. At low distances, the highest resonance originates from an even higher mode and not from the $HEM_{11\delta}$-mode. Lowering the resonance frequency of the dielectric resonator enables the separation of the $HEM_{11\delta}$-modes and the $TE_{01\delta}$-modes.

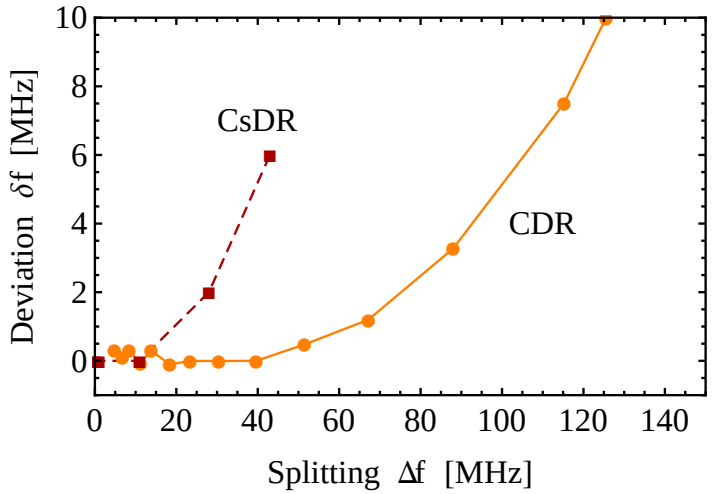

Figure 3.20: Simulated splitting in the CDR setup (solid) and the CsDR setup (dashed) for the $TE_{01\delta}$-mode. $\Delta f = f_2 - f_1$, $\delta f = \frac{1}{2}(f_1 + f_3) - f_2$. Symmetric splitting corresponds to $\delta f = 0$. For very low coupling (corresponding to large distances), the simulation returns unstable results. However, it is clear that the asymmetric splitting in the CsDR setup starts at smaller splitting than in the CDR setup.

but also of the $TE_{01\delta}$-modes: the $TE_{01\delta}$-modes do not split sufficiently symmetric anymore. Figure 3.20 plots the violation of symmetric splitting as a function of the frequency splitting. For the split dielectric resonators, the symmetry is violated at much smaller splitting than for non-split dielectric resonators. This violation was also observed experimentally for a $\varepsilon_r = 5$ glass. However, the symmetric splitting is a prerequisite for the setup to work. Still, the CsDR method extends the measurable range towards lower $\varepsilon_r > 15$ than the CDR setup.

3.5.3 Resonator Nonlinearity

This section aims at obtaining the nonlinear susceptibility χ_3 from the electric field amplitude $\hat{E}_2$ and the intermodulation power ratio at the output $\mathrm{IM_{3M}} = P_{3,out}/P_{1,out}$ for both the CDR and the CsDR method. It is different to the calculation proposed in [NIH88] and [1], as they base their calculation on the electric displacement field $D(E)$. It turned out that an approach based on the polarization $P(E)$ and thereby the dipole $p(E)$ gives more general results, especially for compensating nonlinearities. To obtain χ_3, it is assumed that the polarization has the form:

$$P(E)/\varepsilon_0 = \chi_1 E + \chi_3 E^3 \tag{3.5.1}$$

The applied electric field consists of two frequencies:

$$E(t) = E_1 \sin(\omega_1 t) + E_2 \sin(\omega_2 t) \tag{3.5.2}$$

Inserting the electric field into the polarization yields:

$$P(E_1, E_2, t)/\varepsilon_0 = ... + \frac{3}{4}\chi_3 E_1 E_2^2 \sin(\omega_{\mathrm{IM3+}} t) + ... \tag{3.5.3}$$

Here, only the frequency component of interest, the upper third order intermodulation, is considered explicitly. The local formulation at this frequency reads:

$$P_3(E_1, E_2, x) = \frac{3}{4}\varepsilon_0 \chi_3(x) E_1(x) E_2(x)^2 \tag{3.5.4}$$

In the $\mathrm{TE}_{01\delta}$-mode all fields $E_1(x)$, $E_2(x)$ and $P_3(x)$ have a component in $\hat{e}_\phi$ only. It is therefore convenient to introduce an electric dipole p_ϕ in $\hat{e}_\phi$ direction as a dipole moment amplitude for the resonator:

$$p_\phi = \int \mathbf{P}(\mathbf{x}) \cdot \hat{e}_\phi \, \mathrm{d}V \tag{3.5.5}$$

The dipole component at $\omega_{\mathrm{IM3+}}$ drives the f_3-mode:

$$p_{3,drv}(E_1, E_2, t) = \frac{3}{4}\varepsilon_0 \int \chi_3(x) E_1(x) E_2(x)^2 \mathrm{d}V \;\; \sin(\omega_{\mathrm{IM3+}} t) \tag{3.5.6}$$

The amplitude $\hat{p}_{3,drv}(\hat{E}_1, \hat{E}_2)$ can be written in terms of the normalized field distributions $E_i(x) = \hat{E}_i \varphi(x)$:

$$\begin{aligned} \hat{p}_{3,drv}(\hat{E}_1, \hat{E}_2) &= \frac{3}{4}\varepsilon_0 \hat{E}_1 \hat{E}_2^2 \int \chi_3(x) \varphi(x)^3 \, \mathrm{d}V \\ &= \frac{3}{4}\varepsilon_0 \hat{E}_1 \hat{E}_2^2 (\chi_{3\mathrm{A}} \varphi_{3\mathrm{A}} + \chi_{3\mathrm{R}} \varphi_{3\mathrm{R}} + \chi_{3\mathrm{D}} \varphi_{3\mathrm{D}}) \end{aligned} \tag{3.5.7}$$

Here, the field distribution factors φ_i and φ_{3i} are defined as:

$$\begin{aligned} \varphi_i &= \int_i \varphi(x)\ \mathrm{d}V \\ \varphi_{3i} &= \int_i \varphi(x)^3\ \mathrm{d}V \end{aligned} \tag{3.5.8}$$

The subscripts i represent a volume with constant dielectric properties, the surrounding air (A), the dielectric resonator material (R) and the disc material (D). In the CDR setup, no disc material is included and the MuT is the resonator material (R). For the CsDR setup, the disc material (D) is the MuT. $\hat{p}_{3,drv}(\hat{E}_1, \hat{E}_2)$ is the driving dipole moment of one resonator. The resulting $\hat{p}_{res}$ is enhanced by the resonance:

$$\hat{p}_{3,res}(\hat{E}_1, \hat{E}_2) = Q\ \hat{p}_{3,drv}(\hat{E}_1, \hat{E}_2) \tag{3.5.9}$$

This dipole $\hat{p}_{3,drv}(\hat{E}_1, \hat{E}_2)$ can be rewritten as the electric field amplitude $\hat{E}_3$ at the center resonator:

$$\begin{aligned} \hat{p}_{3,res}(\hat{E}_3) &= \varepsilon_0 \int \chi_1(x) E_3(x)\ \mathrm{d}V \\ &= \varepsilon_0(\chi_\mathrm{A}\varphi_\mathrm{A} + \chi_\mathrm{R}\varphi_\mathrm{R} + \chi_\mathrm{D}\varphi_\mathrm{D})\hat{E}_3 \end{aligned} \tag{3.5.10}$$

Solving for $\hat{E}_3$ results in:

$$\hat{E}_3 = \frac{\hat{p}_{3,res}(E_3)}{\varepsilon_0(\chi_\mathrm{A}\varphi_\mathrm{A} + \chi_\mathrm{R}\varphi_\mathrm{R} + \chi_\mathrm{D}\varphi_\mathrm{D})} \tag{3.5.11}$$

Inserting Equation 3.5.7 returns:

$$\frac{\hat{E}_3}{\hat{E}_1} = \frac{3}{4}\varepsilon_0 Q \frac{(\chi_{3\mathrm{A}}\varphi_{3\mathrm{A}} + \chi_{3\mathrm{R}}\varphi_{3\mathrm{R}} + \chi_{3\mathrm{D}}\varphi_{3\mathrm{D}})}{\varepsilon_0(\chi_\mathrm{A}\varphi_\mathrm{A} + \chi_\mathrm{R}\varphi_\mathrm{R} + \chi_\mathrm{D}\varphi_\mathrm{D})} \hat{E}_2^2 \tag{3.5.12}$$

Using the definition $\mathrm{IM}_{3\mathrm{M}} = P_{3,out}/P_{1,out}$, which is the ratio of the two powers at f_1 and f_3 at the probe, and defining the resonator nonlinearity

$$\xi = \frac{\chi_{3\mathrm{A}}\varphi_{3\mathrm{A}} + \chi_{3\mathrm{R}}\varphi_{3\mathrm{R}} + \chi_{3\mathrm{D}}\varphi_{3\mathrm{D}}}{\chi_\mathrm{A}\varphi_\mathrm{A} + \chi_\mathrm{R}\varphi_\mathrm{R} + \chi_\mathrm{D}\varphi_\mathrm{D}} \tag{3.5.13}$$

leads to:

$$\mathrm{IM}_{3\mathrm{M}} = \left(\frac{\hat{E}_3}{\hat{E}_1}\right)^2 = \left(\frac{3}{4} Q\ \xi\ \hat{E}_2{}^2\right)^2 \tag{3.5.14}$$

Measuring $\mathrm{IM}_{3\mathrm{M}}$ gives two solutions for ξ, a positive and a negative. Nevertheless, the resonator nonlinearity ξ is assumed positive. Instead, the choice of sign is introduced for the material nonlinear susceptibility $\chi_{3\mathrm{R}}$:

$$\chi_{3\mathrm{R}} = \pm \frac{\varphi_\mathrm{R}}{\varphi_{3\mathrm{R}}} \chi_\mathrm{R}\ \xi \tag{3.5.15}$$

Here, the linear and the nonlinear susceptibility of the air are both set to zero. In

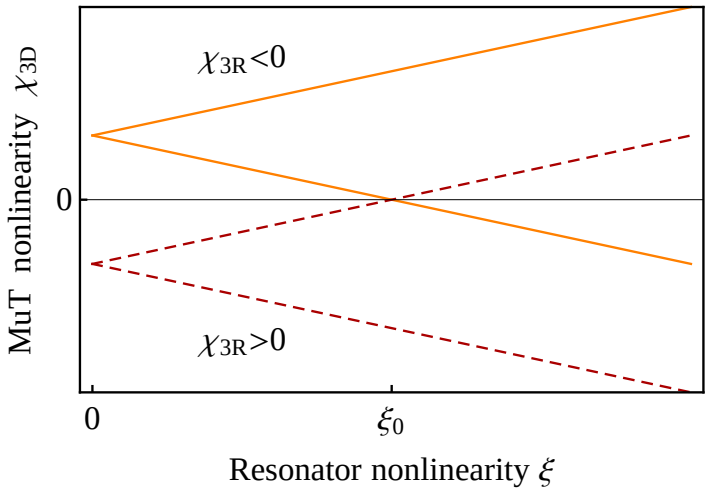

Figure 3.21: Sketch for deducing the MuT nonlinear susceptibility χ_{3D}. There are generally four possible values for χ_{3D} for one measured resonator nonlinearity ξ. $\xi < \xi_0$ induces opposite signs of χ_{3D} and χ_{3R}.

the CsDR setup, the determination of the MuT nonlinearity additionally requires the knowledge of the resonator material:

$$\chi_{3D} = \pm\frac{\chi_R\varphi_R + \chi_D\varphi_D}{\varphi_{3D}}\,\xi - \frac{\varphi_{3R}}{\varphi_{3D}}\chi_{3R} \tag{3.5.16}$$

Figure 3.21 sketches the possible realizations of χ_{3D} for certain resonator nonlinearities ξ. The reference resonator nonlinearity ξ_0 is defined by setting $\chi_{3D} = 0$.

$$\xi_0 = \frac{\chi_{3R}\varphi_{3R}}{\chi_R\varphi_R + \chi_D\varphi_D} \tag{3.5.17}$$

Now, the overall resonator nonlinearity ξ can be normalized to ξ_0. Shortening Equation 3.5.16 to $\chi_{3D} = \pm\zeta_1 - \zeta_2\chi_{3R}$ yields:

$$\frac{\xi}{\xi_0} = \frac{\zeta_1}{\zeta_2\chi_{3R}} \tag{3.5.18}$$

Besides some geometric corrections and the quality factor of the resonance, Equation 3.5.14 mainly requires the knowledge of the electric field amplitude $\hat{E}_2$ and the power ratio IM_{3M}. While the power ratio is obtained straight forward by comparing the output powers at f_1 and f_3, the calculation of $\hat{E}_2$ is more elaborate and will be discussed separately in subsection 3.5.4.

3.5.4 Electric Field Amplitude

As mentioned in subsection 3.5.3, the calculation of the nonlinear susceptibility requires the knowledge of the absolute electric field amplitude $\hat{E}_2$, the maximum in both space and time of the electric field in either of the outer resonators of the three MuT resonators. To obtain $\hat{E}_2$, the entire setup is modeled as a system of lumped element circuit. Each

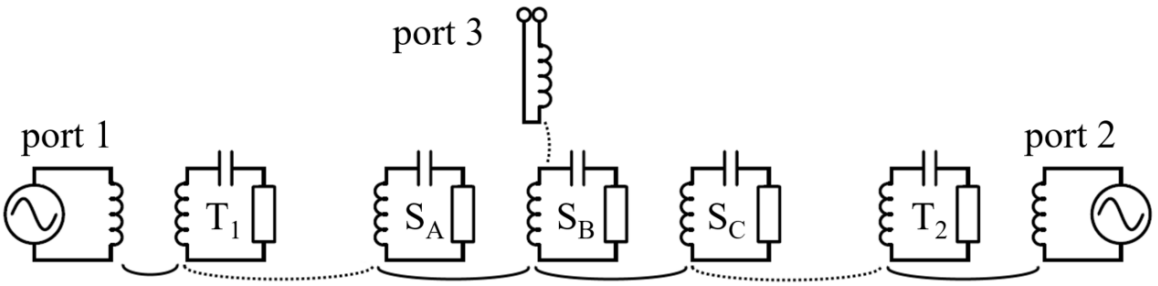

Figure 3.22: The setup represented by lumped element circuits. The three oscillating circuits correspond to the three MuT dielectric resonators (S_A, S_B, S_C) and the two outer circuits to the traps (T_1,T_2). There is an input from each side. The output probes the magnetic field above the center resonator. Each circuit is only assumed to couple inductively with its next neighbors. Strong and weak coupling is visualized by solid and dashed lines between the inductances, respectively.

resonator is represented by a lumped element resonance circuit. They are inductively coupled to their next neighbors. The entire system is depicted in Figure 3.22.

This general system can be divided in several subsystems. For each system, it is appropriate to make different assumptions. The coupling between the three MuT resonators is strong in the sense that the loss can be neglected ($c \gg 1/Q_0$) and the description presented in subsection 3.4.1 holds.

On the other hand, the coupling of the trap/MuT resonator system is weak ($c \approx 1/Q_0$) and loss needs to be taken into account. This is discussed in subsection 3.4.2. Nevertheless, the description can be simplified because all modes except for the symmetric and antisymmetric f_2-mode are far away and can be neglected. Hence, this mode can then be modeled by a single lumped element circuit, coupled to its corresponding trap resonator, as pictured in Figure 3.11. Finally, as long as a perturbation description of the resonator system is valid, the field distributions can be calculated for each dielectric resonator separately and can then be linearly superposed.

The coupled resonators are excited with $f_2 = (f_{2,sym} + f_{2,asy})/2$, where $f_{2,sym}$ and $f_{2,asy}$ are the frequencies of the symmetric and the anti-symmetric mode in Figure 3.18. This results in an excitation of the trap resonator and the f_2-mode of the MuT resonators being phase shifted by $\pi/2$. The energy in this mode is labeled $W_{\mathrm{M+T}}$. Using Equation 3.2.16 and then Equation 3.1.6 yields:

$$W_{\mathrm{M+T}}(P_{2,in}) = \frac{Q_{\mathrm{M+T}}}{\omega_2} P_{2,abs} = \frac{Q_{\mathrm{M+T}}}{\omega_2}(1 - |S_{22}|^2) P_{2,in} \tag{3.5.19}$$

The quality factor of the mode is reduced by coupling into the mode (the loading of the output can be neglected, in comparison the loading at the inputs). This is expressed by Equation 3.2.28:

$$W_{\mathrm{M+T}}(P_{2,in}) = \frac{Q_0}{\omega} \frac{1 + |S_{22}|}{2} (1 - |S_{22}|^2) P_{2,in} \tag{3.5.20}$$

Here, Q_0 is the unloaded quality factor of the mode, which corresponds to the quality factor of a single dielectric resonator if trap and resonator all have the same quality factor. Furthermore, it is assumed that the coupling to the T+M mode is subcritical. The measurements presented in Figure 3.8 confirm that model. For coupling $c_{\mathrm{I=J}}$ between the trap and the MuT resonators, the energy is just equally distributed between the two (see subsection 3.4.2). Hence, the MuT resonator mode stores half of the overall energy:

$$W_{\mathrm{M}} = \frac{1}{2} W_{\mathrm{M+T}} \tag{3.5.21}$$

Next, the energy in the f_2-mode is stored in the outer resonators of the three MuT resonators. The energy is equally distributed between the two, so the energy in one resonator is just half the energy stored in the f_2-mode:

$$W_{\mathrm{R}} = \frac{1}{2} W_{\mathrm{M}} \tag{3.5.22}$$

Finally, the field distribution of a single resonator needs to be considered. Using the conversion from Equation 3.2.14, the amplitude is given by:

$$\hat{E}_2 = c_{\mathrm{EW}} \sqrt{W_{\mathrm{R}}} \tag{3.5.23}$$

Overall, the electric field amplitude $\hat{E}_2$ results in:

$$\hat{E}_2 = c_{\mathrm{EW}} \sqrt{\frac{1}{4} \frac{Q_0}{\omega_2} \frac{1 + |S_{22}|}{2} (1 - |S_{22}|^2) P_{2,in}} \tag{3.5.24}$$

3.5.5 Setup Realization

Figure 3.23 shows an image of the cavity. It is manufactured from a copper pipe with an inner diameter of 15 cm (cutoff frequency at 1.172 GHz). The copper pipe has a length of 80 cm. The cavity closures with the input loops are shown in Figure 3.24. The loops are soldered to the center conductor of the flange. The other end is connected to the cavity closure, which is itself grounded to the outer conductor of the coaxial interface. Following the recommendation by [NIH88], the copper pipe itself is not connected to the cavity closure, though connecting them did not lead to a different behavior of the setup.

Figure 3.25 shows the realization of the probe system. A semi-rigid coaxial cable is inserted into the cavity though a hole in the cavity pipe. A loop is formed to be sensitive to the magnetic field. The loop is placed so that the normal vector of the area points along the cavity length, which is the direction of the magnetic field of the $\mathrm{TE}_{01\delta}$-mode (turning the probe by 90° significantly reduced the coupling, as expected). The fixture to hold the probe was designed to be adjustable to find a compromise between sufficient coupling for sensitivity and not disturbing the system. However, it turned out that the perturbation is negligible even if the probe is completely immersed in the cavity.

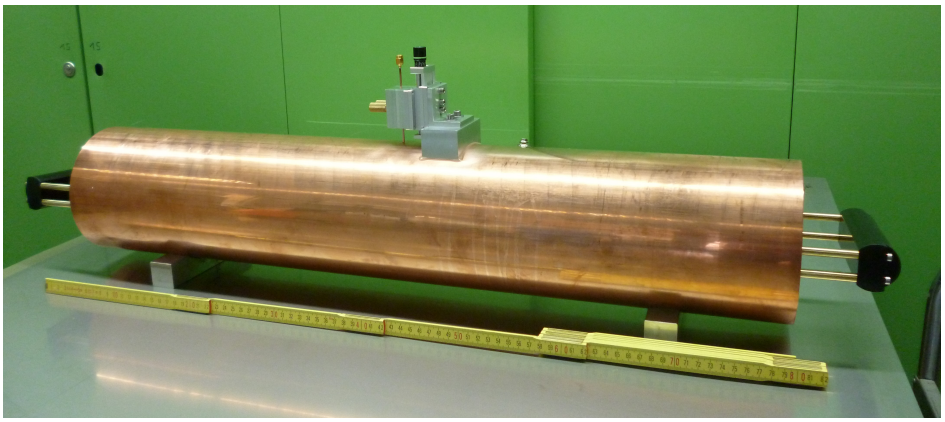

Figure 3.23: Picture of the cavity. The two tones are fed from both sides while the output signal is taken in the middle of the cavity's length.

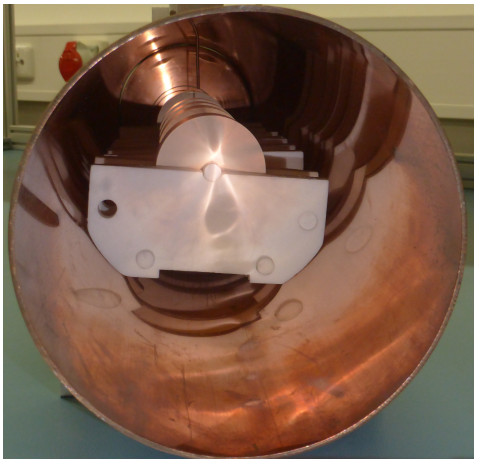

(a) View inside of the cavity, loaded with the five dielectric resonators.

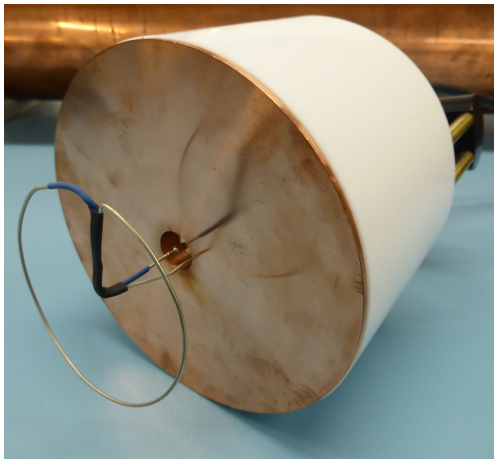

(b) Input, consisting of the input coupling loop and the cavity closure.

Figure 3.24: Open setup. The diameter of the cavity is 15 cm.

Figure 3.26 shows the central part of the setup, the three MuT dielectric resonators. They are all put in one vessel. The vessel is made of the aerofoam Rohacell 31 HF [Evo11], having negligible linear dielectric properties ($\varepsilon_r = 1.04$, $\tan\delta < 0.2 \times 10^{-3}$). The resonator discs are mounted on a rod of Rohacell. Further rods through the sheets result in sufficient rigidity to position the dielectric resonators and then inserting them into the cavity. For the CsDR setup, additional discs of the MuT are inserted between two resonator discs (see Figure 3.26b). This is also done for the very center resonator, though no nonlinear signal actually originates from this resonator. Still, this is the simplest way to achieve the same linear properties of all three resonators, which is necessary to fulfill the intermodulation relation. The traps are mounted on separate vessels so their distance to the MuT resonators can also be adjusted after insertion into the cavity. Figure 3.27 sketches the connections of the cavity.

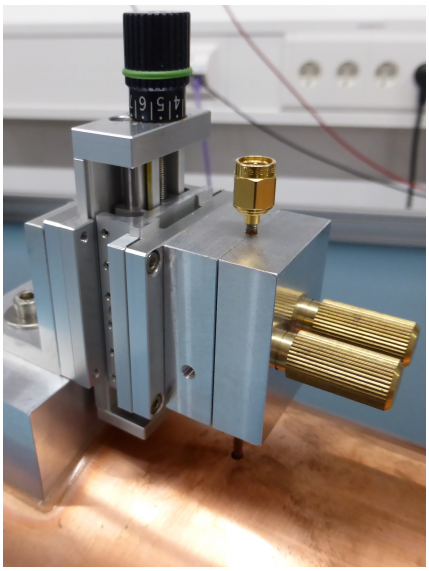

(a) Fixture

(b) Magnetic field probe

Figure 3.25: Output system. Left: Fixture for holding the probe. The screw enables to determine the penetration depth precisely. Right: close-up view of the probe consisting of a semi-rigid cable and a loop for coupling to the magnetic field and a SMA connector as interface to the spectrum analyzer.

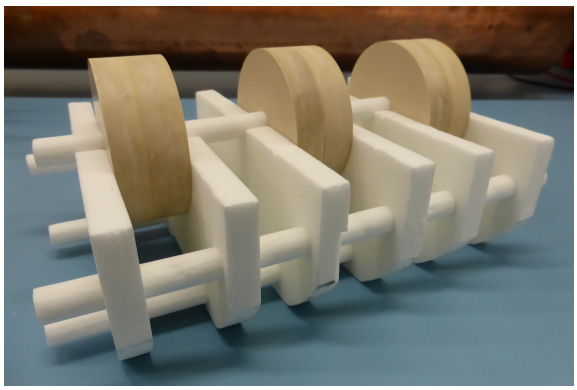

(a) CDR setup

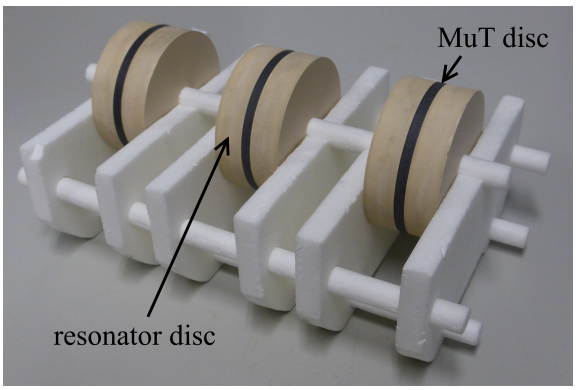

(b) CsDR setup

Figure 3.26: Dielectric resonators mounted on the support vessel. The diameter of the dielectric resonators is 6 cm.

3.5.6 Measurement Procedure

Determination of ε_r and $\tan\delta$

To set the dimensions for manufacturing the dielectric resonators of the MuT, the permittivity in the frequency range of interest ($\sim 1\,\mathrm{GHz}$) needs to be known. A characterization of the loss is not necessarily required but is helpful for comparison with the resonator loss. The dielectric characterization was performed with SPDR (see section 3.3).

Field simulation with CST Microwave Studio

With the known permittivity, a dielectric resonator with a resonance frequency close to 1 GHz can be designed. The aspect ratio is chosen such that the interfering HEM-mode is far enough from the splitting $TE_{01\delta}$-modes.

Preparation of the setup with the VNA

A Keysight ENA 20GHz was used for preparing the setup. 16,000 points are taken in one sweep with a bandwidth of 70 kHz as a compromise of noise level and sweep time for feasible feedback to manually adjust the setup. A simple reflection and transmission response calibration is sufficient, ranging from 850 MHz to 1050 MHz. The reference planes is at the end of the coaxial cables.

The MuT dielectric resonators (S_A, S_B and S_C) are placed on a Rohacell vessel (see Figure 3.26). The distance between the dielectric resonators is set to 33 mm with a ruler. This results in a splitting of about 30 MHz. The precise distance setting is not of relevance for the equal frequency spacing between the modes, a positioning of ± 1 mm is sufficient.

The vessel with the MuT dielectric resonators is placed in the center of the cavity with a ruler. The center resonator S_B can be placed within 5 mm beneath the output probe. The output probe is then moved radially towards the center MuT dielectric resonator to about 1 cm distance.

T_2 is placed about 10 cm away from the closest of the three MuT dielectric resonators, S_C. Then, input 2 is inserted while observing S_{22}. When moving the input closer to T_2, a dip for the trap and the f_2-mode appears. If the dip for f_2-mode is not visible, the coupling between T_2 and f_2-mode is too low and T_2 needs to be moved towards the resonator S_C. If the two dips do not merge into one when moving the input loop closer to T_2, the coupling is too strong and T_2 needs to be moved away from the resonators. This procedure is repeated until splitting of the resonances just becomes visible ($c_{I=J}$ coupling, see Figure 3.15). Empirically, this requires a precision of 1 mm in positioning T_2. It is advisable to rather go for a slightly over-coupled adjustment, because actual

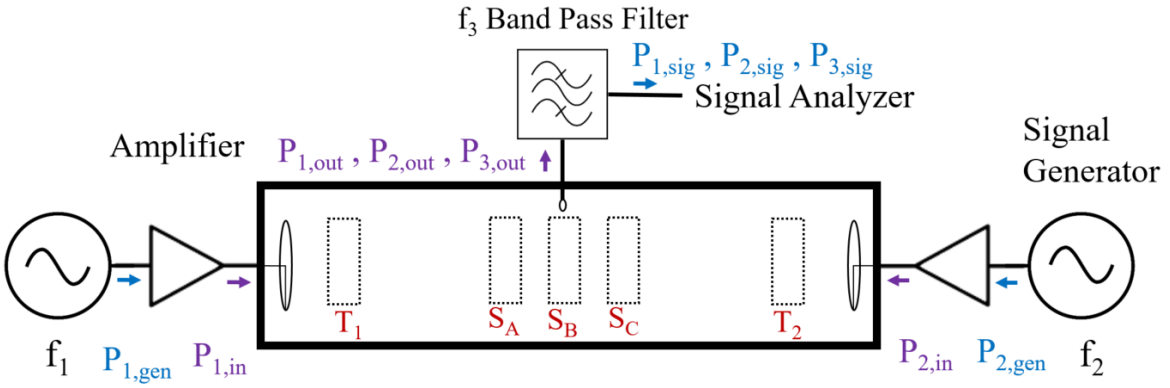

Figure 3.27: Sketch of the connected setup. Signal Generators: Keysight MXG 6GHz and Keysight PSG 40GHz, Signal Analyzer: Keysight MXA 26GHz.

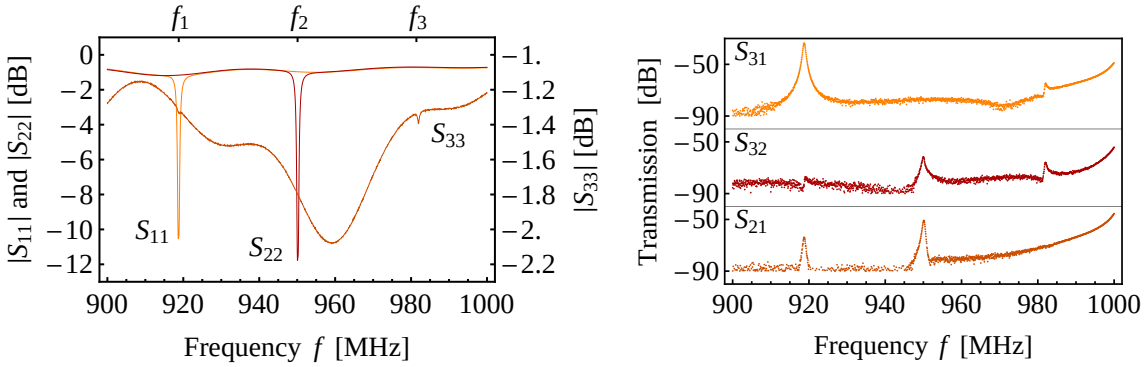

(a) Reflection S_{ii}-parameters (b) Transmission S_{ji}-parameters

Figure 3.28: Measured S-parameters of the CDR setup. Ports 1 and 2 are inputs and port 3 is the probe. Close-up views of the S_{11} and S_{22} peaks are plotted in Figure 3.15. The ports are isolated from each other by at least $-50\,\mathrm{dB}$, except for S_{31} at f_1.

$c_{\mathrm{I=J}}$ coupling cannot be distinguished from under-coupling. The frequency f_2 is recorded. The frequency of the f_3-mode is visible as a slight bump in S_{33}, as in Figure 3.28. Next, T_1 is introduced at the opposite side of the cavity. it is placed about 10 cm away from the closest of the three MuT dielectric resonators, $\mathrm{S_A}$. Input 1 is inserted while observing S_{11}. The same repetitive procedure as with input 2 is performed. When $c_{\mathrm{I=J}}$ coupling is achieved, the reference value of f_1, $f_1^{ref} = 2f_2 - f_3$ is compared to its actual value f_1^{act}. The deviation must not exceed f_0/Q_0 (about 1 MHz for $Q_0 \approx 1000$). If the frequencies do not match, this is most likely due to the dielectric resonators not

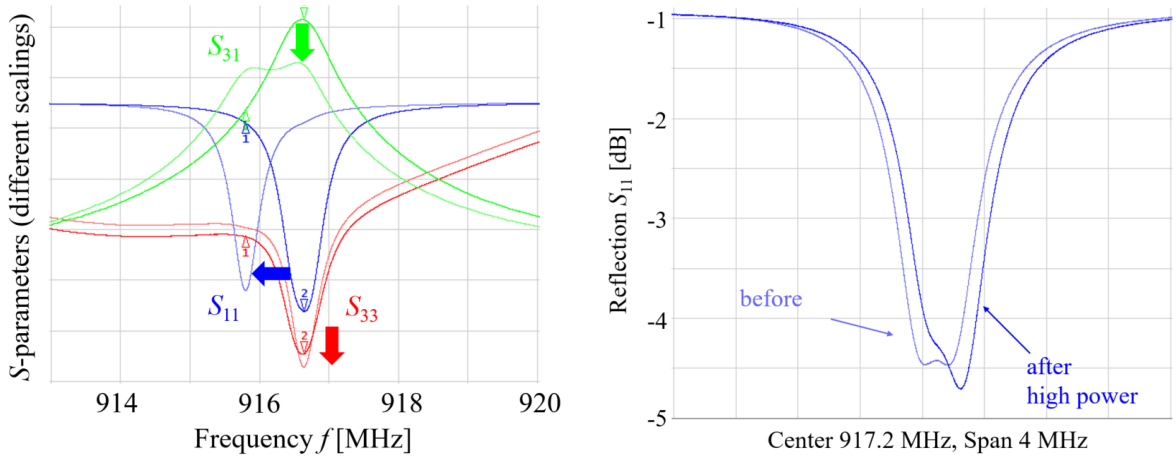

(a) Foreground: $c_{\mathrm{I=J}}$ coupling at f_1^{act}, Background: f_{T1} set to f_1^{ref}.

(b) Temperature shift: Before (background) and after (foreground) application of high power.

Figure 3.29: f_1-matching and temperature shift effect. The arrows in the left figure visualize the change from $f_{\mathrm{T1}} = f_1^{act}$ to $f_{\mathrm{T1}} = f_1^{ref}$: The minimum in S_{11} shifts about 1 MHz to lower frequencies. S_{33} keeps its minimum at f_1^{act} while f_1^{ref} and f_1^{act} become visible separately in the transmission S_{31}. The drop in S_{31} is accompanied by a drop in the electric field amplitude E_1 in the MuT resonators.

having sufficient similar resonance frequencies. The problem can be partly addressed by changing the order of the MuT dielectric resonators [Ber18].
Of course, perfect matching is unlikely. Input 1 is finally moved so that the reflection is minimal for f_1^{ref}. The frequency of the f_1 signal generator is set to $f_1 \coloneqq f_1^{ref}$. A mismatch in f_1 is easiest to tolerate in comparison to f_2 and f_3, as a mismatch in f_3 leads to a reduction of the smallest signal and the power at f_3 depends stronger on the power at f_2 than at f_1. Furthermore, the electric field amplitude E_2 needs to be known to deduce χ_3, so the relation of $P_{2,in}$ and E_2 needs to be known, which is easiest to model when $f_{\mathrm{T2}} = f_2$.
Now, the tunable filter is adjusted in such a way that the intermodulation frequency f_3 lies at the lower end of its pass band, i.e. the insertion loss at f_3 is 1 dB. This ensures optimal suppression of the input frequencies f_1 and f_2. As the VNA itself does not cover the dynamic range to measure the suppression at those frequencies (typically $-80\,\mathrm{dB}$ at f_2 and $-110\,\mathrm{dB}$ at f_1), the filter characterization at f_2 and f_1 is performed with the use of the amplifier together with the spectrum analyzer. As this system is not calibrated and includes cable losses, the insertion loss at f_3 measured with the amplifier and the spectrum analyzer is compared to the insertion loss measured with the calibrated VNA.

Recording of the intermodulation
The tunable filter is connected to the output probe and the amplifiers to the corresponding inputs. The high power should be applied for a short time (few seconds) only to avoid heating of the resonators. The signal analyzers power levels $P_{1,sig}$, $P_{2,sig}$ and $P_{3,sig}$ at respective frequencies f_1, f_2 and f_3 are recorded for different input power levels, together with the input power levels of the signal generators $P_{1,gen}$ and $P_{1,gen}$ at respective frequencies f_1 and f_2. To control for unexpected changes in the setup, two overlapping power sweeps are preformed (low power range and high power range). The powers should should be consistent. After exposing the dielectric resonators to the high power, the S-parameters are checked again with the VNA to exclude changes in the resonances due to heating (see Figure 3.29b).

3.6 Capacitance Bridge

3.6.1 Static Bias Nonlinear Response

A qualitative different technique to measure a nonlinear behavior consists of a static high amplitude signal and a superposed small amplitude probing signal, which is used to test the local slope. This is depicted in Figure 3.30. The static high amplitude signal gives rise to the nonlinear response. Nevertheless, the nonlinear response depends on the test frequency. Concerning dielectric nonlinear response, materials have been tested in the kHz range [KGV+14, BDB09] but also in the GHz range [KJH02, DSKJH96] with DC bias.

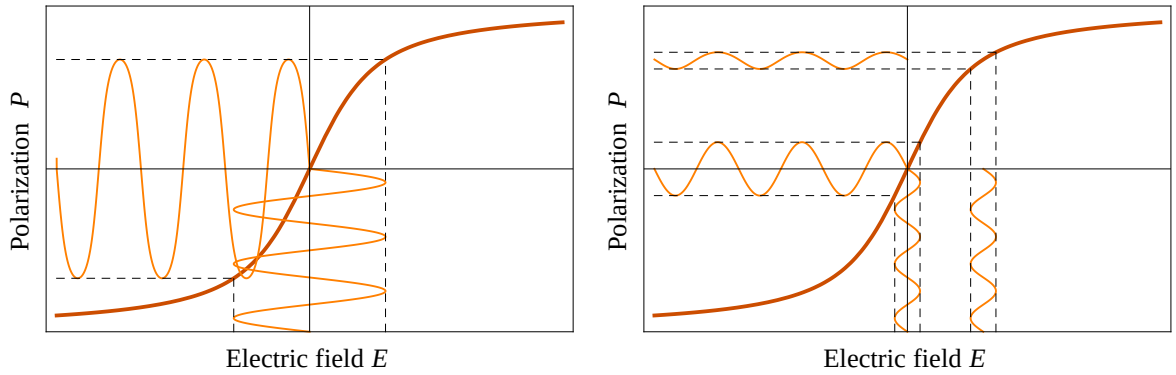

(a) Detection by signal distortion (b) Detection by slope test

Figure 3.30: Comparison of two qualitatively different methods to detect a nonlinear response. Similar representation can be found in e.g. [MDK11].

3.6.2 Voltage Dependent Capacitance

A nonlinear permittivity $\varepsilon_r(E)$ directly leads to a voltage dependent capacitance $C(V)$ of a capacitor made from the nonlinear dielectric. The capacitance of a thin ($A \gg d^2$) capacitor with area A and thickness d is given by

$$C = \varepsilon_0 \varepsilon_r \frac{A}{d} \tag{3.6.1}$$

For the thin capacitor geometry, the de-electrification factor turns out to be $N = 1$. Hence, the magnitude of the macroscopic electric field $\mathbf{E}_{mac}$ in the dielectric is

$$E_{mac} = \frac{E_{ext}}{\varepsilon_r} = \frac{V}{\varepsilon_r \, d} \tag{3.6.2}$$

Electrostriction leads to dependencies $A(E)$ and $d(E)$. However, as the sensitivity of the setup is too low to detect electrostrictive effects (discussed in subsection 2.4.6), it is neglected in this discussion. Hence, the change of the capacitance is fully explained by the change of the permittivity as follows:

$$\Delta\varepsilon_r = \frac{d}{A\varepsilon_0}\Delta C \tag{3.6.3}$$

The third order nonlinear susceptibility χ_3 can be derived from $\Delta\varepsilon_r$ via:

$$\chi_3 = \frac{\Delta\varepsilon_r}{E_{mac}^2} = \frac{d^3\varepsilon_r^2}{A\varepsilon_0 V^2}\Delta C \tag{3.6.4}$$

It becomes clear that the determination of χ_3 critically depends on the thickness d.

3.6.3 Bridge Circuit

Generally, a bridge circuit is a circuit with two parallel branches that are connected at some point in-between. The elements of the circuit are then modified in such a way that the voltage and current at this connection are zero. For the presented measurements, a AH2550A 1 kHz Ultra-Precision Capacitance Bridge by Andeen-Hagerling is used.
In the capacitance bridge, the two branches are a known impedance and the unknown impedance, the device under test (DuT) (see Figure 3.31). The known impedance consist of a parallel circuit of a temperature-stabilized fused-silica capacitor and a resistor. Potential dividers in form of ratio transformers allow adjusting the voltage over the known impedance and the unknown impedance in such a way that the detector measures no voltage. The detector measures both in-phase and $\pi/2$-shifted voltages relative to the generator signal. From the ratio at the potential dividers, the unknown complex impedance can be determined.
To measure the voltage dependent impedance, a DC bias voltage is fed into the LOW terminal via a series resistance. The bridge allows choosing between two internal resistances, 100 MΩ and 1 MΩ. A large resistance leads to a larger time constant and therefore reduced noise, but the charging time for the capacitor increases as well. In case of a DC conducting sample, a voltage divider is created additionally. In this case, the DC voltage at the DuT is smaller than the applied bias voltage. For a capacitance of around 100 pF and a resistance of 100 MΩ, the time constant $\tau = 10$ ms for charging is still small enough for the measurement procedure discussed in section 4.2. Additionally, the DuTs do not exhibit a DC conductance. Hence, the large series resistance can be

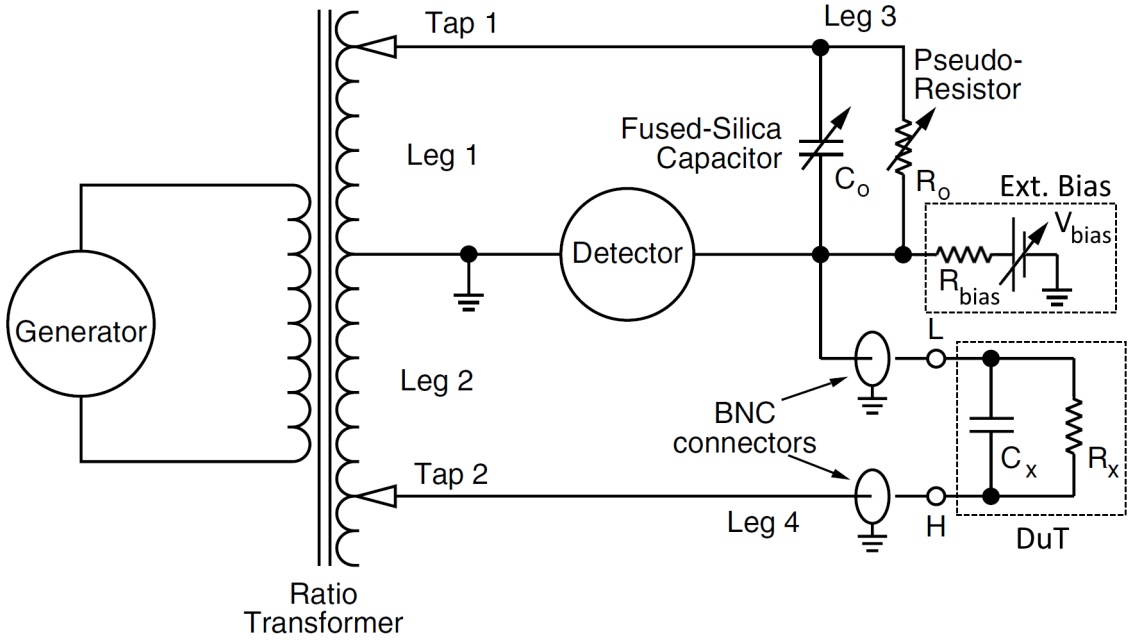

Figure 3.31: Bridge circuit sketch. The bridge circuit consists of two branches with a known impedance in one branch and with the DuT in the other. Figure taken from [AH02], modified.

chosen to obtain the best signal to noise ratio. For handling safety reasons, another external 100 kΩ is connected in series just after the voltage supply to limit the current to 1 mA. Without DC bias voltage, the bridge drives the voltage at the detector to zero. With a DC voltage, the voltage at the detector cannot be driven to zero anymore and the voltage is minimized instead.

The bridge circuit already enables to detect nonlinear susceptibilities $\chi_3 > 10^{-14}\,\mathrm{m^2/V^2}$. However, an even more sensitive method claims to be able to detect nonlinearities down to $\chi_3 > 10^{-16}\,\mathrm{m^2/V^2}$ by detecting the frequency shift of a resonance circuit with a capacitance of the MuT [FFK+93].

3.6.4 Equivalent Circuit of a Lossy Capacitance

The DuT is a lossy capacitor. There are loss mechanisms in parallel and in series with the capacitance. A representative circuit is shown in Figure 3.32. Usually, either the series resistance R_s or parallel resistance R_p dominates. So the circuit can be simplified to either a series or a parallel circuit.

However, the bridge sees only a complex impedance and therefore cannot decide between the two models. The following equation convert between the two models:

$$\begin{aligned} C_s &= (1 + D^2)C_p \\ R_s &= \frac{D^2}{1 + D^2} R_p \end{aligned} \tag{3.6.5}$$

C_s and C_p are the capacitance in series and in parallel, respectively. D is the dissipation factor:

$$D = \frac{1}{\omega C_p R_p} \tag{3.6.6}$$

For small dissipation factors $D \ll 1$, the conversion can be simplified:

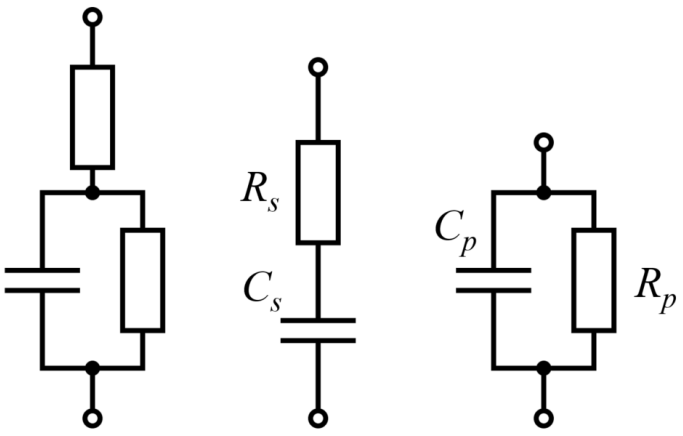

Figure 3.32: Different representations of a lossy capacitance [AH02].

$$
\begin{aligned}
C_s &= C_p \\
R_s &= D^2 R_p = \frac{R_p}{(\omega C_p R_p)^2} = \frac{G_p}{(\omega C_p)^2}
\end{aligned}
\tag{3.6.7}
$$

For small dissipation factors $D \ll 1$, both C_s and C_p return the capacitance C. Hence, the capacitance can be easily determined independent of the underlying circuit model. This is different for the resistance. Equation 3.6.7 shows that R_s and R_p are even inversely proportional to each other. The measurement itself does not allow deciding between the two. Even a DC conductance measurement does not allow deciding for one model, as the parallel resistance R_p represents an AC conductance, e.g. a lossy dielectric has a parallel AC conductivity but no DC conductivity.

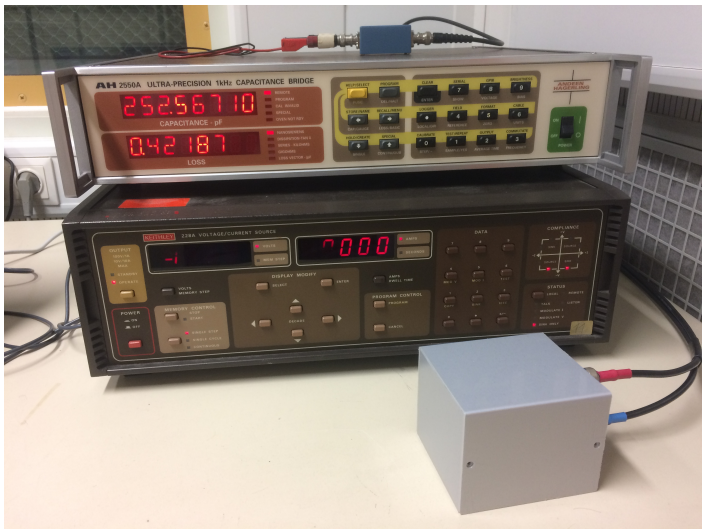

(a) Closed setup with capacitance bridge and DC voltage source in the background.

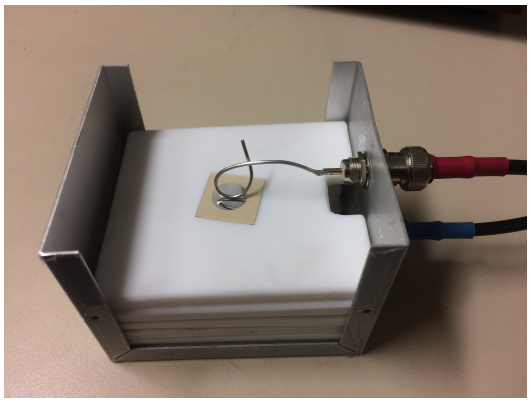

(b) Open setup with sample

(c) Close-up view Contacts with no sample

Figure 3.33: Capacitance bridge setup.

3.6.5 Shielding Setup and Sample Preparation

The bridge's resolution is best for a capacitance in the order of 100 pF to 1000 pF and conductance below 1 nS. The nominal resolution in this range is at least 10^{-6} or even 10^{-7}. The signal ΔC for a certain χ_3 increases strongly with decreasing thickness d, $\Delta C \sim d^3$. To maximize the signal, the samples should be as thin as possible. The limit is the mechanical stability in the manufacturing process. The stability is dependent on the material and the thicknesses in the order of 150 µm are possible. A metallized area of about 1 cm^2 results in the required capacitance range.
The electric shielding was realized with an aluminum box, grounded via the BNC outer conductor. Magnetic shielding is not necessary. Thereby, the resolution limit is reached with less than $0.05\,\mathrm{fF}/150\,\mathrm{pF} = 3.3 \times 10^{-7}$. The accuracy after calibration is at least 10^{-3} in the order of 1 pF to 10.000 pF. However, the accuracy is not critical for the precise measurement of the voltage dependent capacitance. A temperature-stabilized room at $(21 \pm 1)\,°\mathrm{C}$ was found to be sufficient.
The samples for the capacitance bridge measurements are thin metallized samples of the test material. After grinding to the desired thickness and polishing (surface roughness less than 1 µm), the samples are cleaned in an ultrasonic distilled water bath and then sputtered with a contact layer of 20 nm chromium and 500 nm silver on top. One sample that was instead sputtered with gold and no chromium adhesion layer turned out to have an increased loss and scratching simply allowed removing the gold layer. The samples are metallized completely from one side and only in a circular area on the other side. This avoids any mismatch of metallization areas but also avoids metallization at the edges, which can result in leakage currents. The metallization diameter is chosen sufficiently large in comparison with the thickness (approx. $200\,\mu\mathrm{m}/8\,\mathrm{mm} = 2.5\,\%$) to have the model of a thin capacitor be applicable.

Chapter 4

Results and Discussion

4.1 GHz Dielectric Nonlinearities

4.1.1 $Ba_4Al_2Ti_{10}O_{27}$ Glass-Ceramic

A suitable material to be characterized with the CDR setup was found in the glass-ceramic "Poweramic GHz33" [HLK15]. Its main crystalline phase, $Ba_4Al_2Ti_{10}O_{27}$ [SMB81], has been identified by X-ray diffraction [Mar13]. It combines sufficiently large dielectric constant ($\varepsilon_r = 32.65 \pm 0.05$) and low loss ($\tan\delta = (5.6 \pm 0.1) \times 10^{-4}$) at 1 GHz (measured with the SPDR method [Eng20]). Moreover, it has excellent mechanical properties, which allows dielectric resonators with an outer radius of 30 mm and a thickness of 24 mm with a center hole of 5 mm radius to be manufactured with a precision of 50 µm. This precision is required for the CDR method. As the glass-ceramic cannot be produced with a thickness of 24 mm, the dielectric resonator was composed of two discs with 12 mm thickness each (see Figure 3.26).

Figure 4.1 visualizes a typical output spectrum and Figure 4.2 shows an input power sweep. The powers $P_{1,sig}$ and $P_{2,sig}$ are recorded at the respective tones f_1 and f_2 together with the power $P_{3,sig}$ at the third order intermodulation frequency $f_3 = f_{\mathrm{IM3+}}$. Furthermore, the figure compares the powers displayed on the signal analyzer $P_{i,sig}$ and the signal generator $P_{i,gen}$ to the input powers into the fixture $P_{x,in}$ and output powers at the probe $P_{x,out}$. This exemplifies the power range that is covered with this nonlinear measurement: the tunable filter causes the power levels to be closer together at the signal analyzer than at the probe. While the power levels $P_{1,sig}$ and $P_{2,sig}$ at the signal analyzer are of comparable order of magnitude, the power level $P_{2,out}$ is about 20 dB lower than $P_{1,out}$ due to the suppression of the f_2-mode. The intermodulation power $P_{3,out}$ lies far below the tone powers $P_{1,out}$ and $P_{2,out}$. The power of both tones scales with 1 dB/dB over the full measured range. This is a positive control for the amplifier gain not reaching its saturation power. The intermodulation power $P_{3,out}$ shows the expected 3 dB/dB slope for low powers. At high powers, it deviates significantly from this trend.

Several arguments suggest that the saturation towards higher powers is not due to a

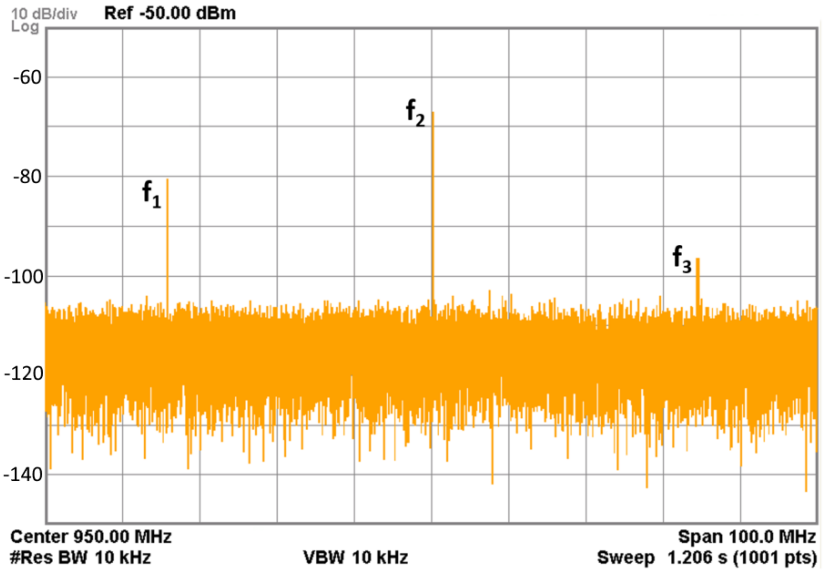

Figure 4.1: Example of a spectrum at the signal analyzer, with powers at the tones f_1 and f_2 and the intermodulation frequency f_3. For the actual data recording, only the powers at the frequencies of interest are recorded instead of a whole spectrum.

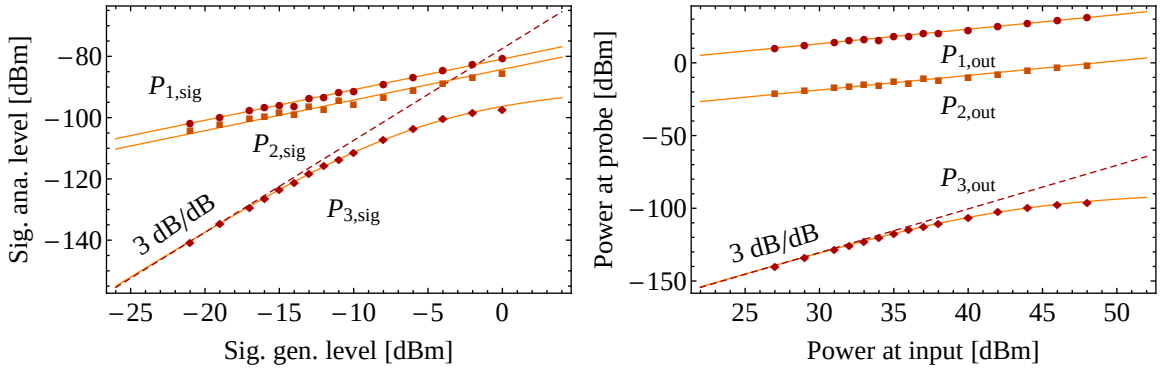

(a) Power levels at the signal analyzer

(b) Power levels at the probe

Figure 4.2: Power levels before and after the band pass filter at the output. The filter attenuates the tone powers $P_{1,out}$ and $P_{2,out}$ so that the dynamic range at the signal analyzer is much smaller than before the filter (60 dB versus 170 dB).

systematic experimental error. First, transient oscillations of the CDR system can be ruled out as the transient time is about $Q\,1/f \approx 1\,\mu s$ and recording the three power levels takes about 1 s, depending on the bandwidth. The recording is additionally delayed by 0.1 s after applying the power. Moreover, the powers $P_{1,sig}$ and $P_{2,sig}$ show that the amplifier delivers in time and the intermodulation level is recorded after recording the tone powers. Second, heating of the samples and therefore a shift in the resonance cannot be neglected. A frequency mismatch increasing with time would indeed lead to an apparent saturating intermodulation level. However, this effect can be ruled out by applying the power for a limited time and checking the frequency match after the recording of the intermodulation (see Figure 3.29). Additionally, the saturation due to heating should depend on the deposited energy; however, the saturation is

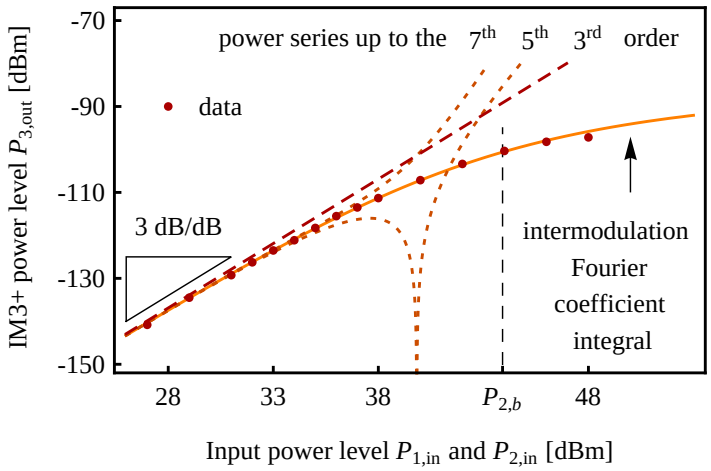

Figure 4.3: Input power dependence of the intermodulation power $P_{\mathrm{IM3+}} = P_{3,out}$, together with intermodulation trends for polynomials of up to the seventh order and the intermodulation Fourier coefficient integral from Equation 2.3.16 applied to the saturable absorber from Equation 2.4.44. $P_{2,b}$ marks the input power corresponding to E_b in the saturable absorber model, which is the radius of convergence of the power series. This figure is the diagonal cross section of Figure 4.4.

observed independently of the data point acquisition order. Furthermore, erroneous characteristics of the signal analyzer can be excluded as $P_{3,sig}$ reaches comparable levels as $P_{1,sig}$ and $P_{2,sig}$ resulting in a small dynamic range. Finally, the observation of similar intermodulation trends in literature [HCC09b, OAW+08] suggest that the saturation is not due to erroneous experimental conditions.

The tone power dependency of intermodulation signals has been discussed in section 2.3. Figure 4.3 shows the intermodulation power $P_{3,out}$ together with slope trends expected for polynomial nonlinear response up to the seventh order. Despite achieving a slightly better agreement with the data at low powers for higher order polynomials, the polynomial description clearly does not give a satisfying description. Saturating intermodulation trends have been observed for several nonlinear response functions in section 2.4, such as the function for describing the saturable absorber, the charge in a box or the binary state system. All these mechanisms show distinct intermodulation trends. Still, the data does not allow distinguishing between them unambiguously. Hence, the fit in Figure 4.3 is arbitrarily based on the saturable absorber model from Equation 2.4.44. As discussed in subsection 2.3.6, the resulting material parameters χ_3 and E_b can nevertheless be interpreted in the frame of the different models. This discussion is moved to the very end of this section.

Strictly speaking, the intermodulation amplitude is a function of two electric fields E_1 and E_2 (see subsection 2.3.5). Hence, a complete description requires separate variation of E_1 and E_2, resulting in a three parameter fit. In the logarithmic representation, these three parameters are offsets in $P_{1,in}$, $P_{2,in}$ and $P_{3,out}$. The data presented in Figure 4.4 includes independent variation of the two input powers.

To obtain the nonlinear susceptibility χ_3, The $P_{3,out}$ offset is evaluated together with

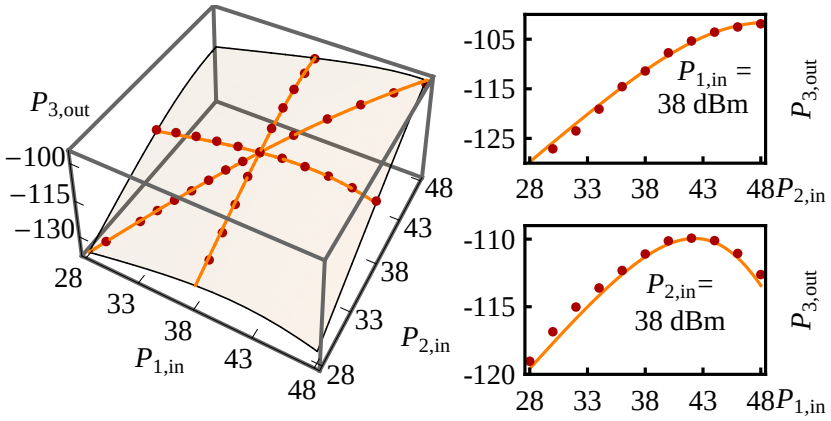

Figure 4.4: Input power dependence of the intermodulation power $P_{\mathrm{IM3+}} = P_{3,out}$ for independent input powers $P_{1,in}$ and $P_{2,in}$. The figures on the right depict cross sections for one constant input power each. Figure 4.3 shows the diagonal cross section. The underlying model is the saturable absorber from Equation 2.4.44. The coefficient of determination of the fit is $R^2 = 0.999977$.

the $P_{1,out}$ level and the knowledge of the electric field amplitude E_2 according to Equation 3.5.14. In contrast to the unknown relation of $P_{1,in}$ and E_1, the relation of E_2 and $P_{2,in}$ is known (Equation 3.5.24). Hence, the power $P_{2,b}$ can be directly translated to the electric field amplitude $E_{2,b}$. Finally, the parameter E_b in the saturable absorber model is present in both E_1 and E_2, $E_b = E_{2,b} = E_{1,b}$. The microscopic interpretation of E_b will be discussed at the very end of this section.

Low power limit

In the low power limit, the description with a simple χ_3 nonlinear susceptibility is appropriate and Equation 3.5.14 can be used to calculate χ_3. The electric field amplitude is obtained via Equation 3.5.24. For an $\varepsilon_r = 32$ dielectric resonator with an outer diameter of 60 mm, an inner diameter of 5 mm and a thickness of 24 mm, the field simulation returns $\varphi_{\mathrm{R}}/\varphi_{3\mathrm{R}} = 1.52$ and $c_{\mathrm{EW}} = 12.9\,\mathrm{kV/(mm}\,\sqrt{J})$. Further measurement parameters are listed in Figure A.5.

Figure 4.5 compares the resulting nonlinearity χ_3 to the measurements in [THNW89]: the authors were the first to use the CDR method to extract the microwave nonlinearity for their sintered ceramics. However, the data given in their publications does not allow inferring χ_3 for their sintered ceramics [NIH88, THNW89, ITNW92]. They only specify $P_{3,in}/P_{1,out}$ though $\mathrm{IM_{3M}} = P_{3,out}/P_{1,out}$ is required together with the electric field amplitude E_2 to obtain χ_3. The conversion is:

$$\frac{P_{3,out}}{P_{1,out}} = \frac{P_{1,in}}{P_{1,out}} \frac{P_{3,out}}{P_{1,in}} \tag{4.1.1}$$

The conversion factor $P_{1,in}/P_{1,out}$ is the transmission of the setup from input to output. Although this factor is not given, the transmission can be estimated from the transmission of the setup in this work. It is about −40 dB and is assumed to be within

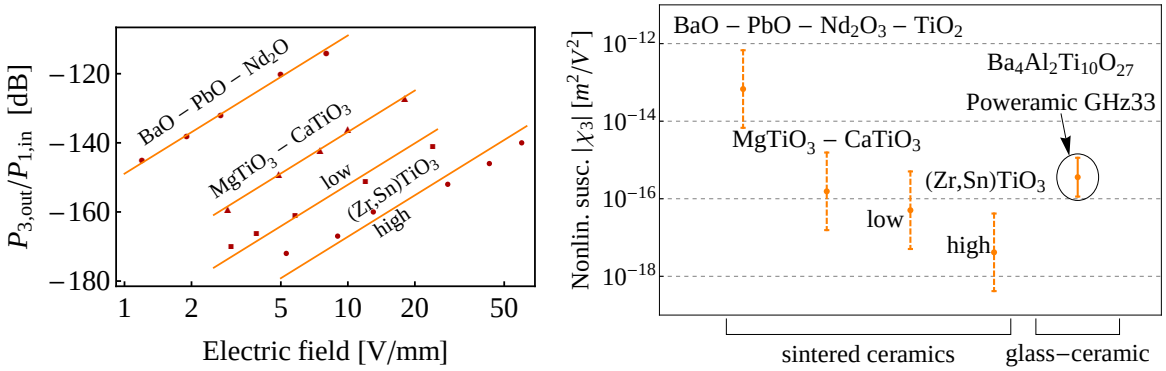

(a) Intermodulation by sintered ceramics (b) Comparison to glass-ceramic

Figure 4.5: Comparison of the nonlinear susceptibility χ_3 of sintered ceramics and the $Ba_4Al_2Ti_{10}O_{27}$ glass-ceramic of this work. (Zr,Sn)TiO_3 comes in two different purities (high and low) of the raw materials. Data for sintered ceramics and left plot adapted from [THNW89].

(-40 ± 20) dB for their work. As the nonlinear susceptibility χ_3 depends on the square root of IM_{3M}, this results in a uncertainty of ± 10 dB or two orders of magnitude.
For the estimate of the order of magnitude, the material nonlinearity χ_3 is assumed to be given by $\chi_3 = \chi_1 \xi$, so the geometric correction is $\varphi_R/\varphi_{3R} \approx 1$ (see subsection 3.5.3). The estimate in Figure 4.5 furthermore assumes that the quality factor of the resonance Q_0 is given by the inverse dielectric loss Q_d. As the fields leak into the surrounding air, the resonance quality factor Q_0 is underestimated. Finally, Q_0 does not necessarily need to be limited by the dielectric loss, especially for the low loss sintered ceramics. Instead, the metallic loss of the cavity cannot be neglected and can dominate the loss for the low loss sintered ceramics, as the calculations in [NIH88] suggests. Still, the effects of those erroneous assumptions are much smaller than the uncertainty of the guess of the transmission. The saturation of the intermodulation, which was described previously, was not observed in [THNW89] (see Figure 4.5). However, their data is rather sparse. Overall, the nonlinear susceptibility of the glass-ceramic lies in the same range as the previously measured sintered ceramics. Despite showing a larger dielectric loss than all sintered ceramics, the nonlinear response is comparable. Thus, the glass-ceramic does not fit in the $\tan\delta \sim \chi_3$ correlation found in [THNW89]. In [ITNW92], the high purity (Zr,Sn)TiO_3 was found to serve in filters with sufficient isolation, which suggests that $\chi_3 \approx 10^{-17}\,\mathrm{m^2/V^2}$ is suitable for resonant structures. The glass-ceramic, which has not been optimized at all for such purposes yet, lacks only about one order of magnitude to meet this benchmark.

Reproducibility, uncertainties and sources of errors

The uncertainty for the $Ba_4Al_2Ti_{10}O_{27}$ glass-ceramic displayed in Figure 4.5 is a factor of two, the reproducibility of the measurements. The histograms in Figure 4.6 visualize this reproducibility. All 13 measurements lie within a factor of 8 and 60 % of the measurements lie within a factor of two. Both the distribution for χ_3 and E_b exhibit an asymmetry towards lower values. The 13 measurements were performed over a period

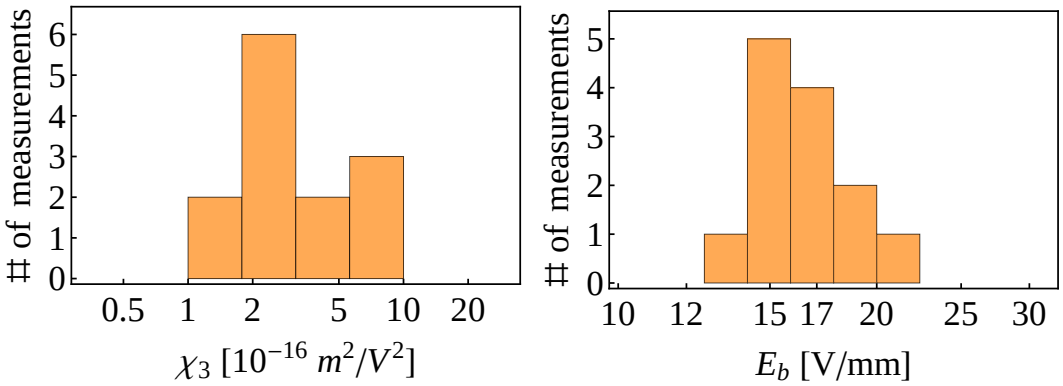

(a) Nonlinear susceptibility χ_3 (b) saturation field amplitude E_b

Figure 4.6: Histograms for the two fit parameters.

of 18 months. In-between each measurement, the samples were removed from the cavity and newly adjusted.

As previously mentioned in this section, the input power dependency fit has three free parameters. However, the offset in $P_{1,in}$ does not contain valuable information except for checking the quality of the fit. Hence, a simple two-parameter fit of a single constant ratio power sweep is sufficient to determine both χ_3 and E_b. The underlying fit is based on $E_1 = E_2$. Although this is not realized in the experiment, the resulting χ_3 is not at all influenced by that simplification and E_b is only influenced within about 1 dB. This simplification works because the intermodulation trend for a fixed amplitude ratio E_2/E_1 is mostly independent of the actual amplitude ratio (3 dB/dB at low amplitudes, 0 dB/dB at high amplitudes) and only shows a slight distinctive feature in the curvature in the intermediate power range.

Figure 4.7 illustrates the reproducibility of the direct measurands $P_{1,out}$, $P_{2,out}$ and $P_{3,out}$ as a time series of the output powers at $P_{1,in} = P_{2,in} = 28$ dBm input power. As expected, $P_{2,out}$ is always smaller than $P_{1,out}$. The measurements with close $P_{1,out}$ and $P_{2,out}$ levels coincide with low $P_{1,out}$ levels. These measurements #1 and #5 also show a large asymmetric splitting with a frequency mismatch δf =0.9 MHz and 1.0 MHz,

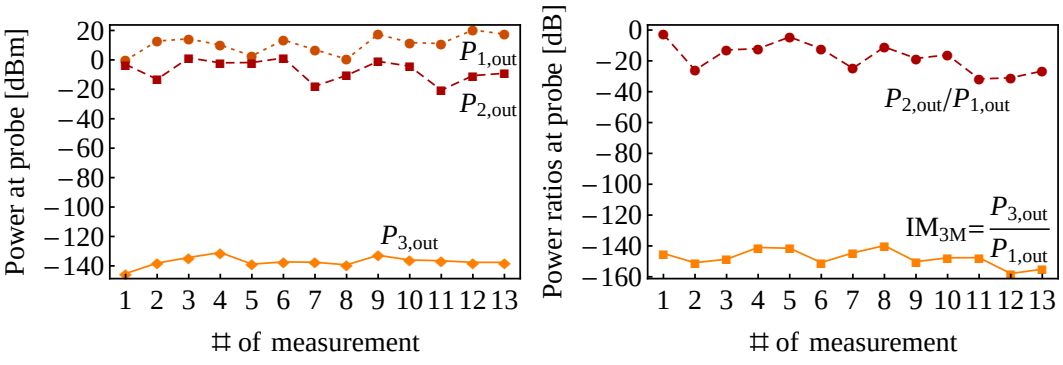

(a) Absolute power (b) Power ratios

Figure 4.7: Time series of the output powers.

respectively. Therefore, this could be related to the mismatch; however, mismatch δf and $P_{2,out}/P_{1,out}$ do not show any further correlation.
The power ratio $\mathrm{IM_{3M}}$ has a larger variation than the absolute intermodulation power $P_{3,out}$ and the variation in $\mathrm{IM_{3M}}$ is dominated by the variation of $P_{1,out}$. This contradicts the model assumption of having comparable amplitudes E_1 and E_3 above the center resonator, which should lead to strongly correlated power levels $P_{1,out}$ and $P_{3,out}$. A parallel f_1 transmission that does not happen via the dielectric resonators and therefore does not contribute to intermodulation generation could be a possible source of that variation. A large variation in $P_{2,out}$ on the other hand does not surprise, as a match with the anti-resonance of the center resonator $\mathrm{S_B}$ crucially influences the power level that is detected above it, because the second mode frequency f_2 of the coupled system almost matches the mode of the isolated dielectric resonator f_B (see Figure 3.17a).
All parameters that are needed to deduce the nonlinear susceptibility χ_3 can be determined with higher precision than the reproducibility suggests. This includes the input power $P_{2,in}$ ($\pm 0.1\,\mathrm{dB} \approx 2\%$, the reflection parameter S_{22} ($\pm 0.1\,\mathrm{dB}$), the resonance quality factor of the resonance (less than 2%) and the resonance frequency (less than 1 ppm). The intermodulation ratio $\mathrm{IM_{3M}}$ can be determined with even higher precision due to the regression. The field simulations produce resonance frequencies conforming to those from the experiment within a few MHz, which suggest that the field distributions are accurate enough to be neglected in comparison to the error sources, which have been proposed so far. Overall, these uncertainties cannot account for the reproducibility that is actually observed. However, the underlying model has several assumptions that can be sources of error:

- Assumption: All absorbed power $P_{2,abs}$ goes into the $\mathrm{TE_{01\delta}}$-mode of the coupled system ($\mathrm{T_2}$, $\mathrm{S_C}$, $\mathrm{S_B}$, $\mathrm{S_A}$).
  Validity: Indeed, Figure 3.8 perfectly supports this assumption. While the excitation of the $\mathrm{HEM_{11\delta}}$-modes was observed to be strongly dependent on the angle of the input coupling loop, the $\mathrm{TE_{01\delta}}$-mode has been clearly identified and found to be independent of the angle. The off-resonance reflection parameter S_{22} is about $-1\,\mathrm{dB}$ (after calibration). This means that, even off-resonance, about 20 % of the power are not reflected but are lost in the cavity or input system. However, this loss is accounted for by subtracting the plateau from the input S-parameter.

- Assumption: The stored energy is equally distributed between the trap resonator $\mathrm{T_2}$ and the sample resonators $\mathrm{S_C}$ and $\mathrm{S_A}$.
  Validity: This is only the case for $c_{\mathrm{I=J}}$ coupling. This coupling can be arranged within $\Delta\omega = 0.5\,\mathrm{MHz}$ corresponding to less than 0.1 %. As visible in Figure 3.13, the energy distribution does not strongly depend on the coupling around the $c_{\mathrm{I=J}}$ (the derivative at the maximum is zero). Hence, the amplitude distribution is expected to hold within a few percent.

- Assumption: The stored energy is distributed between the three resonators S_A, S_B and S_C according to the amplitudes calculated in subsection 3.4.1.
  Validity: Strictly, this is only the case for equal coupling between the sample resonators S_A-S_B and S_B-S_C. However, a brief calculation shows that the amplitude ratio E_A/E_C is not very sensitive to unequal coupling (see Equation A.0.11). The resonators can be positioned with a precision of 1 mm at 33 mm. Hence, the model is expected to hold within a few percent.

Overall, the uncertainties in the model cannot account for the variance that has been observed in the measurements. This suggest that further model parameters exist, which have not been controlled for. Nevertheless, based on the reproducibility, it is reasonable to declare that the nonlinearity has been determined to

$$|\chi_3^{1\mathrm{GHz}}| = (4 \pm 2) \times 10^{-16}\,\mathrm{m^2/V^2}$$

For dielectrics with similar linear properties, the setup is expected to have a sensitivity at least one order of magnitude smaller, $|\chi_3| > 10^{-17}\,\mathrm{m^2/V^2}$.

E_b and microscopic interpretations

As discussed in subsection 2.3.6, the bending electric field amplitude E_b is a convenient characteristic of a nonlinear mechanism. The measurement of E_b enables comparing predictions of various models.

The authors of [THNW89] proposed nonlinear interatomic forces to be the source of the nonlinear susceptibility. As introduced in subsection 2.4.3, such optical phonons can indeed reach $10^{-16}\,\mathrm{m^2/V^2}$ nonlinearities. Moreover, subsection 2.4.7 motivated that the underlying model, even though assuming $T = 0\,\mathrm{K}$, is appropriate at ambient temperatures. Still, this phononic model corresponds to a distributed (large N small p) nonlinearity: As such, it cannot account for the saturating intermodulation at electric field amplitudes of 10 V/mm. Instead, some localized (small N large p) models, which have been introduced in subsection 2.4.7, indeed produce a saturating intermodulation response. These shall be discussed in the following. Moreover, the following discussion is based on a field correction factor of $L = 10$, which is the factor based on the Lorentz field for $\varepsilon_r = 28$ (see subsection 2.4.1).

Both orienting dipoles (Equation 2.4.27) and the charge in the box model (Equation 2.4.63) result in a Langevin-like response. Although freely rotating permanent dipoles seem unlikely in a solid with ionic bonds, [PSW+11] takes them as a basis to explain the low frequency nonlinear response of SiO_2. On the other hand, the charge in a box potential, which also results in a Langevin response, can be interpreted as a locally free charge. In this model, the dipole that is required to obtain a saturation field of $E_b = 10\,\mathrm{V/mm}$ is in the order or $10^{-25}\,\mathrm{C\,m}$, which is about 10^4 atomic dipoles (eÅ). For a single electric charge, this would require a box of 1 µm. This length corresponds to the size of the crystallites in the glass-ceramic Figure 4.21. However, assuming typical diffusion velocities of 100 µm/s (in metals), single charges do not cover such distances

within the reversal of the electric field at 1 GHz. On the other hand, grain boundaries have already been associated with dielectric losses [SSTNS+18], which could also exhibit a strong nonlinear response. In addition, inhomogeneous dielectric properties alter the local electric field, presumably leading to field peaks and thereby enhancing the nonlinear response [PCGM12].

The same order of magnitude of a dipole ($10^4\,e$Å) is also required for the binary state model (Equation 2.4.66). Such a binary state system could for instance originate from a local ferroelectric behavior with a correlated switching of 10^4 atomic dipoles. Although $Ba_4Al_2Ti_{10}O_{27}$ is not ferroelectric, its perovskite structure is very similar to that of the ferroelectric $BaTiO_3$. The large permittivity of $Ba_4Al_2Ti_{10}O_{27}$ already points in the direction of a (compositional) phase transition to a ferroelectric. Furthermore, the perovskite structure is known to exhibit an exceptional high local electric field [Sla50].

All the mechanisms so far rely on a dipole that that is sufficiently large to balance the thermal energy ($pE_{loc} \approx k_\mathrm{B}T$). A model that does not require such a large dipole is the saturable absorber (see subsection 2.4.5). In return, it requires a resonant system in the order of 1 GHz. Taking an atomic dipole as a basis, the model requires a mean lifetime of 0.1 ns of the upper state of the resonant system. Larger dipoles proportionally allow shorter lifetimes. Such microwave saturable absorbers have been discussed as the source of nonlinearity in MgO substrates in high temperature superconducting devices [HHH+03].

While E_b is characteristic for a nonlinear mechanism and independent of the mechanism's abundance in the dielectric, E_b in combination with χ_3 allows the determination of the linear contribution of the nonlinear mechanism χ_1 (see Equation 2.3.28). The linear susceptibilities are in the same order of magnitude independent of the underlying model. Hence, it is possible to estimate the nonlinear susceptibility independently of the concrete model: The contribution to the linear susceptibility is in the order of $\chi_1 \approx 10^{-8}$. This shows that the nonlinear mechanism is barely present in the material; however, it dominates the nonlinear response. This is crucially different from linear dielectric properties: while a high loss mechanism that is barely present in the dielectric does only lead to a small loss, a fractional nonlinear mechanism can dominate the overall nonlinear response. This argument also works in the other direction: the mechanism that is responsible for the nonlinearity can be invisible in both loss and relative dielectric constant, i.e. $\mathrm{Im}(\chi_1) \approx \mathrm{Re}(\chi_1) \approx 10^{-8}$ will not be visible in the loss $\tan\delta \approx 10^{-3}$.

From the linear susceptibility χ_1, the density N of the mechanisms in the dielectric can be estimated. For the binary state model and the charge in a box model, a density of $N \approx 10^9\,\mathrm{m}^{-3}$ is required; still, based on a local electric field correction $L = 10$. This is much smaller than the density of e.g. the crystallites in the glass-ceramic (about 1 µm distance between the crystallites leads to a density of $10^{18}\,\mathrm{m}^{-3}$). For the saturable absorber, the required density is much larger ($N \approx 10^{25}\,\mathrm{m}^{-3}$), as a resonant system with 1 GHz splitting is almost equally occupied ($hf \ll k_\mathrm{B}T$) and does not lead to a strong polarizability. This large density makes the saturable absorber seem rather improbable.

4.1.2 N-SF66 Glass Dopant Series

Motivated by the observation of a dependency of the nonlinearity on the purity of the minerals in [THNW89], a dielectric is systematically doped with typical impurities found in minerals: iron, and sodium as a representative of alkali metals.

However, doping a glass-ceramic has two disadvantages: First, the respective green glass is usually prone to spontaneous crystallization (devitrification). Hence, the green glass cannot be deliberately doped while still obtaining a suitable glass for ceramization. Second, a glass-ceramic always requires an additional comparatively time intense production step, the ceramization of the green glass.

Therefore, a glass is more suitable, preferably a "stable" glass that will not devitrify easily under doping. Furthermore, a high ε_r is required to enable dielectric resonators. A corresponding glass was found in N-SF66. Originally, it is a high refractive index ($n = 1.9$) optical glass [Opt20]. However, it also possesses a large permittivity at 1 GHz ($\varepsilon_r = 21.1$).

Still, as discussed in subsection 3.5.2, not all materials that enable dielectric resonators are suitable for the CDR method. The glass N-SF66 turned out to be one of those. However, the range of testable materials can be extended with the CsDR method. This method was found to work for the N-SF66 glass in combination with the glass-cermic

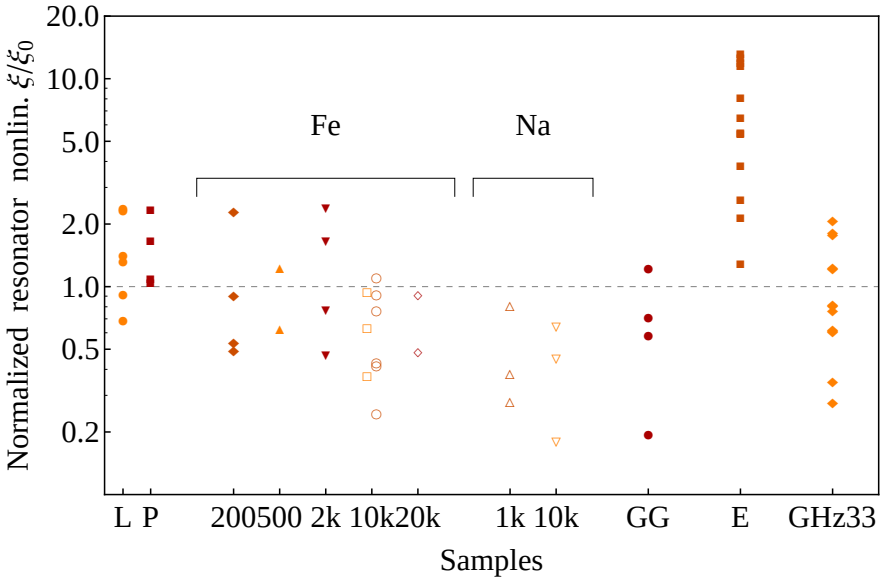

Figure 4.8: Normalized resonator nonlinearity ξ/ξ_0 for different samples. L: N-SF66 laboratory sample, P: N-SF66 production sample, Fe: N-SF66 doped with Fe_2O_3 (concentration in mass-ppm), Na: N-SF66 doped with Na_2O (concentration in mass-ppm), E: N-SF66 streak probes, GG: Poweramic GHz33 green glass, GHz33: Poweramic GHz33 glass-ceramic. The E samples are also doped samples with 500 wt ppm Fe_2O_3. ξ_0 is calculated with the arithmetic mean of χ_3 of Poweramic GHz33 obtained with the CDR method. The Fe10k results consists of two columns. The left column (squares) represents measurements with 2 test discs (2×4 mm) between the resonator discs. The sets of data points for each sample show the reproducibility.

Poweramic GHz33 as the resonator material. Additionally, the green glass of Poweramic GHz33 was also found to be suitable for characterization with the CDR setup (dielectric properties in Figure A.6). Figure 4.8 summarizes the measured normalized resonator nonlinearity ξ/ξ_0 (see subsection 3.5.3) of the dopant series. All samples have the same geometry: a disc of 4 mm thickness and an outer diameter of 60 mm. They are mounted between two Poweramic GHz33 discs of 12 mm each, as depicted in Figure 3.26b.

Strictly speaking, all samples except for the streak samples (E) lie within the reproducibility of the resonator material and are therefore consistent with $\chi_{3D} = 0$. However, this still allows specifying an upper limit, $|\chi_3| < 10^{-15}\,\mathrm{m^2/V^2}$. This sensitivity of the CsDR setup is limited by the precision of the CDR method. While the laboratory sample L and production sample P seem to really be consistent with $\chi_{3D} = 0$, the Na samples exhibit only values $\xi < \xi_0$. This is also applies to the Fe10k and Fe20k samples. One ξ/ξ_0 value can be interpreted as originating from two χ_{3D} values. Furthermore, the unknown sign of the resonator nonlinearity χ_{3R} gives again a multiplicity of two. Hence, there are four possible values for χ_{3D}. Figure 4.9 arbitrarily assumes that $\chi_{3R} > 0$, so negative values in Figure 4.9 should be interpreted as having an opposing sign to χ_{3R} and positive values as having the same sign as χ_{3R}.

For the Fe10k samples, enough discs were available to measure two test discs (2×4 mm) inserted between the resonator discs. These measurements can be used to check whether the minus sign branch or the plus sign branch in Equation 3.5.16 is more reasonable. The comparison in Figure 4.9 shows that in the plus sign branch, both geometries agree with a single χ_{3D}, while the minus sign branch interpretation leads to nonconforming χ_{3D}. Of course, these interpretations need to be treated carefully, as strictly speaking, all values are anyway consistent with $\chi_{3D} = 0$. The ambiguity of the sign furthermore does not allow deciding if the nonlinearity increases or decreases with added Na or Fe. While both series show a trend of decreasing ξ/ξ_0 with increasing dopant content, this can be interpreted as both an increasing or a decreasing nonlinearity with increasing dopant content. Underlying the measurements with two Fe10k discs, the increased dopant content leads to an increasing absolute nonlinearity χ_{3D}.

The influence of the dopants on the linear properties was characterized with the SPDR method (section 3.3). The results can be found in Figure A.7. Adding Na or Fe both decreases the dielectric constant and the loss, though in a way that is negligible for the CsDR setup. Fe was suspected to be a source of magnetic nonlinearity and loss acting as a pseudo-dielectric nonlinearity and loss. However, this conjecture has been theoretically ruled out in subsection 2.4.8 and now has been shown experimentally to have no measurable effect on the nonlinearity. An increased Fe content even leads to lower dielectric loss in the N-SF66 glass. The limited sample size did not allow measuring the dielectric properties with the SPDR at the explicit frequency of the CsDR setup (~ 1 GHz). Nevertheless, the qualitative trends are expected to be independent of the frequency so that they can be extrapolated towards lower frequencies.

A decreasing ξ/ξ_0 was observed for an increased dopant concentration. Still, it is not possible to correlate lower loss to lower nonlinearity because of the ambiguousness in

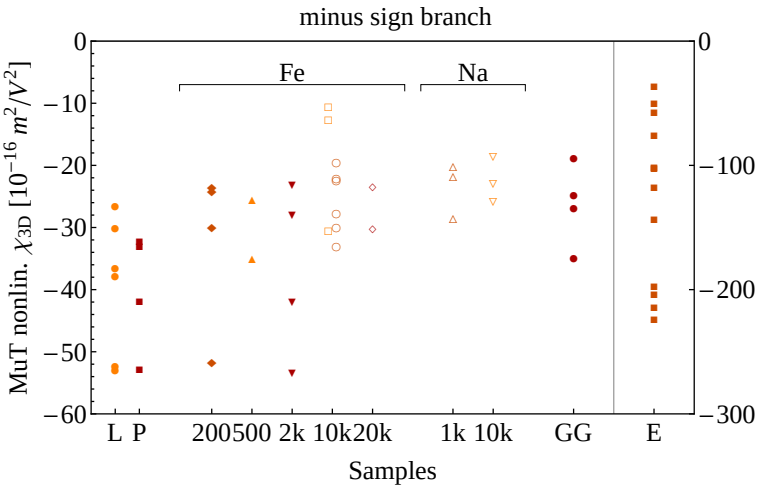

(a) minus branch

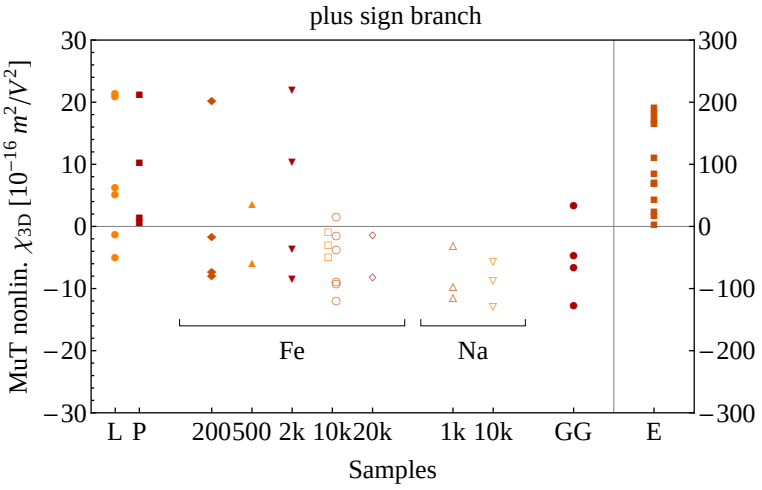

(b) plus branch

Figure 4.9: Nonlinear susceptibility χ_{3D} of the MuT for the plus and the minus sign branch of Equation 3.5.16 visualized in Figure 3.21. The scale for the streak samples (E) is different and can be seen on the right of each plot.

the sign of the nonlinearity. Basing the interpretation on the measurements with two Fe10k discs, the absolute nonlinearity even increases with decreasing loss.

Next, Figure 4.10 summarized the second fit parameter, the saturation electric field amplitude E_b. First, the saturation of the intermodulation power is observed in all measurements and the resulting E_b all lie within a factor of two. Even though the Na samples show both a low E_b and a low ξ/ξ_0, there is no general correlation between ξ/ξ_0 and E_b. Even the streak samples (E), which exhibit a significantly larger ξ/ξ_0, show a similar E_b.

The next paragraph resumes the discussion on the sign of the nonlinearity. Measurements in the CsDR setup resulting in $\xi < \xi_0$ certainly lead to opposing signs of χ_{3D} and χ_{3R}. This is the case for all Na samples and the highly doped Fe samples. Of course, the $\xi < \xi_0$ effect is not significant, the possibility of compensating nonlinearities shall be

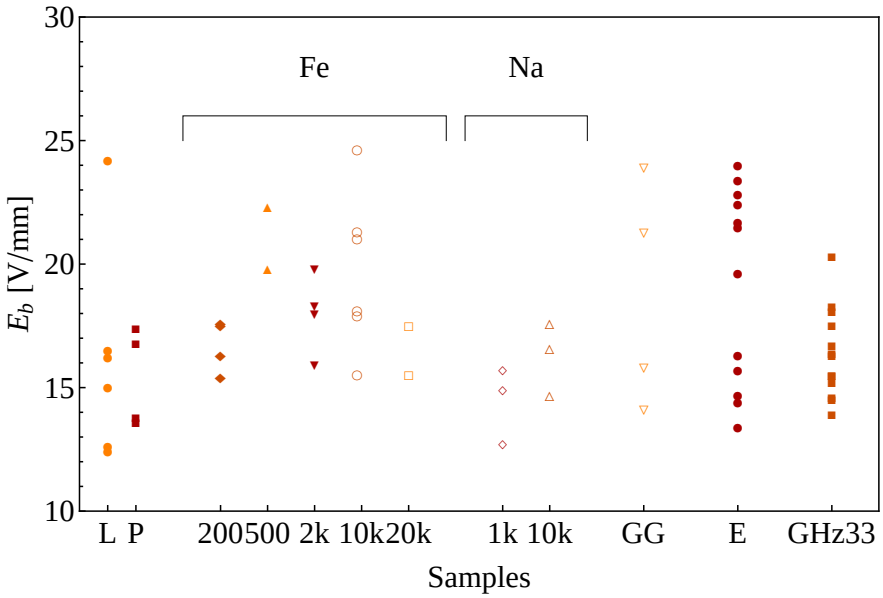

Figure 4.10: Saturation field amplitude E_b for the glass dopant series. The x-axis lists the different samples as in Figure 4.8.

addressed anyway.

For third order nonlinear responses, the compensation works over the complete power range: $y(x) = -ax^3$ and $z(x) = +bx^3$ just yield $y(x) + z(x) = (b-a)x^3$. Naturally, a and b are required to be of the same order of magnitude to observe the compensation. However, for more general nonlinearities, the situation is more intricate: to obtain an intermodulation trend like the observed one while assuming different signs requires the E_b of the two mechansims to be precisely the same. Otherwise, there would be always a power at which both nonlinearities compensate completely, resulting in a dip in the intermodulation trend. Clearly, this was not observed. This further supports the hypothesis that the $\xi < \xi_0$ effect is not significant and hence not due to compensating nonlinearities.

The physical models discussed so far that have a saturating intermodulation only had negative third order nonlinearities. However, the intermodulation signal can also saturate for positive nonlinearities, as in the geometric nonlinearity in Equation 2.3.22. However, this model is rather artificial and no other physically plausible positive saturating nonlinearity model was found. Still, it is possible that the macroscopic nonlinear susceptibility stems from compensating mechanisms within a single material. Metal-insolator-metal capacitors already take advantage of such compensating nonlinearities [JACJ+19] and [BCD18] uses this theoretical construct to propose optical fibers that are tailored to zero nonlinearity. The same might be possible in the microwave range, if mechanisms of different signs are identified.

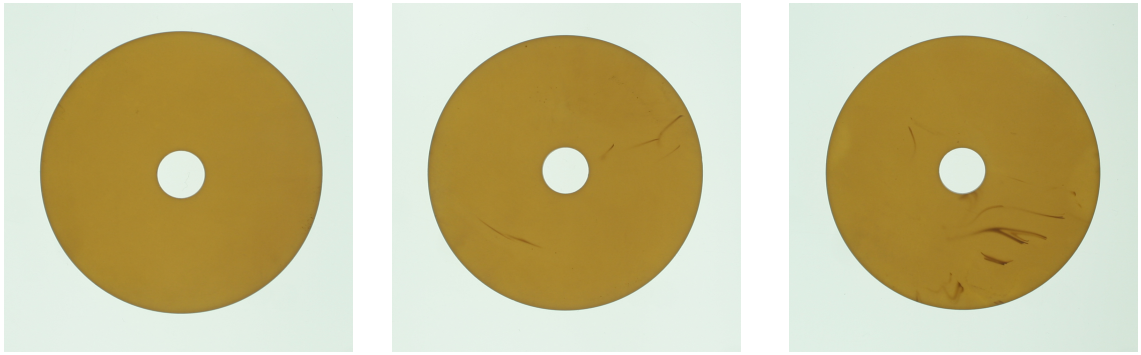

(a) streaks E1 (b) streaks E2 (c) streaks E3

Figure 4.11: N-SF66 streak samples (E). E1 does not actually show any visible streaks, however, it was fabricated from the same melt as the samples E2 and E3, which exhibit clearly visible streaks. The outer diameter of the samples is 60 mm.

Streak samples

The most significant increase in the nonlinearity correlates with the streaks in the sample (see Figure 4.11), resulting in a $|\chi_3| = (1.0 \pm 0.5) \times 10^{-14}\,\mathrm{m^2/V^2}$. Figure 4.12 depicts an exemplary output signal of the streak samples, showing that the intermodulation power can even cross the tone power. Although the increase in the resonator nonlinearity is significant for the streak samples, no significant correlation with the amount of streaks was found neither by permuting the streak sample nor by combining the streak samples (E) with laboratory samples of N-SF66 (L). As long as at least one sample with streaks (E2 or E3) is mounted either in resonator S_A or S_C, the intermodulation level increases. Figure 4.13 shows two microscope images of the streaks. The optical image shows the milky phenomenology of the streaks and their localized structure. The scanning electron microscopy (SEM) image shows a section with streaks as an overview and as a close-up image of some drops. The regions with streaks were investigated with energy-dispersive X-ray spectroscopy (EDX) and were found to have an excess of Si. This fact suggests that the drops are composed of SiO_2. As SiO_2 is not a component of

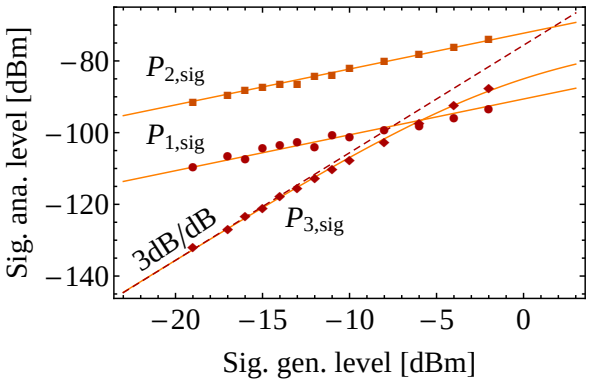

Figure 4.12: Exemplary intermodulation trend of the streak samples (E). The displayed powers are powers at the signal generator and the signal analyzer. It shows that the power at the intermodulation frequency f_3 can be even larger then the power at f_f.

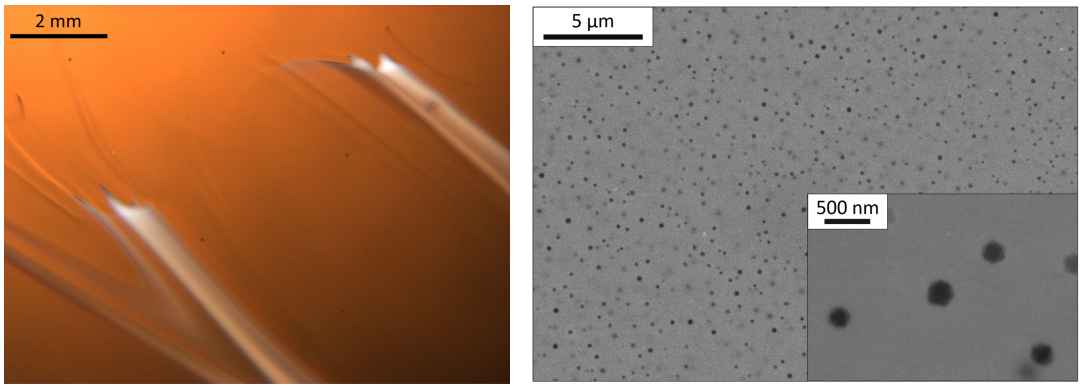

(a) Optical microscopy of the streaks (b) SEM image of the streaks

Figure 4.13: Microscope images of the streaks [Val21].

N-SF66, the SiO_2 most likely originates from the crucible that was used to melt the glass. The small and monodisperse drop size (∼250 nm) suggest that the SiO_2 particles were not mechanically separated from the crucible. Instead, the SiO_2 was first solved into the glass melt and then separated due to immiscibility at lower temperatures. The local occurrence of the streaks can be explained by a higher concentration of SiO_2 at the bottom of the crucible, which can only be partly stirred. The drop form does not allow distinguishing a crystalline or an amorphous state of SiO_2, even though the drops suggest some six-fold symmetry, which is expected for crystalline SiO_2. However, measurements at kHz frequencies propose that SiO_2 has a nonlinear response below the sensitivity of the CsDR setup ($\chi_3 \approx -10^{-18}\,\mathrm{m^2/V^2}$) [PSW+11]. Instead, the drops suggest that the increased nonlinearity might actually originate from the interface of the drops to the bulk N-SF66 glass. It is remarkable that the streaks neither induce a measurable change in the dielectric constant nor in the loss (no detectable shift and no change in the quality factor of the dielectric resonator's resonance), while the influence on the nonlinearity is significant. This conforms to the discussion of the microscopic sources in subsection 4.1.1, which are visible in the nonlinearity but too small to be detected in either permittivity or loss.

The nonlinear response of the streak glass sample and the glass-ceramic do not necessarily originate from the same mechanism; however, the increased nonlinearity in the streak samples suggest that the nonlinearity in the glass-ceramic might stem from a similar mesoscopic mechanism associated with inhomogeneity such as grain boundaries. Moreover, the streak samples (E) also show the saturating intermodulation trend with a comparable saturation amplitude E_b. A comparable E_b with increased χ_3 could for instance result from the same mechanism, which is more abundant in the streak samples than in the $Ba_4Al_2Ti_{10}O_{27}$ glass-ceramic.

The streak sample measurement has one more implication that is important. In subsection 3.5.1 it was qualitatively argued how the setup prevents intermodulation generation in the input and the output system. The S-parameter measurements (high isolation S_{21} between the inputs, suppression of f_2 at the output) support the

argumentation. Still, a measurement of a single material does not allow ascribing the intermodulation generation to that material with certainty. Nevertheless, from the set of material measurements, it is certain to attribute the intermodulation generation to the material: The CsDR streak samples (E), the laboratory (L) and the production samples (P), all having the indistinguishable linear dielectric properties and the same geometric properties, lead to a distinct intermodulation response. This allows ascribing the nonlinear response to the material with high certainty. On the other hand, for the CDR method, an experimental proof that the intermodulation originated from the dielectric itself is still lacking, as the CDR method does not allow reference measurements without a test material.

4.2 kHz Dielectric Nonlinearities

The nonlinear susceptibility of several glass samples and the $Ba_4Al_2Ti_{10}O_{27}$ based glass-ceramic Poweramic GHz33 was measured with the kHz ultra-high precision capacitance bridge introduced in section 3.6. Besides the nonlinear response to the voltage, the change in capacitance is dominated by the temperature drift. To compensate for that drift, a time series of the capacitance is recorded and the DC bias voltage is switched on and off in regular intervals. A representative time series of the capacitance and the conductance is shown in Figure 4.14. It depicts the decrease of the capacitance due to the temperature drift as well as the fall and rise of the capacitance when the bias voltage is turned on and off, respectively. This change in capacitance ΔC upon application of the bias voltage is in the range of a about 4 fF for a capacitance of $C_0 = 180.9\,\mathrm{pF}$, corresponding to a relative change of 22 ppm. The capacitance change ΔC is extracted by offsetting the data recorded with the bias voltage V and fitting a polynomial to the adjusted data. The offset is chosen such that the sum of the residuals of the polynomial fit is minimized. This procedure is repeated for a set of voltages. The resulting $\Delta C(V)$ shows a parabolic form (see Figure 4.18), which can be fitted with Equation 3.6.4 to obtain the nonlinear susceptibility χ_3.

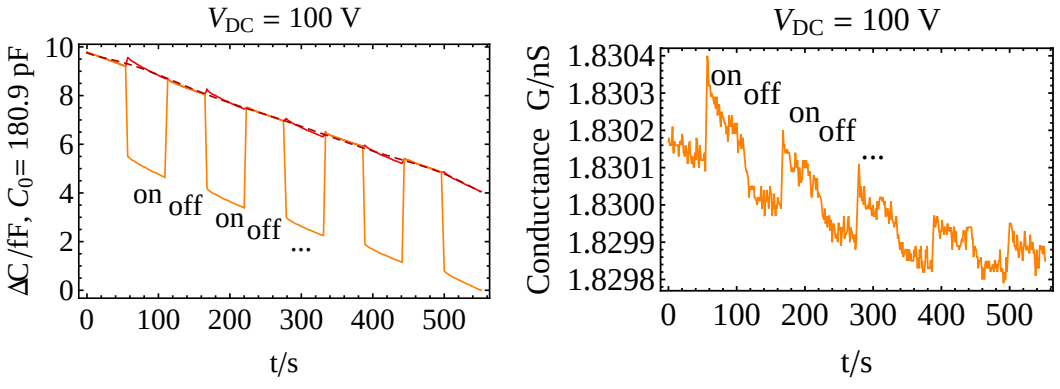

(a) Capacitance (b) Conductance

Figure 4.14: Time series of the Poweramic GHz33 sample #0-3 at 100 V.

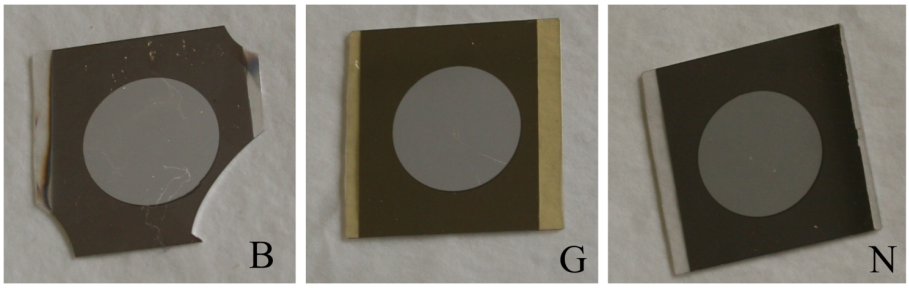

Figure 4.15: Glassy samples investigated with the high sensitivity capacitance bridge: (B) Borofloat (nominal thickness 100 µm), (G) Poweramic GHz33 green glass (nominal thickness 250 µm), and (N) N-SF66 (nominal thickness 250 µm). The metallization diameter for all samples is 12 mm.

Two features shall be mentioned briefly, but they will not be further discussed in this work. First, the nonlinear response of the capacitance partly consists of a contribution with an exponential-like relaxation with a time constant in the order of 10 s. It is supposed that the relaxation response originates from the metallization/dielectric interface. However, this effect is dominated by an instant (< 1 s) change in the capacitance. Second, the conductance also shows a voltage dependency. As the loss is expected to originate from the metallization contact, this nonlinear response is not further investigated.
Several samples have been investigated with this method, including the glasses Borofloat, N-SF66 and the green glass of Poweramic GHz33 (samples depicted in Figure 4.15). However, only the glass-ceramic Poweramic GHz33 showed a measurable nonlinear response.

4.2.1 $Ba_4Al_2Ti_{10}O_{27}$ Thickness Series

The glass-ceramic Poweramic GHz33 showed a significant, though only a few ppm, decrease in capacitance if a bias voltage was applied. To check if the nonlinear response conforms to a single bulk property χ_3, both the area A and the thickness d of the samples are varied. Varying A and d lead to different ΔC, however, they all should result in the same χ_3. Figure A.12 shows the fabricated samples and Table A.1 lists their properties.
Figure 4.16 shows the linear permittivity and the loss for samples of different thicknesses. The permittivity varies within the measurement uncertainty of $\sim 1.5\,\%$, though samples #0-3, #1-1 and #1-2 exhibit an elevated permittivity. Sample #0-3 has a smaller metallization diameter. As the simple capacitor model neglects all fields outside the capacitor, the elevated permittivity for the small metallization might originate from the non-negligible contribution of these outer fields. Samples #1-1 and #1-2 are round discs. The metallization area was evaluated by counting pixels on the images. The round samples were evaluated differently than the rectangular samples, which could therefore lead to the systematic error. Besides that, samples #0-1, #0-2 #0-3, #1-1

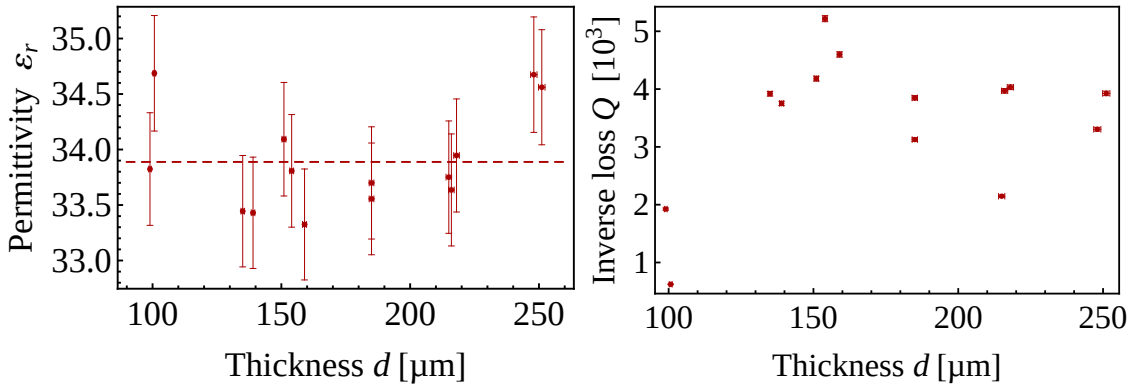

(a) Permittivity (b) Inverse loss

Figure 4.16: Linear dielectric properties of Poweramic GHz33 samples as a function of sample thickness.

and #1-2 belong to a different production batch than the other samples (see Table A.1). Still, #0-1 matches in the trend of the majority of the samples.

Next, the loss significantly varies between the samples. Such significant deviations are more likely to originate from to varying metallization interface resistances than from the bulk dielectric loss. Sample #0-2 was excluded from further evaluation because it showed large changes in the capacitance that are uncorrelated with the applied voltage. It is suspected that fractures beneath the metallization lead to such a behavior.

Figure 4.17 summarizes the nonlinear susceptibility measurements for the thickness series. All samples show a negative susceptibility in the order of $10^{-13}\,\mathrm{m^2/V^2}$. The majority of the samples agree within the measurement uncertainty, though some samples significantly deviate. For instance, the deviating samples #5 and #10 exhibit a fracture that is close to the circular metallization and a metallization on that fractures itself (see Figure A.9). Samples #0-3, #1-1, #1-2 showed the elevated permittivity.

The independence of the sample thickness and the symmetric response is a necessary

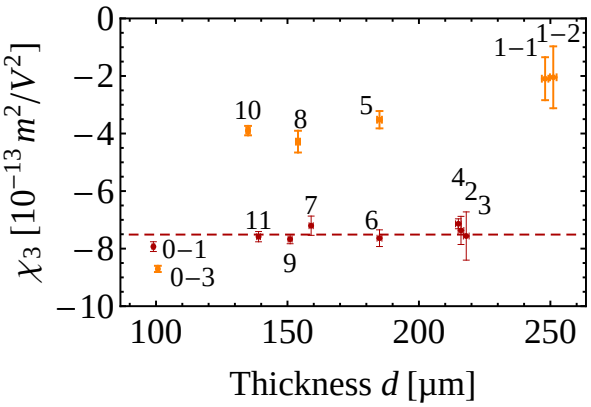

Figure 4.17: Nonlinear susceptibility of Poweramic GHz33 samples for different sample thicknesses. The lighter data points were excluded from the mean value calculation as discussed in the text.

condition for attributing the effect to a bulk material nonlinear susceptibility; still, it is not sufficient to exclude an interface nonlinear response. On the other hand, there is no systematic trend with the sample thickness either, which would clearly suggest an interface effect. The significant difference in the nonlinear susceptibility can be explained either by different interface properties or even with a difference in bulk dielectric properties, which would mean that the glass-ceramic samples are not as homogeneous as assumed. Additionally, the negative nonlinear susceptibility is opposed to most MIM measurements, where interface effects are expected to lead to increase in capacitance upon an applied voltage [VGJEK10].

Modeling the interface by a capacitance C_I in series to the bulk capacitance C_B leads to an overall capacitance C_G of the form:

$$C_\mathrm{G} = \frac{C_\mathrm{I} C_\mathrm{B}}{C_\mathrm{I} + C_\mathrm{B}} \tag{4.2.1}$$

In this series circuit, C_G is always smaller than both C_I and C_B. Measuring a C_G that conforms to the expected C_B is a good indicator that C_I is sufficiently shortened ($G_\mathrm{I} > \omega C_\mathrm{I}$). This is the case for the linear capacitance measurements: the permittivity is even 3.6 % higher than the one measured with the SPDR at 1 GHz. This theoretically allows assigning the voltage dependent capacitance of this series circuit to the nonlinearity to the bulk capacitance itself.

Still, to investigate the effect of the interface more thoroughly, a gold metallization instead of the chromium/silver metallization was planed. However, the mechanical contact of the gold was not sufficient for the characterization. Another way to investigate the interface could be a controlled series with different degrees of polishing of the surface before metallization.

The following paragraph briefly summarizes the sources of uncertainties: the uncertainty in ε_r is dominated by the geometric properties of the capacitor. The uncertainty in the thickness d is the standard deviation of five measurements at different spots on the sample (about 0.5 %) that were taken with a Heidenhain probe. The area A is determined by image processing the sample pictures. The uncertainty is taken to be the standard deviation of different samples of same nominal area. This is a very conservative guess, which is most likely the reason for the comparatively large uncertainty. The uncertainty of Q_d is dominated by the noise in the conductance (1 % at 100 pF and 0.1 nS). The uncertainty of χ_3 is based on the uncertainty of the fit $\Delta\varepsilon_r(E)$ (about 10 %). The uncertainty of $\Delta\varepsilon_r$ is dominated by ΔC. The uncertainty ΔC is estimated from the residuals of a fit with a large number of voltage points (Figure 4.18). At a ΔC of about -4 fF, the residuals deviate by about ± 0.1 fF, corresponding to 2.5 % of the ΔC signal and 0.6 ppm of the absolute capacitance $C_0 = 180.9$ pF. The uncertainty in the electric field is dominated by the uncertainty in ε_r.

Overall, the majority of the samples agree with a bulk nonlinear susceptibility of

$$\chi_3^{1\mathrm{kHz}} = (-7.5 \pm 0.2) \times 10^{-13}\,\mathrm{m^2/V^2}.$$

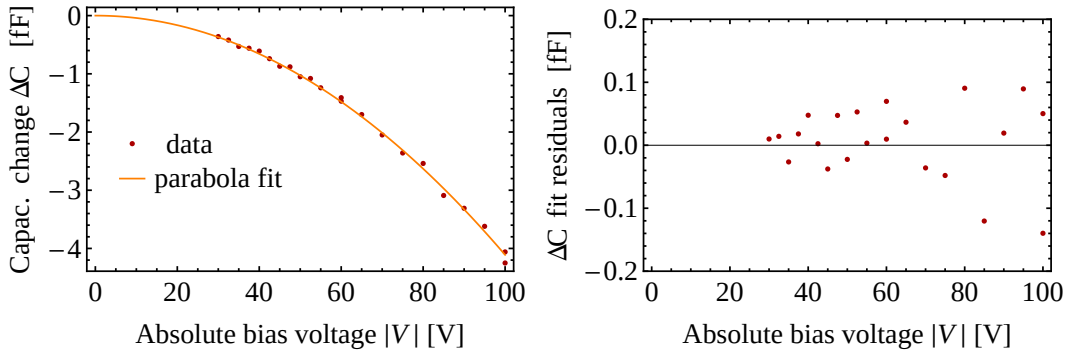

(a) Data with fit (b) Fit residuals

Figure 4.18: Voltage dependent capacitance measurement at sample #0-3. Positive and negative voltages are overlaid to give a visual comparison.

As discussed above, it seems more likely that the significant deviations are due to inhomogeneous bulk properties than influences of the interface. Still, it cannot be said with final certainty that the measured nonlinearity actually stems from the bulk material instead of the interface. For the qualitative comparison to the microwave nonlinearity from subsection 4.1.1 and for the comparison of samples of different crystallite size in subsection 4.2.2, the order of magnitude of $10^{-13}\,\mathrm{m^2/V^2}$ for all measurements is sufficient.

In contrast to the saturating intermodulation trend that was observed in the microwave measurements, the dependency of the capacitance on the voltage is perfectly described by a symmetric parabola with a single fitting parameter. Additionally, the capacitance method allows the determination of the sign of the nonlinearity in contrast to the intermodulation measurement.

As a microscopic origin, any resonant effect can directly be excluded because the DC voltage induces the nonlinear response. This also excludes the saturable absorber

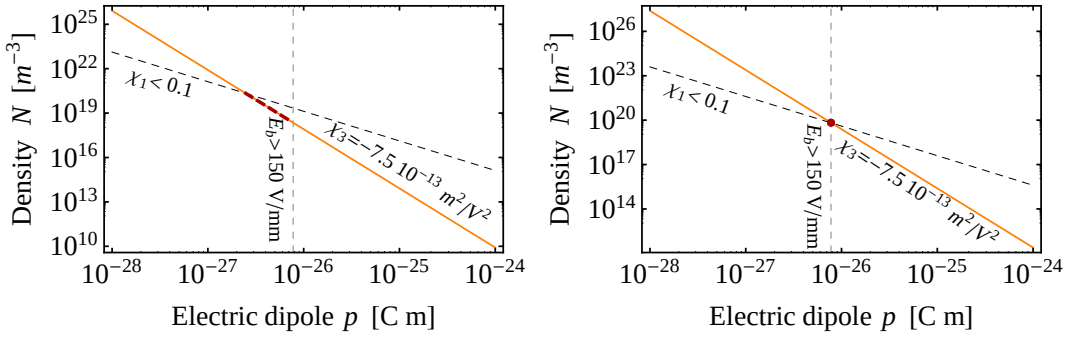

(a) Binary state system (b) Charge in a box (Langevin)

Figure 4.19: Estimation of the density N of dipoles p for the measured constraints, under the assumption of the binary state system (Equation 2.4.66) and the charge in a box model (Equation 2.4.63). The solid line represents the measured χ_3 ($N \sim p^{-4}$), the dashed lines are conditions in form of inequalities ($N \sim p^{-2}$, $p < p_{max}$).

(Equation 2.4.44). Negative nonlinear susceptibilities in MIMs have been attributed to dipolar orientation [PSW+11] or based on entropic far distance interactions [BDB09]. Additionally, both the binary state system (Equation 2.4.66) and the charge in a box model (Equation 2.4.63) can be adjusted in their parameters to result in the required order of magnitude of the nonlinear susceptibility χ_3. Furthermore, the charge in a box model is not limited by a diffusion velocity compared to the field reversal time as in the microwave range. However, χ_3 alone only allows the determination of the product of the density N and the dipole p in these models, Np^4. Nevertheless, further constrains can be derived: First, the fact that the data is perfectly described by a parabola reveals that the saturation field amplitude E_b is not reached under the experimental conditions. This minimum possible value in E_b gives an upper limit for p according to Equation 2.3.27. Second, the linear contribution of the nonlinear mechanism is expected not to exceed $\chi_1 = 0.1$, otherwise it would had been observed in dielectric spectroscopy [5]. Figure 4.19 visualizes these constrains. The value for E_b is chosen for 500 V over 100 µm, including the de-electrification field. The resulting window of possible values is rather narrow. For the charge in a box model it is even on the edge of returning any possible combination of parameters at all. For both models, the dipole can be constrained to about 10^3 atomic dipoles (eÅ) with a density of $N \approx 10^{20}\,\mathrm{m}^{-3}$.

4.2.2 $Ba_4Al_2Ti_{10}O_{27}$ Ceramization Series

The Poweramic GHz33 glass-ceramic samples of the thickness series all showed a significant nonlinear response. On the other hand, its green glass did not exhibit a measurable nonlinear response. This suggest a dependency of the nonlinear response on the degree of crystallinity of the dielectric. To further elaborate this conjecture, a sample series with different degrees of ceramization and hence degrees of crystallinity are investigated. The crystallite size shall serve as a measure of degree of crystallinity. Figure 4.22 shows four block samples with different degrees of ceramization. They are clearly distinguishable by visual inspection. Their SEM images in Figure 4.21 show the different degree of ceramization in the crystallite size, though neither sample K1 or K2 exhibit detectable crystallites.
To achieve high electric fields, the blocks were grinded down to about 160 µm. Under the pressure of polishing, the samples turned out to be fragile. Nevertheless, some

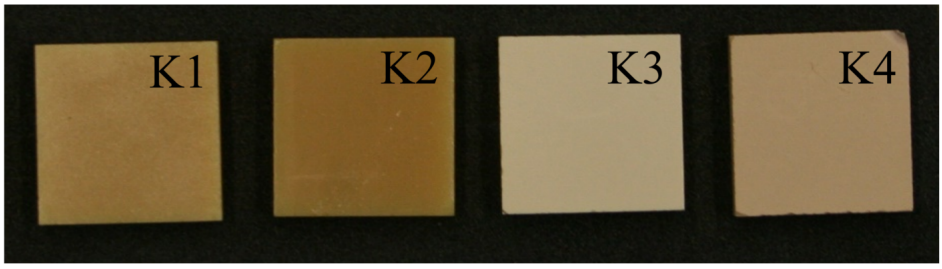

Figure 4.20: Ceramized blocks for four different ceramization programs. Their geometry is $28 \times 28 \times 5$ mm^3.

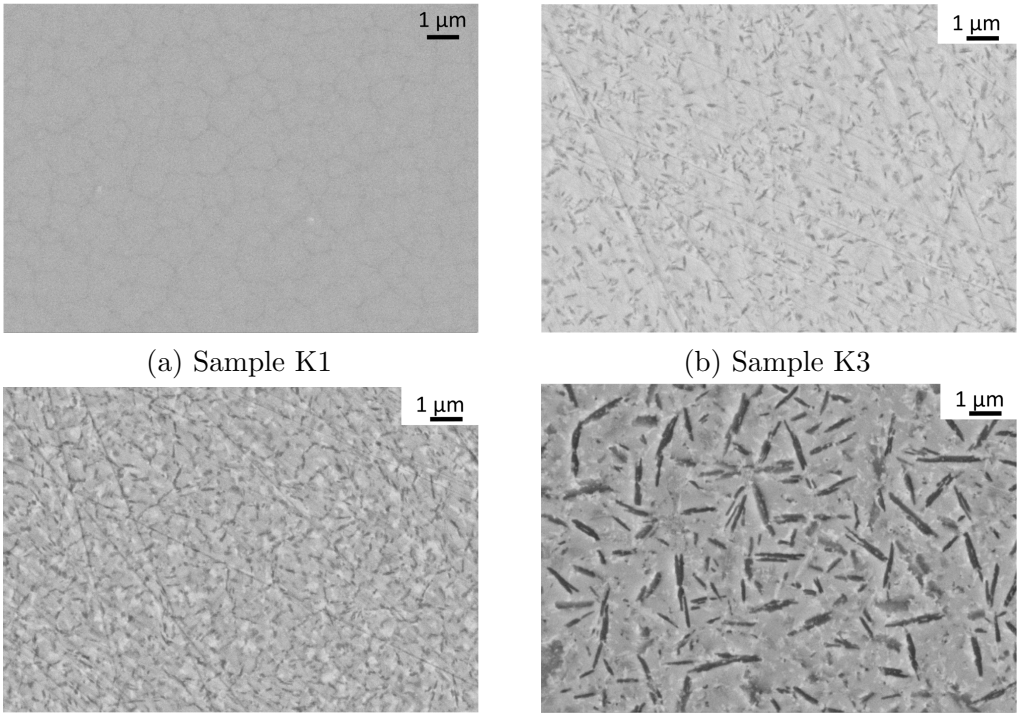

(a) Sample K1 (b) Sample K3

(c) Sample P (Production GHz33) (d) Sample K4

Figure 4.21: Scanning Electron Microscopy images for four ceramized samples with different crystallite sizes. The dark areas have been identified as $Ba_4Al_2Ti_{10}O_{27}$ via energy dispersive X-ray spectroscopy.

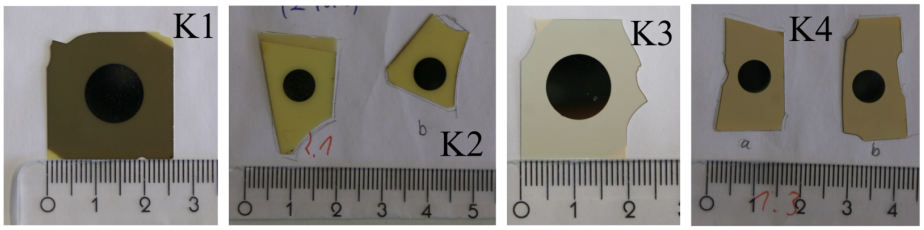

Figure 4.22: Metallized samples with different degrees of ceramization.

fragments were sufficiently large to be metallized. These selected samples are shown in Figure 4.22. Furthermore, the samples turned out to be unsuitable for cleaning in the ultrasonic bath due to their fragility. Instead, they were simply wiped with ethanol before metallization.

Figure 4.23 summarizes the linear and the nonlinear dielectric response for the different degrees of ceramization for the samples with measurable nonlinear response and measurable crystallite size. The crystallite sizes are visually estimated based on Figure 4.21 and are hence equipped with large uncertainties. The samples that do not show any measurable nonlinear response (K1 and K2) are also the samples with no detectable crystallites. Samples K3, P (GHz33 from production) and K4 on the other hand show a positive correlation of nonlinear susceptibility and crystallite size. The uncertainty of the K3 sample is larger due to the asymmetric response to negative and

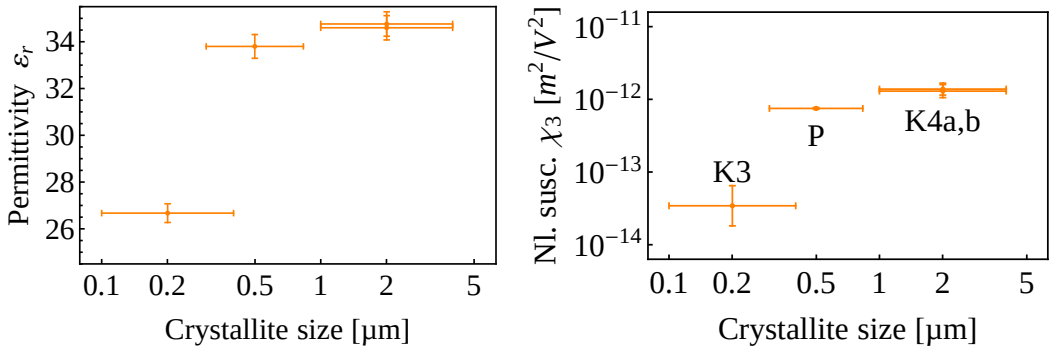

(a) Permittivity (b) Nonlinear susceptibility χ_3

Figure 4.23: Dielectric properties for different crystallite sizes. Both the linear susceptibility and the nonlinear susceptibility increase with the crystallite size. In contrast to the linear susceptibility, the nonlinear susceptibility changes over order of magnitudes. The uncertainty of the 0.2 µm sample is much larger as this sample actually exhibited a significant asymmetric response (see Figure A.11).

positive voltages (see Figure A.11), which is clearly not compatible with a bulk χ_3. As this sample shows the smallest nonlinear response, it is possible that this sample is dominated by an interface nonlinear response, while the others are dominated by a bulk nonlinear response. However, more samples are needed to support such conjectures. Overall, a correlation of the nonlinear response of MIM capacitors made from the $Ba_4Al_2Ti_{10}O_{27}$ glass-ceramic and the crystallite size has been observed. Still, this nonlinear response cannot be unambiguously attributed to a bulk χ_3.

Chapter 5

Conclusion and Outlook

The aim of this work was the characterization of the nonlinear susceptibility of dielectric glasses and glass-ceramics in the microwave range and to relate their nonlinear susceptibility to microscopic mechanisms. The coupled dielectric resonator (CDR) setup from [Ber18] was extended, including a model and a measurement procedure for the measurement setup, and tested for reproducibility. The CDR setup allows measuring nonlinear susceptibilities of high permittivity $\varepsilon_r > 30$ and low loss dielectrics $Q_d > 1000$ with a sensitivity of at least $|\chi_3| > 10^{-17}\,\mathrm{m^2/V^2}$.

A glass-ceramic with $Ba_4Al_2Ti_{10}O_{27}$ as its main crystalline phase was characterized. The nonlinear susceptibility of the glass-ceramic was found to be $|\chi_3^{1\mathrm{GHz}}| = (4 \pm 2) \times 10^{-16}\,\mathrm{m^2/V^2}$, which is comparable to previously measured high quality sintered ceramics.

The dependency of the intermodulation level on the input power observed in this measurement was found to be incompatible with a power-law description classically used for phenomenological description of small nonlinearities. To describe the intermodulation response, a method based on Fourier coefficients was developed to predict intermodulation for more general nonlinear responses: while the power-law description is only applicable within the radius of convergence of the power series, the Fourier coefficient integral allows numerical calculation of intermodulation responses of any square integrable nonlinear response function.

The Fourier coefficient integral method was applied to several established nonlinear polarization models: amongst these, the locally free charge model, the resonant saturable absorber and the binary state system were found to exhibit precisely the intermodulation behavior that was observed experimentally.

On this basis, microscopic realizations of these models were discussed. In this context, it was found that microscopic interpretation crucially depends on local electric field models. The locally free charge model results in lengths that coincide with the size of the crystallites in the glass-ceramic. The binary state system on the other hand could stem from a local ferroelectric behavior. A definite determination of model is not possible, however, several previous conjectures could be ruled out. In any case, the mechanism that dominates the nonlinear response was found to contribute barely to

the linear dielectric properties ($\chi_1 = 10^{-8}$) and therefore cannot be detected by linear dielectric spectroscopy measurements.
The CDR setup was extended to coupled *split* dielectric resonators (CsDR), allowing the characterization of dielectrics with lower permittivity. This enabled measuring the $\varepsilon_r = 21$ glass N-SF66. The glass was used to investigate the influence of typical mineral impurities. Iron doping was found to have no measurable influence on the nonlinear dielectric response, which was originally suspected to exhibit a magnetic nonlinear response. The absence of measurable changes was further supported by modeling the nonlinear response of magnetic impurities. Instead, SiO_2 immiscibilities were found to increase the nonlinear response of the glass significantly, which supports the discussed microscopic origins related to inhomogeneity.
For comparison, the nonlinear dielectric response was measured in the kHz range in a capacitor geometry with an ultra-high precision capacitance bridge. Several glassy samples were found to show no measurable nonlinear response ($|\chi_3| < 10^{-14}\,\mathrm{m^2/V^2}$). The $Ba_4Al_2Ti_{10}O_{27}$ glass-ceramic, on the other hand, showed a significant negative nonlinear response. The majority of the samples conformed to $\chi_3 = (-7.5 \pm 0.2) \times 10^{-13}\,\mathrm{m^2/V^2}$. Finally, the nonlinear response of the capacitor could be shown to increase with the crystallite size in the glass-ceramic.
In summary, the SiO_2 immiscibility and the crystallite size dependency point towards an inhomogeneous source of the nonlinearity at microwave frequencies and below, in contrast to previous homogeneous conjectures such as phonon nonlinearity and electrostriction.

Outlook

First, the characterization of the ceramization series that was characterized with the kHz capacitance bridge motivates a similar series for the CDR setup. The SiO_2 immiscibilities were already shown to enhance the microwave nonlinear response. Both the crystalline phase or its interface are a potential candidate for the nonlinear microwave response of the glass-ceramic.
The ε_r-range of the CDR/CsDR setup could be extended even further by a tuning gadget for the resonators. Nevertheless, the applicability was found to be limited. Moreover, it is advisable to compare the outcomes to results obtained with different methods. For instance, the re-entrant cavity method developed in [VH88] has sufficient sensitivity and seems to be extendable for the characterization of solid dielectrics. It allows nonlinear dielectric characterization up to the microwave range, although with a quasi-static bias field that induces the nonlinear response.
For characterization of kHz nonlinear responses, metal-isolator-metal (MIM) structures with thin dielectric films $\sim 10\,\mathrm{nm}$ and high electric fields show an easily measurable change in capacitance. While MIM capacitors are bottom-up manufactured, a resonant circuit setup comparable to the one used in [FFK+93] seems more suitable for top-down manufactured samples. It allows the detection of smaller changes in the dielectric

constant at lower fields.
Moreover, the discussion on local electric field models motivates to identify nonlinear mechanisms in a different manner than the applied electric field, e.g. by temperature and frequency dependent measurements. Especially higher frequencies are of technological interest, as applications further proceed to tens of GHz, including automotive systems. In addition, as the power range for observing the intermodulation is limited, higher powers can be addressed with the aim to differentiate various intermodulation trends. Finally, the proposed Fourier coefficient integral method seems to be applicable in various different fields of science that use intermodulation measurements for nonlinear characterization. For instance, so far unexplained intermodulation trends in high temperature superconductors, microstrip lines, and even intermodulation in the mammalian ear can be accurately modeled with this method based on the well-known nonlinear response functions. Figure 5.1 gives three examples. Based on this model, new insights into nonlinear responses may become possible.

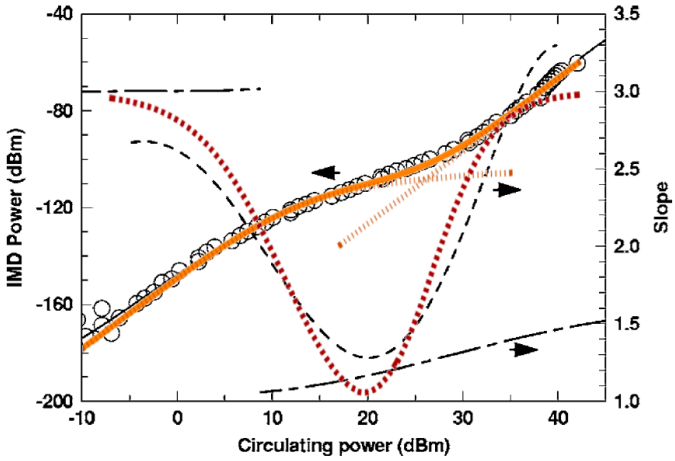

(a) High Temperature Superconductors [AO05]

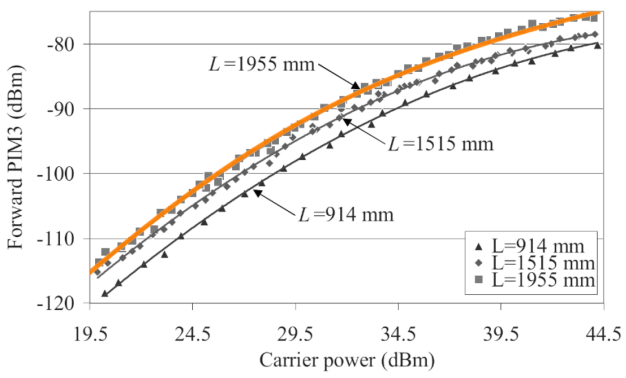

(b) Microstrip lines [SZS09]

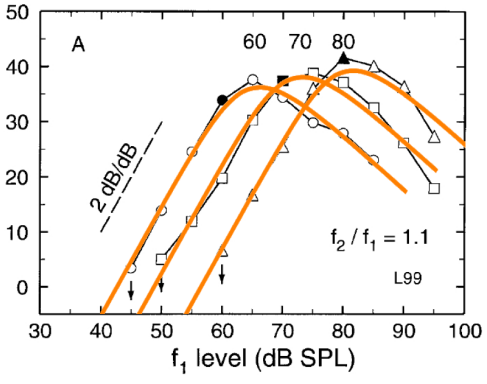

(c) Mammalian ear [RRR97]

Figure 5.1: Examples for intermodulation data that can be explained with the proposed Fourier coefficient integral for intermodulation prediction. In all cases, the underlying model is the saturable absorber, though other models produce similar trends. In [RRR97], one input tone is held constant in power, which gives rise to the 2 dB/dB slope. In [AO05], both the actual intermodulation level and its derivative are shown.

Appendix

Additional Calculations

Potential Estimate

The potential in [MF62] is given in the form:

$$\begin{aligned} r_0 &= 3.472 \times 10^{-8}\,\mathrm{cm} \\ \Phi(r_0) &= 0 \\ \Phi'(r_0) &= 0 \\ \Phi''(r_0) &= 1.819 \times 10^{4}\,\mathrm{erg/cm^2} \\ \Phi'''(r_0) &= -9.693 \times 10^{12}\,\mathrm{erg/cm^3} \\ \Phi''''(r_0) &= 4.016 \times 10^{21}\,\mathrm{erg/cm^4} \end{aligned} \tag{A.0.1}$$

This formulation shall be translated into a potential of the form:

$$\Phi(r) = \Phi_0 r + \Phi_1 r^2 + \Phi_2 r^3 + \Phi_3 r^4 \tag{A.0.2}$$

This translation occurs with:

$$\begin{aligned} \Phi_3 &= \Phi''''(r_0)/24 \\ \Phi_2 &= \Phi'''(r_0)/6 - \Phi''''(r_0)\ r_0/6 \\ \Phi_1 &= \Phi''(r_0)/2 - \Phi'''(r_0)\ r_0 + \Phi''''(r_0) r_0^2/4 \\ \Phi_0 &= -\Phi''(r_0) + \Phi'''(r_0) r_0^2/2 - \Phi''''(r_0) r_0^3/6 \end{aligned} \tag{A.0.3}$$

This leads to

$$\begin{aligned} \Phi(r - r_0) = {} & 9.10 \times 10^{3}\,\mathrm{erg/cm^2}(r - r_0)^2 \\ & - 1.62 \times 10^{12}\,\mathrm{erg/cm^3}(r - r_0)^3 \\ & + 1.67 \times 10^{20}\,\mathrm{erg/cm^4}(r - r_0)^4 \end{aligned} \tag{A.0.4}$$

Circuit Modeling

The circuit depicted in Figure 3.11 can be modeled by two coupled differential equations:

$$\begin{aligned} L_c\ \ddot{H} + L_\mathrm{I}\ \ddot{I} + R\ \dot{I} + \frac{1}{C}\ I = 0 \\ L_c\dot{I} + L_\mathrm{H}\dot{H} = U_\mathrm{H} \end{aligned} \tag{A.0.5}$$

Solving the latter equation after differentiating once returns $\ddot{H} = (U_\mathrm{H} - L_c\ddot{I})/L_\mathrm{H}$. Inserting this into the former equation of Equation A.0.5 after dividing by L_I and replacing $2\gamma = R/L_\mathrm{I}$ and $\omega_0^2 = 1/(L_\mathrm{I}C)$ gives:

$$\left(1 - \frac{L_c^2}{L_\mathrm{H}L_\mathrm{I}}\right)\ddot{I} + 2\gamma\dot{I} + \omega_0^2 I = -\frac{L_c}{L_\mathrm{H}L_\mathrm{I}}\ \dot{U}_\mathrm{H} \tag{A.0.6}$$

This equation can be simplified by introducing the dimensionless coupling factor $k = L_c/(L_\mathrm{H}L_\mathrm{I})$. Remembering the physical meaning of L_c, L_H and L_I leads to the constrains $L_\mathrm{H} > L_c < L_\mathrm{I}$ and hence $k < 1$. Dividing Equation A.0.6 by $1 - k^2$ leads to:

$$\ddot{I} + 2\frac{\gamma}{1-k^2}\dot{I} + \frac{\omega_0^2}{1-k^2}I = \frac{k}{1-k^2}\ \frac{-\dot{U}_\mathrm{H}}{\sqrt{L_\mathrm{H}L_\mathrm{I}}} \tag{A.0.7}$$

This is just the differential equation of a damped and excited harmonic oscillator with modified resonance frequency and damping and excitation A:

$$\gamma' = \frac{\gamma}{1-k^2} > \gamma \text{ and } \omega_0' = \frac{\omega_0}{\sqrt{1-k^2}} > \omega_0 \text{ and } A = \frac{k}{1-k^2}\ \frac{-\dot{U}_\mathrm{H}}{\sqrt{L_\mathrm{H}L_\mathrm{I}}} \tag{A.0.8}$$

Effect of Unequal Coupling on Amplitudes

For unequal coupling c and k, the system of three coupled resonators is described by:

$$\begin{pmatrix} \omega_0^2 - \omega^2 & -k\omega_0^2 & 0 \\ -k\omega_0^2 & \omega_0^2 - \omega^2 & -c\omega_0^2 \\ 0 & -c\omega_0^2 & \omega_0^2 - \omega^2 \end{pmatrix} \begin{pmatrix} I \\ J \\ K \end{pmatrix} = \mathbf{0} \tag{A.0.9}$$

The eigenvalues for ω^2 are:

$$\begin{aligned} \omega_1 &= \omega_0\sqrt{1 - \sqrt{c^2 + k^2}} \\ \omega_2 &= \omega_0 \\ \omega_3 &= \omega_0\sqrt{1 + \sqrt{c^2 + k^2}} \end{aligned} \tag{A.0.10}$$

This shows that unequal coupling $k \neq c$ does not influence the intermodulation relation $\omega_3 = 2\omega_2 - \omega_1$. The corresponding eigenvectors $\mathbf{v} = (I, J, K)$ read:

$$\begin{aligned} \mathbf{v}_1 &= (c, \sqrt{c^2 + k^2}, k) \\ \mathbf{v}_2 &= (k, 0, -c) \\ \mathbf{v}_3 &= (1, -\sqrt{c^2 + k^2}, 1) \end{aligned} \tag{A.0.11}$$

Estimation for χ_3 Benchmark

For non-resonant structures, [Sta80] offers a calculation to estimate the influence of a nonlinear substrate on PIM generation in a microstrip line. The intermodulation power is derived to be:

$$P_{\mathrm{IM3}} = \frac{\pi^2}{4} Z_0^2 P^3 \alpha_{\mathrm{V}}^2 \left(\frac{Y}{\lambda_{\mathrm{IM}}} \right)^2 \tag{A.0.12}$$

Here, α_{V} is defined by $\varepsilon_r(V) = \varepsilon_r(1 + \alpha_{\mathrm{V}} V^2)$ so $\alpha_{\mathrm{V}} = (\varepsilon_r\ d)^2 \alpha_{\mathrm{E}}$ and $\alpha_{\mathrm{E}} = \chi_3/\varepsilon_r$ Choosing $Z_0 = 50\,\Omega$, an input power of $P = 43\,\mathrm{dBm}$ in a substrate of $\varepsilon_r = 5$ of thickness $\mathrm{d} = 1\,\mathrm{mm}$ over a length of $Y = 10\,\mathrm{cm}$ at $1\,\mathrm{GHz}$ yields $|\chi_3| < 10^{-15}\,\mathrm{m^2/V^2}$ if the intermodulation power was restricted to $P_{\mathrm{IM3}} < -112\,\mathrm{dBm}$. The powers P and P_{IM3} were chosen to fulfill the limit given in [HCC09a].
For resonant structures, the authors of [ITNW92] proposed a filter based on their high quality (Zr,Sn)$\mathrm{TiO_4}$ sintered ceramic that achieves 50 dB isolation. This suggest a stricter limit on the material nonlinearity for resonant structures $|\chi_3| < 10^{-17}\,\mathrm{m^2/V^2}$ (see Figure 4.5).

Calculation of the RoC for the inverse polynomial

The radius of convergence (RoC) of the power series of the functions of interest, $\mathrm{Lgv}(x) = \coth(x) - 1/x$, $\tanh(x)$ and $x/\sqrt{1+x^2}$ are given in [Zuc72] and [Boy08]. For $y(x)$ defined by $x = y(x) + y(x)^3$ (see Equation 2.3.21), the radius of convergence is discussed here. The radius of convergence can be obtained with the follwing *Mathematica* code:

```
Solve[x == y + y^3, y]; (*Solve inverse polynomial equation*)
y/.%[[1]](*Take real solution only*);
Normal[Series[%,{x,0,15}]] (*Calculate series at x=0 up to the 15th order*);
CoefficientList[%,x] (*Take Coefficients*);
%[[2;; ;;2]] (*Take odd terms only*);
a[n_] = FindSequenceFunction[%,n] (*Recognize pattern of coefficients*);
b[n_]:= If[EvenQ[n], 0, a[(n+1)/2]] (*Reconstruct even terms*);
1/Limit[Abs[b[n]]^(1/n), n->Infinity] (*Calculate RoC*)
```

15 terms in the power series are sufficient to recognize the pattern of the coefficients. The output is

$$x_{\mathrm{RoC}} = 2/(3\sqrt{3}) = -4.1\,\mathrm{dB}. \tag{A.0.13}$$

This method can also be applied to the saturable absorber in Equation 2.4.44 and conforms to the RoC given in [Boy08].

Additional Experimental Data

CsDR Samples

(a) Laboratory sample (L) (b) Production sample (P) (c) GHz33 green glass (GG)

Figure A.2: Disc samples (thickness 4 mm, outer diameter 60 mm)

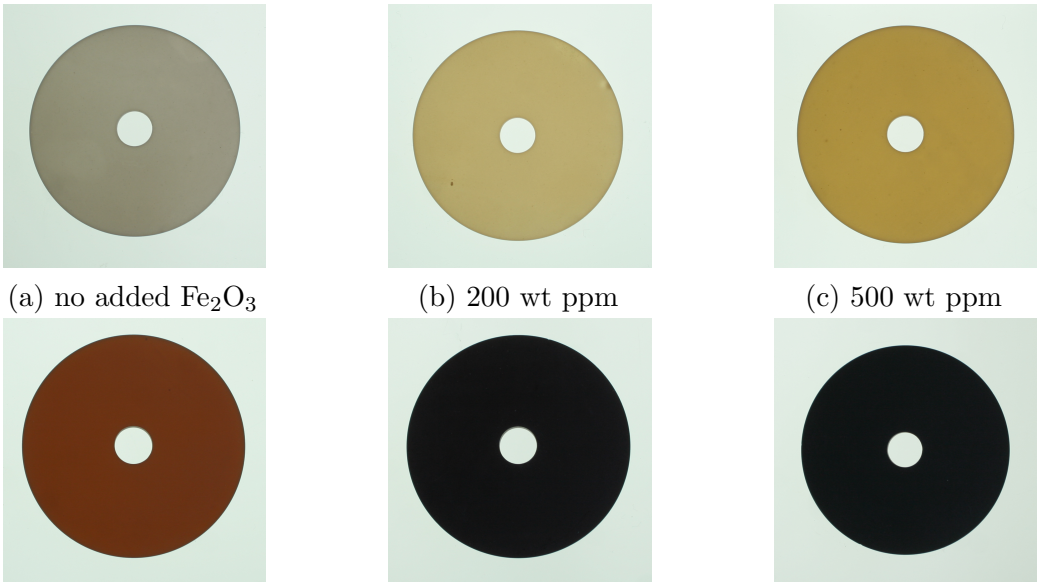

(a) no added Fe_2O_3 (b) 200 wt ppm (c) 500 wt ppm

(d) 2000 wt ppm (e) 10000 wt ppm (f) 20000 wt ppm

Figure A.3: N-SF66 dopant series Fe_2O_3.

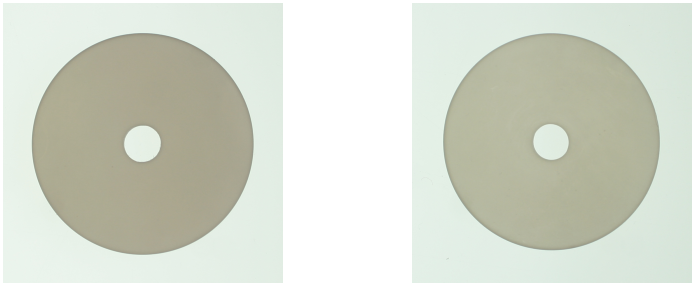

(a) 1000 wt ppm (b) 10000 wt ppm

Figure A.4: N-SF66 dopant series NaO.

	Q0	f2(MHz)	S22f2	S22p	F3nwa	F3spc	F2spc	F1spc	f1soll	f1ist
1	1870	950.7	-22.9	-1.	-1.	-3.7	-87	-116	917.9	917.
2	1870	951.1	-22.7	-1.	-1.	-3.5	-87	-114	918.	918.1
3	1870	950.15	-16.7	-1.	-1.	-3.7	-88	-116	917.3	917.65
4	1870	950.1	-15.6	-0.9	-1.	-3.6	-88	-115	917.4	917.7
5	1870	951.	-20.2	-0.9	-1.	-3.6	-84.7	-113	921.	920.
6	1870	950	-18.9	-0.9	-1.	-3.7	-85	-112	920.75	920.
7	1870	950.7	-16.3	-1.1	-1.	-3.9	-88.3	-116	917.7	917.2
8	1870	950.75	-15.5	-1.	-1.	-3.8	-89	-114	917.5	916.9
9	1870	950.2	-12.6	-1.	-1.	-4.	-87	-115	918.	918.4
10	1870	950.2	-11.6	-0.9	-1.	-4.2	-87	-114	918.5	918.7
11	1870	950.2	-11.6	-1.	-1.	-4.	-86.6	-115	918.2	918.4
12	1785	950.4	-11.8	-1.1	-1.	-4.2	-86.15	-115	918.5	918.5
13	1870	950.25	-12.1	-1.	-1.	-4.	-86.6	-115	918.2	918.3

(a) Settings GHz33

	split(MHz)	miss(MHz)	P2in(dBm)	P1out(dBm)	P2out(dBm)	P3out(dBm)	IM3M(dB)	E2(V/mm)	chi3(m2/V2E-16)	E2b(V/mm)
1	32.8	0.9	-20.	-0.3	-3.1	-145.2	-144.9	2.09	4.45	16.4
2	33.1	-0.1	-20.	12.8	-13.2	-138.1	-150.9	2.09	2.24	14.5
3	32.85	-0.35	-20.	14.3	1.4	-134.3	-148.6	2.15	2.77	15.2
4	32.7	-0.3	-20.	10.1	-2.	-130.9	-141.	2.16	6.6	13.9
5	30.	1.	-20.	2.7	-1.8	-138.8	-141.5	2.11	6.48	15.5
6	29.25	0.75	-20.	13.5	1.3	-137.3	-150.8	2.13	2.19	14.6
7	33.	0.5	-20.	6.9	-17.9	-137.5	-144.5	2.15	4.43	18.1
8	33.25	0.6	-20.	0.5	-10.5	-139.3	-139.8	2.16	7.55	20.3
9	32.2	-0.4	-20.	17.4	-1.	-132.8	-150.2	2.19	2.23	17.5
10	31.7	-0.2	-20.	11.8	-4.3	-136.	-147.7	2.2	2.93	16.3
11	32.	-0.2	-20.	11.1	-20.6	-136.5	-147.6	2.2	2.96	15.5
12	31.9	0	-20.	20.3	-10.7	-137.6	-157.9	2.14	1.	18.3
13	32.05	-0.1	-20.	17.5	-9.1	-137.6	-155.1	2.19	1.26	16.7

(b) Results GHz33

	Q0	f2(MHz)	S22f2	S22p	F3nwa	F3spc	F2spc	F1spc	f1soll	f2ist
1	1238	942.7	-9.6	-0.9	-1.	-3.8	-84	-111	911.5	912.3
2	1238	942.8	-9.8	-0.9	-1.	-3.8	-84	-111	913.5	914.3
3	1238	943.3	-10.7	-0.8	-0.9	-3.8	-83	-110	914.05	913.9
4	1238	942.5	-10.8	-0.8	-1.	-3.9	-82	-108	915.5	914.9
5	1230	943.	-9.8	-1.1	-1.	-4.	-85.5	-112	912.6	912.5
6	1240	943.1	-9.9	-1.1	-1.	-4.	-85.5	-112	911.8	911.9
7	1250	942.9	-7.4	-1.1	-1.	-3.9	-84.2	-112	913.9	914.3
8	1250	942.6	-6.9	-1.	-1.	-3.9	-84.2	-112	913.7	914.6
9	1250	942.75	-7.4	-1.	-1.	-3.9	-84.2	-112	914.	914.8
10	1250	942.6	-7.2	-1.	-1.	-3.9	-84.2	-112	913.6	914.35
11	1250	942.55	-7.1	-1.	-1.	-3.9	-84.2	-112	914.1	914.9
12	1250	942.8	-7.4	-1.	-1.	-3.9	-84.2	-112	913.95	914.6

(c) Settings streak samples (E)

	split(MHz)	miss(MHz)	P2in(dBm)	P1out(dBm)	P2out(dBm)	P3out(dBm)	IM3M(dB)	E2(V/mm)	z1(m2/V2E-16)	E2b(V/mm)	z2
1	31.2	-0.8	-20.	5.1	-4.6	-132.7	-137.8	1.77	102.19	14.7	4.34
2	29.3	-0.8	-20.	0.3	-7.5	-131.3	-131.6	1.77	208.21	14.4	4.34
3	29.25	0.15	-20.	7.9	-11.3	-124.1	-132.	1.77	198.54	15.7	4.34
4	27.	0.6	-20.	9.6	-9.	-132.8	-142.4	1.77	59.87	13.4	4.34
5	30.4	0.1	-20.	7.9	-8.6	-131.4	-139.4	1.76	85.96	19.6	4.34
6	31.3	-0.1	-20.	8.7	-11.7	-127.1	-135.8	1.77	127.8	16.3	4.34
7	29.	-0.4	-20.	6.7	-9.9	-132.7	-139.4	1.74	86.33	22.8	4.34
8	28.9	-0.9	-20.	-1.5	-11.	-134.6	-133.1	1.73	181.27	22.4	4.34
9	28.75	-0.8	-20.	-3.6	-12.1	-136.2	-132.6	1.75	188.01	24.	4.34
10	29.	-0.75	-20.	6.9	-14.8	-140.6	-147.6	1.74	33.92	23.4	4.34
11	28.45	-0.8	-20.	14.4	-16.3	-137.7	-152.1	1.74	20.22	21.5	4.34
12	28.85	-0.65	-20.	7.	-20.	-138.8	-145.8	1.75	41.14	21.7	4.34

(d) Results streak samples (E)

Figure A.5: Settings and resulting measurands of the CDR/CsDR measurements for GHz33 and the streak samples (E). z1 and z2 columns correspond to ζ_1 and ζ_2 in Equation 3.5.18.

SPDR Linear Dielectric Characterization

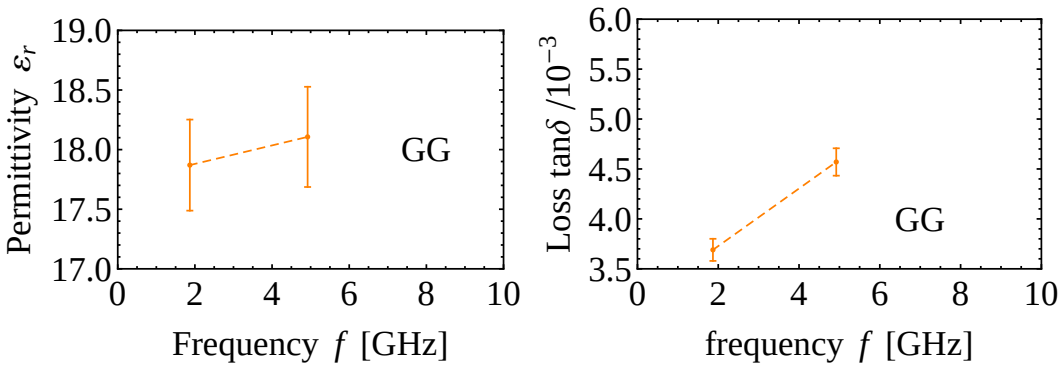

(a) Permittivity (b) loss

Figure A.6: Poweramic GHz33 green glass.

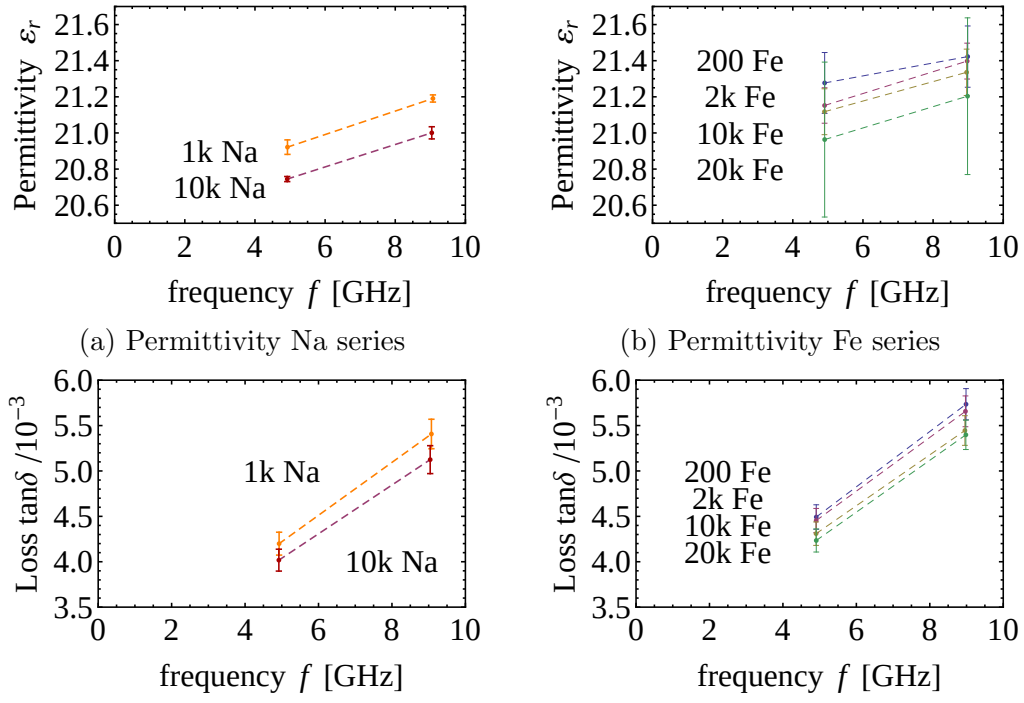

(a) Permittivity Na series (b) Permittivity Fe series

(c) Loss Na series (d) Loss Na series

Figure A.7: SPDR of Na and Fe series. The uncertainty in ε_r for the Fe series is the uncertainty of the setup while the uncertainty in the Na series is based on the standard deviation of several samples and is therefore smaller than that of the Fe measurements.

Capacitance Bridge Samples

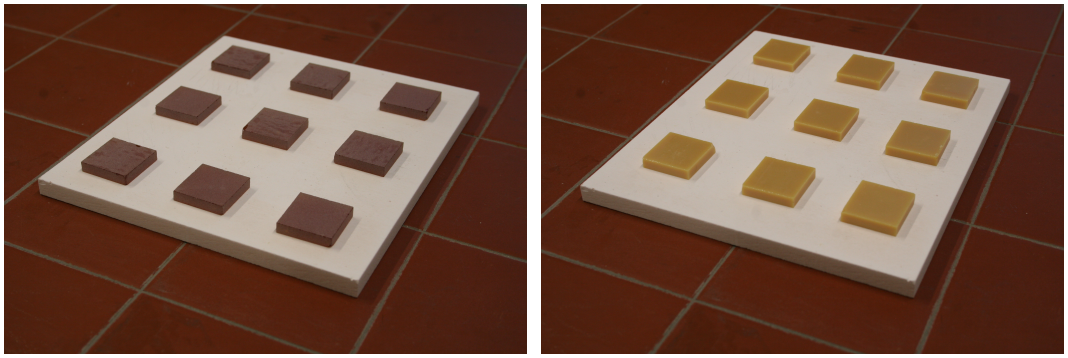

(a) Before (b) After

Figure A.8: GHz33 green glass block samples before and after the ceramization.

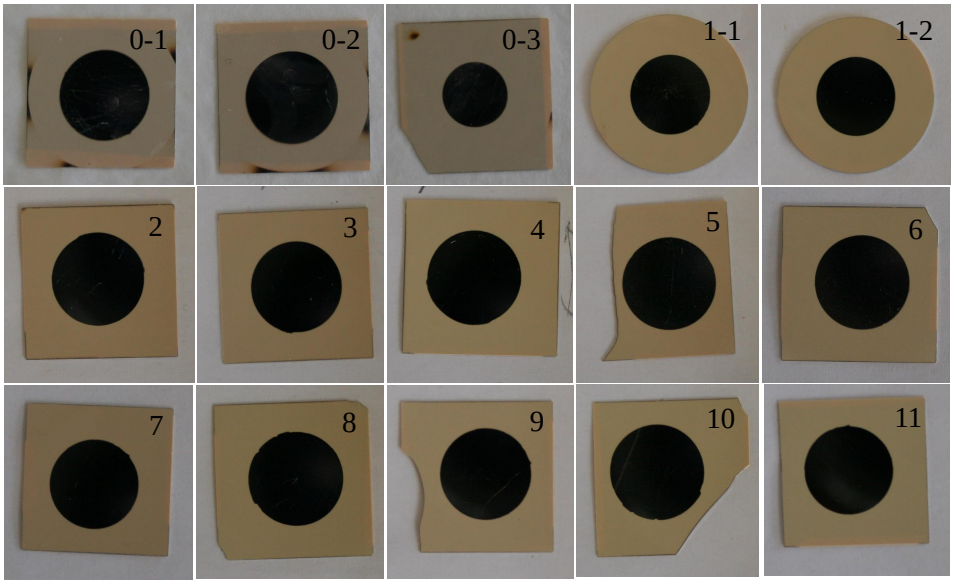

Figure A.9: High sensitivity capacitance bridge GHz33 Samples.

Table A.1: GHz33 thickness series samples. “277E” and the like denote the production batch.

Sample #	0-1	0-2	0-3
Material	GHz33 (277E)	GHz33 (277E)	GHz33 (277E)
d [µm]	98.7±0.3	99.0±0.2	100.7±0.5
A [cm^2]	1.19±0.01	1.20±0.01	0.59±0.01

Sample #	2	3	4
Material	GHz33 (304M)	GHz33 (304M)	GHz33 (304M)
d [µm]	215.9±0.6	218.2±0.8	215.0±0.9
A [cm^2]	1.19±0.01	1.17±0.01	1.19±0.01

Sample #	5	6	7
Material	GHz33 (304M)	GHz33 (304M)	GHz33 (304M)
d [µm]	185.3±0.5	184.5±0.3	158.8±0.2
A [cm^2]	1.17±0.01	1.19±0.01	1.18±0.01

Sample #	8	9	10
Material	GHz33 (304M)	GHz33 (304M)	GHz33 (304M)
d [µm]	153.8±0.7	151.5±0.9	135.8±0.6
A [cm^2]	1.18±0.01	1.15±0.01	1.19±0.01

Sample #	11	1-1	1-2
Material	GHz33 (304M)	GHz33 (277E)	GHz33 (277E)
d [µm]	138.8±0.2	248.0±2.5	251.1±0.5
A [cm^2]	1.18±0.01	1.15±0.01	1.16±0.01

Table A.2: GHz33 ceramization series samples.

Sample #	K1	K2a	K2b
Material	GHz33-K1	GHz33-K2	GHz33-K2
d [µm]	145±1	146.0±0.8	153.1±0.4
A [cm^2]	1.19±0.01	0.40±0.01	0.40±0.01

Sample #	K3	K4a	K4b
Material	GHz33-K3	GHz33-K4	GHz33-K4
d [µm]	154±1	156.0±0.4	153.9±0.8
A [cm^2]	1.13±0.01	0.39±0.01	0.39±0.01

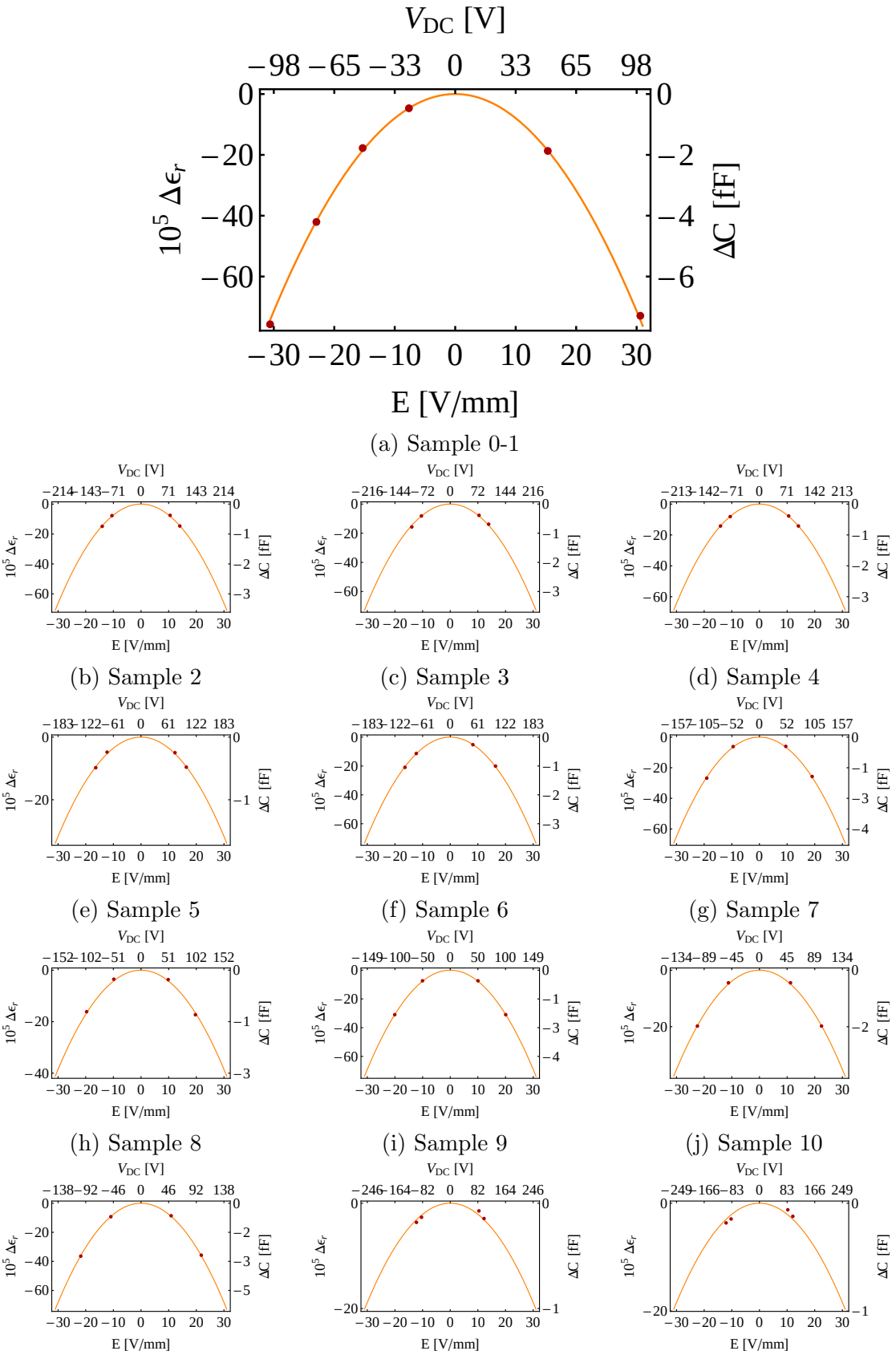

(a) Sample 0-1

(b) Sample 2 (c) Sample 3 (d) Sample 4

(e) Sample 5 (f) Sample 6 (g) Sample 7

(h) Sample 8 (i) Sample 9 (j) Sample 10

(k) Sample 11 (l) Sample 1-1 (m) Sample 1-2

Figure A.10: Change of capacitance with respect to the applied voltage for the thickness series.

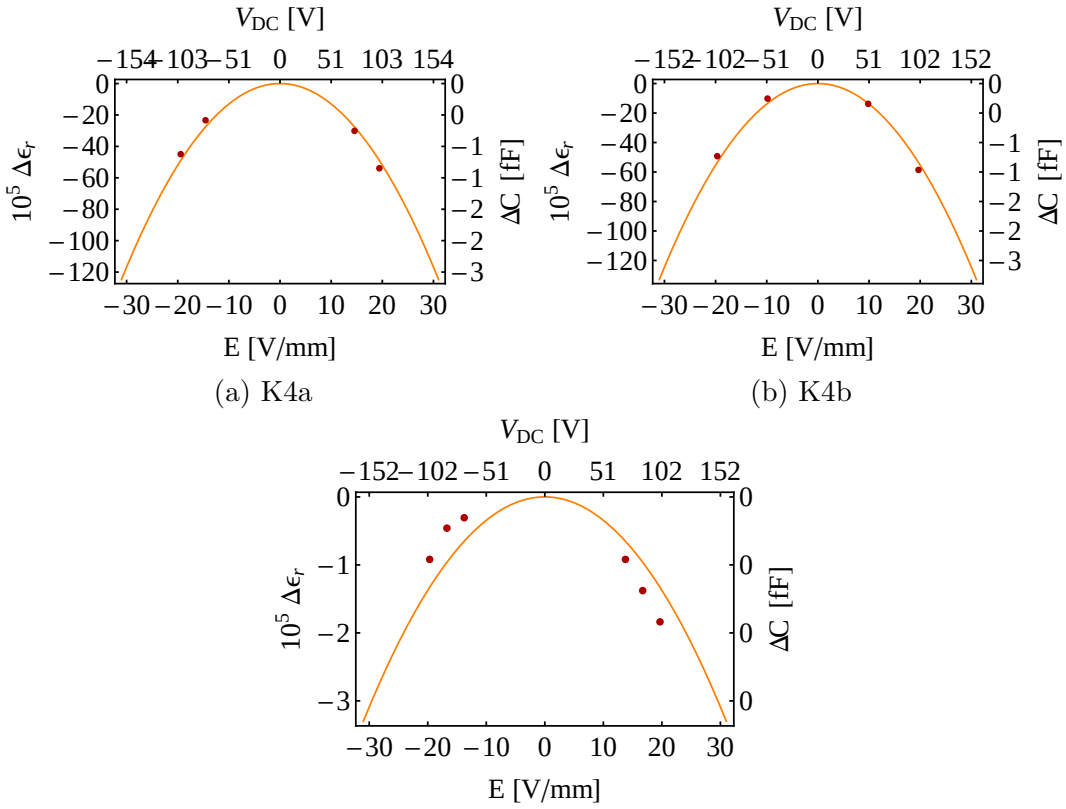

(a) K4a (b) K4b

(c) K3

Figure A.11: Change of capacitance with respect to the applied voltage for the ceramization series.

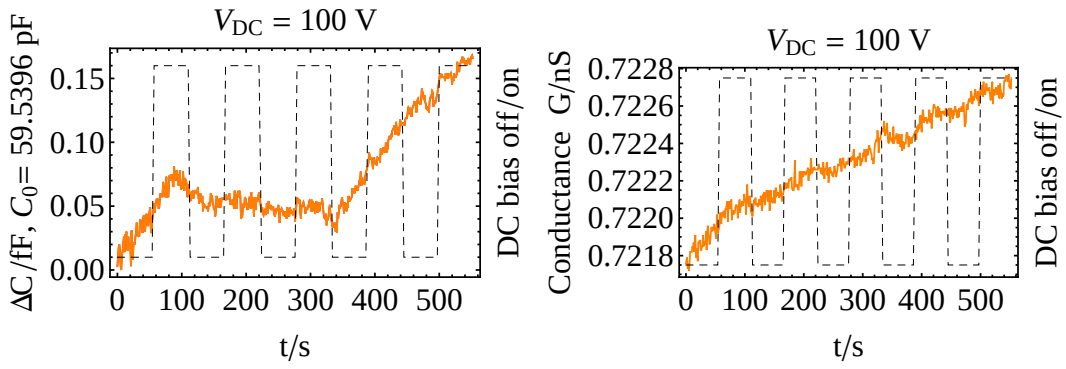

(a) time series of capacitance (b) time series of conductance

Figure A.12: Time series of sample K2a at 100 V. The dotted line marks the times with applied DC bias voltage.

Publications and Conferences

Publications

- [5] Article: M. Letz, M. Hovhannisyan, F. Bergmann, Xiaofei Bai, H. Engelmann, and G. Weidmann, "$Ba_4Al_2Ti_{10}O_{27}$ based glass ceramic as dielectric in high frequency applications", *Applied Physics Letters* 119, 052903 (2021)

- [4] Article: F. Bergmann, M. Letz, H. Maune, and G. Jakob, "Description of intermodulation generation of nonlinear responses beyond the validity of the power series expansion", *Applied Physics Letters* 118, 012902 (2021)

- [3] Patent: F. Bergmann, M. Letz, "Device and method for determining the nonlinearity of a dielectric material", *Publication No.* WO 2020/127199 A1 (2020)

- [2] Conference Proceeding: F. Bergmann, M. Letz, H. Maune, and G. Jakob, "Setup for Characterization of the Non-Linear Electric Susceptibility in the Microwave Range Applied to a Glass Ceramic" in 2019 IEEE MTT-S International Microwave Workshop Series on Advanced Materials and Processes for RF and THz Applications (IMWS-AMP), pp. 16–18 (2019)

- [1] Article: F. Bergmann, M. Letz, H. Maune, and G. Jakob, "High sensitivity characterization of the nonlinear electric susceptibility of a glass ceramic in the microwave range", *Applied Physics Letters* 114, 212903 (2019)

Conferences

- Contributed talk: "High sensitivity characterization of the nonlinear electric susceptibility of glasses and glass-ceramics in the microwave range", Electroceramics XVII, Darmstadt (online), Germany, Aug. 24-28 (2020)

- Invited talk: "High sensitivity characterization of the nonlinear electric susceptibility of glasses and glass ceramics in the microwave range" , Advanced Ceramic and Application Conference VIII, Belgrade, Serbia, Sep. 23-25 (2019)

- Contributed talk: "Nonlinear dielectric responses in the microwave range", IEEE MTT-S International Microwave Workshop Series on Advanced Materials and Processes, Bochum, Germany, Jul. 16-18 (2019)

- Poster: "Glasses and glass ceramics in wireless communication applications: Nonlinear dielectric response", SCHOTT Materials Day, Mainz, Germany, Jun. 4 (2019)

- Contributed talk: "Tiny nonlinear dielectric responses in the microwave range", DPG Frühjahrstagung, Regensburg, Germany, Mar. 31 - Apr. 5 (2019)

- Contributed talk: "Characterization of extremely small nonlinearities in the dielectric response of glass-ceramics in the microwave range", Electronic Materials and Applications, Conference, Orlando, Florida, USA, Jan. 23-25 (2019)

Bibliography

[ACP87] R Adair, L L Chase, and S A Payne. Nonlinear refractive-index measurements of glasses using three-wave frequency mixing. *Journal of the Optical Society of America B*, 4(6):875–881, 1987.

[AH02] Andeen-Hagerling. AH2550A 1 kHz Ultra-Precision Capacitance Bridge. Manual, 2002.

[AHHC17] D Z Austin, K E K Holden, J Hinz, and J F Conley. Electrode modulated capacitance-electric field nonlinearity in metal-insulator-metal capacitors. *Applied Physics Letters*, 110(26):263503, 2017.

[AO05] D Agassi and D E Oates. Nonlinear Meissner effect in a high-temperature superconductor. *Physical Review B*, 72:014538, 2005.

[AOK19] A Aubret, M Orrit, and F Kulzer. Understanding Local-Field Correction Factors in the Framework of the Onsager-Böttcher Model. *ChemPhysChem*, 20(3):345–355, 2019.

[Bö73] C J F Böttcher. *Non-linear Effects*. Theory of Electric Polarization. Elsevier, 1973.

[BCA06] S Bécu, S Crémer, and J-L Autran. Microscopic model for dielectric constant in metal-insulator-metal capacitors with high-permittivity metallic oxides. *Applied Physics Letters*, 88(5):052902, 2006.

[BCD18] J Ballato, M Cavillon, and P Dragic. A unified materials approach to mitigating optical nonlinearities in optical fiber. I. Thermodynamics of optical scattering. *International Journal of Applied Glass Science*, 9(2):263–277, 2018.

[BDB09] S Blonkowski, E Defay, and X Biquard. Sign of the nonlinear dielectric susceptibility of amorphous and crystalline $SrTiO_3$ films. *Physical Review B*, 79:104108, 2009.

[Ben33] W R Bennett. New results in the calculation of modulation products. *The Bell System Technical Journal*, 12(2):228–243, 1933.

[Ber18] F Bergmann. Measuring extremely small nonlinear electric responses in glasses and glass ceramics. Master thesis, Johannes Gutenberg Universität Mainz, 2018.

[Blo07] S Blonkowski. Nonlinear capacitance variations in amorphous oxide metal-insulator-metal structures. *Applied Physics Letters*, 91(17):172903, 2007.

[BMH+17] H P Braun, A Mehmood, M Hovhannisyan, H Zhang, D S B Heidary, C Randall, M T Lanagan, R Jakoby, I M Reaney, M Letz, and H-J Elmers. Microwave properties and structure of La–Ti–Si–B–O glass-ceramics for applications in GHz electronics. *Journal of the European Ceramic Society*, 37(5):2137–2142, 2017.

[Boy08] R W Boyd. *Nonlinear Optics*. Academic Press, Burlington, 2008.

[Bra14] D A Bradley. Passive intermodulation (PIM) distance-to-fault analyzer and method to resolve distance-to-fault within a constrained receive band. US Patent 8 903 324, December 2 2014.

[BSS+18] J Breeze, E Salvadori, J Sathian, N M Alford, and C Kay. Continuous-wave room-temperature diamond maser. *Nature*, 555, 2018.

[CMO01] C Collado, J Mateu, and J M O'Callaghan. Nonlinear simulation and characterization of devices with HTS transmission lines using harmonic balance algorithms. *IEEE Transactions on Applied Superconductivity*, 11(1):1396–1399, 2001.

[CN+07] C B Carter, M G Norton, et al. *Ceramic materials: science and engineering*. Springer, 2007.

[Coh68] S B Cohn. Microwave Band Pass Filters Containing High-Q Dielectric Resonator. *IEEE Transactions on Microwave Theory and Techniques*, 16:218 – 227, 1968.

[DCS+19] P Delsing, A N Cleland, M J A Schuetz, J Knörzer, G Giedke, J I Cirac, K Srinivasan, M Wu, K C Balram, C Bäuerle, et al. The 2019 surface acoustic waves roadmap. *Journal of Physics D: Applied Physics*, 52(35):353001, 2019.

[DH04] H Dresig and F Holzweißig. Einfache nichtlineare und selbsterregte Schwinger. In *Maschinendynamik*. Springer, 2004.

[DP99] N B De Carvalho and J C Pedro. Large- and small-signal IMD behavior of microwave power amplifiers. *IEEE Transactions on Microwave Theory and Techniques*, 47(12):2364–2374, 1999.

[DS99] T Dahm and D J Scalapino. Nonlinear current response of a *d*-wave superfluid. *Physical Review B*, 60:13125–13130, 1999.

[DSKJH96] K De Smet, P Kędziora, Jadżyn, and L Hellemans. Dynamics of 2-Pyrrolidinone Self-Association by Nonlinear Dielectric Spectroscopy. *The Journal of Physical Chemistry*, 100(18):7662–7668, 1996.

[Ein05] A Einstein. Über die von der molekularkinetischen Theorie der Wärme geforderte Bewegung von in ruhenden Flüssigkeiten suspendierten Teilchen. *Annalen der Physik*, 4, 1905.

[EK35] H Euler and B Kockel. Über die Streuung von Licht an Licht nach der diracschen Theorie. *Naturwissenschaften*, 23(15):246–247, 1935.

[EKS19] C Entsfellner, B Kaindl, and M Schwab. Method for measuring passive intermodulation and measuring device. US Patent 10 270 546, April 23 2019.

[Eng20] H Engelmann. Schott internal communication, September 29 2020.

[Evo11] Evonik. Dielectric Properties Rohacell. Data sheed, 2011.

[FFK+93] K Fukuda, I Fujii, R Kitoh, Y Cho, and I Awai. Influence of Rare Earth Ions on BaO-TiO_2-Rare Earth Oxide Ceramics for Microwave Applications. *Japanese Journal of Applied Physics*, 32:1712–1715, 1993.

[Gre95] A L Greer. Metallic Glasses. *Science*, 267(5206):1947–1953, 1995.

[GT91] V L Gurevich and A K Tagantsev. Intrinsic dielectric loss in crystals. *Advances in Physics*, 40(6):719–767, 1991.

[Har28] R V L Hartley. Transmission of Information. *Bell System Technical Journal*, 7(3):535–563, 1928.

[HCC09a] J J Henrie, A J Christianson, and W J Chappell. Engineered Passive Nonlinearities for Broadband Passive Intermodulation Distortion Mitigation. *IEEE Microwave and Wireless Components Letters*, 19(10):614–616, 2009.

[HCC09b] J J Henrie, A J Christianson, and W J Chappell. Linear-nonlinear interaction's effect on the power dependence of nonlinear distortion products. *Applied Physics Letters*, 94(11):114101, 2009.

[HCC10] J J Henrie, A J Christianson, and W J Chappell. Linear–Nonlinear Interaction and Passive Intermodulation Distortion. *IEEE Transactions on Microwave Theory and Techniques*, 58(5):1230–1237, 2010.

[HDM75] L Hellemans and L De Maeyer. Absorption and dispersion of the field induced dielectric increment in caprolactam–cyclohexane solutions. *The Journal of Chemical Physics*, 63(8):3490–3498, 1975.

[HHH+03] M A Hein, R G Humphreys, P J Hirst, S H Park, and D E Oates. Nonlinear microwave response of epitaxial YBaCuO films of varying oxygen content on MgO substrates. *Journal of Superconductivity*, 16(5):895–904, 2003.

[HLK15] M Hovhannisyan, M Letz, and G Kissl. Glass-ceramic as a dielectric in the high-frequency range. US Patent 0018193, January 15 2015.

[HOH+02] M A Hein, D E Oates, P J Hirst, R G Humphreys, and A V Velichko. Nonlinear dielectric microwave losses in MgO substrates. *Applied Physics Letters*, 80(6):1007–1009, 2002.

[Hun09] S Hunklinger. *Festkörperphysik*. Oldenbourg, 2009.

[HvS81] S Hunklinger and M von Schickfus. Acoustic and Dielectric Properties of Glasses at Low Temperatures. In W A Phillips, editor, *Amorphous Solids. Topics in Current Physics*. Springer, 1981.

[ITNW92] Y Ishikawa, H Tamura, T Nishikawa, and K Wakino. Extremely low distortion dielectric ceramics. *Ferroelectrics*, 135(1):371–383, 1992.

[Jac99] J D Jackson. *Classical electrodynamics*. Wiley, 1999.

[JACJ+19] M Jenkins, D Z Austin, J F Conley Jr, J Fan, C H De Groot, L Jiang, Y Fan, R Ali, G Ghosh, M Orlowski, et al. Beyond the Highs and Lows: A Perspective on the Future of Dielectrics Research for Nanoelectronic Devices. *ECS Journal of Solid State Science and Technology*, 8(11):N159, 2019.

[JDL+20] P Jonsson, S Davis, P Linder, A Gomroki, A Zaidi, A P Carlsson, M Opsenica, I Sorlie, S Elmgren, et al. Ericssion Mobility Report, 2020.

[JGHB20] Q Jin, J Gao, H Huang, and L Bi. Mitigation Methods for Passive Intermodulation Distortion in Circuit Systems Using Signal Compensation. *IEEE Microwave and Wireless Components Letters*, 30(2):205–208, 2020.

[KCL+04] S J Kim, B J Cho, M-F Li, S-J Ding, C Zhu, M B Yu, B Narayanan, A Chin, and D-L Kwong. Improvement of voltage linearity in high-κ MIM capacitors using HfO_2-SiO_2 stacked dielectric. *IEEE Electron Device Letters*, 25(8):538–540, 2004.

[Key14] Keysight. Keysight X-Series Signal Analyzers. Manual N9060-90035, 2014.

[KG86] D Kajfez and P Guillon. *Dielectric Resonators*. Artech House, 1986.

[KGV+14] O Khaldi, P Gonon, C Vallée, C Mannequin, M Kassmi, A Sylvestre, and F Jomni. Differences between direct current and alternating current capacitance nonlinearities in high-k dielectrics and their relation to hopping conduction. *Journal of Applied Physics*, 116(8):084104, 2014.

[KH66] K C Kao and G A Hockham. Dielectric-fibre surface waveguides for optical frequencies. In *Proceedings of the Institution of Electrical Engineers*, volume 113, pages 1151–1158. IET, 1966.

[Kit73] C Kittel. *Einführung in die Festkörperphysik*. Wiley, 1973.

[KJDH98] P Kędziora, J Jadżyn, K De Smet, and L Hellemans. Nonlinear dielectric relaxation in non-interacting dipolar systems. *Chemical Physics Letters*, 289(5):541–545, 1998.

[KJH01] P Kędziora, J Jadżyn, and L Hellemans. Nonlinear dielectric relaxation in solutions of hydrogen bonded liquid crystalline carboxylic acid. *IEEE Transactions on Dielectrics and Electrical Insulation*, 8(3):485–487, 2001.

[KJH02] P Kędziora, J Jadżyn, and L Hellemans. Dynamics of the nonlinear dielectric properties of a nematogenic compound dissolved in a nonpolar medium. *Physical Review E*, 66:021709, 2002.

[Kru06] J Krupka. Frequency domain complex permittivity measurements at microwave frequencies. *Measurement Science and Technology*, 17(6):R55, 2006.

[KSB+20] D Kozlov, A P Shitvov, S Bulja, R Lundy, P Rulikowski, K Nolan, and R Enright. Practical Mitigation of Passive Intermodulation in Microstrip Circuits. *IEEE Transactions on Electromagnetic Compatibility*, 62(1):163–172, 2020.

[KSKK18] T Karpisz, B Salski, P Kopyt, and J Krupka. A Novel Approach to the Modeling of a Fabry-Perot Open Resonator. In *2018 IEEE/MTT-S International Microwave Symposium - IMS*, pages 1397–1400, 2018.

[LFN12] L Liu, M Flores, and N Newman. Microwave Loss in the High-Performance Dielectric $Ba(Zn_{1/3}Ta_{2/3})O_3$ at 4.2 K. *Physical Review Letters*, 109:257601, 2012.

[Lui90] P L Lui. Passive Intermodulation Interference in Communication Systems. *Electronics & Communication Engineering Journal*, 2:109 – 118, 1990.

[LZV+18] M Letz, W Zihan, S Viswanathan, M Jotz, H Maune, M Jost, P M Raj, V Sundaram, and R Tummala. Glass in Electronic Packaging and Integration: High Q Inductances for 2.35 GHz Impedance Matching in 0.05

mm Thin Glass Substrates. In *2018 IEEE 68th Electronic Components and Technology Conference (ECTC)*, pages 1089–1096, 2018.

[Maa03] S A Maas. *Nonlinear microwave and RF circuits*. Artech House, 2003.

[Mar13] U Martens. HT-XRD an einer Ba-Al-Ti-Schmelzprobe (VSM 41482). Prüfbericht 20-2013 00012, Schott, 2013.

[McM79] P McMillan. *Glass ceramics*. Academic Press, 1979.

[MDK11] S Miga, J Dec, and W Kleemann. *Non-linear dielectric response of ferroelectrics, relaxors and dipolar glasses*. InTech, 2011.

[MDP48] C G Montgomery, R H Dicke, and E M Purcell. *Principles of microwave circuits*. McGraw-Hill, 1948.

[MF62] A A Maradudin and A E Fein. Scattering of Neutrons by an Anharmonic Crystal. *Physical Review*, 128:2589–2608, 1962.

[MKJL04] J Mazierska, J Krupka, M V Jacob, and D Ledenyov. Complex permittivity measurements at variable temperatures of low loss dielectric substrates employing split post and single post dielectric resonators. In *2004 IEEE MTT-S International Microwave Symposium Digest (IEEE Cat. No.04CH37535)*, volume 3, pages 1825–1828, 2004.

[MLa19] K Leppänen M Latva-aho. Key drivers and research challenges for 6G ubiquitous wireless intelligence. University of Oulu, 2019.

[MM56] C G Malmberg and A A Maryott. Dielectric Constant of Water from 0° to 100° C. *Journal of research of the National Bureau of Standards*, 56(1):1, 1956.

[MTHT95] N Michiura, T Tatekawa, Y Higuchi, and H Tamura. Role of Donor and Acceptor Ions in the Dielectric Loss Tangent of $(Zr_{0.8}Sn_{0.2})TiO_4$ Dielectric Resonator Material. *Journal of the American Ceramic Society*, 78(3):793–796, 1995.

[Mun02] R Munro. Elastic Moduli Data for Polycrystalline Oxide Ceramics. NIST Interagency/Internal Report, 2002.

[NIH88] T Nishikawa, Y Ishikawa, and J Hattori. Measurement Method of Intermodulation Distortion of Dielectric Resonator. *IEICE Japanese Technical Report*, MW88-11:39, 1988. in Japanese.

[OAW+08] D E Oates, D Agassi, E Wong, A Leese de Escobar, and K Irgmaier. Nonlinear Meissner effect in a high-temperature superconductor: Local versus nonlocal electrodynamics. *Physical Review B*, 77(21):214521, 2008.

[Opt20] Advanced Optics. Optical Glass. Schott AG catalog, 2020.

[PC03] J C Pedro and N B Carvalho. *Intermodulation distortion in microwave and wireless circuits*. Artech House, 2003.

[PCGM12] L Padurariu, L Curecheriu, C Galassi, and L Mitoseriu. Tailoring nonlinear dielectric properties by local field engineering in anisotropic porous ferroelectric structures. *Applied Physics Letters*, 100(25):252905, 2012.

[Pfa97] H G Pfaender. *Schott Glaslexikon*. Münchner Verlagsgruppe, 1997.

[Poz11] D M Pozar. *Microwave engineering*. Wiley, 2011.

[PSW+11] T H Phung, P Steinmann, R Wise, Y Yeo, and C Zhu. Modeling the Negative Quadratic VCC of SiO_2 in MIM Capacitor. *IEEE Electron Device Letters*, 32(12):1671–1673, 2011.

[RI06] I M Reaney and D Iddles. Microwave Dielectric Ceramics for Resonators and Filters in Mobile Phone Networks. *Journal of the American Ceramic Society*, 89(7):2063–2072, 2006.

[Ric39] R D Richtmeyer. Dielectric Resonators. *Journal of Applied Physics*, 10(6):391–398, 1939.

[Ric17] R Richert. Nonlinear dielectric effects in liquids: a guided tour. *Journal of Physics: Condensed Matter*, 29(36):363001, 2017.

[RRR97] L Robles, M A Ruggero, and N C Rich. Two-Tone Distortion on the Basilar Membrane of the Chinchilla Cochlea. *Journal of Neurophysiology*, 77(5):2385–2399, 1997.

[Sch64] E Schlömann. Dielectric Losses in Ionic Crystals with Disordered Charge Distributions. *Physical Review*, 135:A413–A419, 1964.

[Sch88] H Scholze. *Natur und Struktur des Glases*. Springer, 1988.

[Seb08] M Sebastian. *Dielectric materials for wireless communication*. Elsevier, 2008.

[She07] J Sheen. Microwave Measurements of Dielectric Properties Using a Closed Cylindrical Cavity Dielectric Resonator. *IEEE Transactions on Dielectrics and Electrical Insulation*, 14:1139 – 1144, 2007.

[SKS18] A P Shitvov, D S Kozlov, and A G Schuchinsky. Nonlinear Characterization for Microstrip Circuits with Low Passive Intermodulation. *IEEE Transactions on Microwave Theory and Techniques*, 66:865 – 874, 2018.

[Sla50] J C Slater. The Lorentz Correction in Barium Titanate. *Physical Review*, 78:748–761, 1950.

[SMB81] J Schmachtel and H Müller-Buschbaum. Ein neues quaternäres Oxotitanat: $Ba_4Ti_{10}Al_2O_{27}$. *Zeitschrift für anorganische und allgemeine Chemie*, 472(1):89–94, 1981.

[SRTO94] D J Salvino, S Rogge, B Tigner, and D D Osheroff. Low Temperature AC Dielectric Response of Glasses to High DC Electric Fields. *Physical Review Letters*, 73:268–271, 1994.

[SSTNS+18] A Sayyadi-Shahraki, E Taheri-Nassaj, H Sharifi, J Gonzales, T Kolodiazhnyi, and N Newman. Origin of dielectric loss in $Ba(Co_{1/3}Nb_{2/3})O_3$ microwave ceramics. *Journal of the American Ceramic Society*, 101(4):1665–1676, 2018.

[Sta80] G H Stauss. Intrinsic sources of IM generation. Naval Research Laboratory Memorandum Report 4233, Ch. 5, 65-82, 1980.

[Ste80] J M Stevels. Local motions in vitreous systems. *Journal of Non-Crystalline Solids*, 40(1):69–82, 1980.

[SZS09] A Shitvov, D Zelenchuk, and A Schuchinsky. Carrier-power dependence of passive intermodulation products in printed lines. In *2009 Loughborough Antennas Propagation Conference*, pages 177–180, 2009.

[Tam06] H Tamura. Microwave dielectric losses caused by lattice defects. *Journal of the European Ceramic Society*, 26(10):1775–1780, 2006.

[THNW89] H Tamura, J Hattori, T Nishikawa, and K Wakino. Third Harmonic Distortion of Dielectric Resonator Materials. *Japanese Journal of Applied Physics*, 28:2528–2531, 1989.

[TS76] G P Tolstov and R A Silverman. *Fourier Series*. Dover Books on Mathematics. Dover Publications, 1976.

[TW16] D Truesdale and W Whiteley. System and method for measuring passive intermodulation (PIM) in a device under test (DUT). US Patent 9 455 792, September 27 2016.

[Val21] B Valentin. SEM/EDX an Schliere in N-SF66 - Scheibe. Prüfbericht OF-21-00107, Schott, 2021.

[VdV68] W E Van der Velde. *Multiple-input describing functions and nonlinear system design*. McGraw-Hill, 1968.

[Vel04] A V Velichko. Origin of the deviation of intermodulation distortion in high-Tc thin films from the classical 3:1 scaling. *Superconductor Science and Technology*, 17(1):1, 2004.

[VGJEK10] C Vallée, P Gonon, C Jorel, and F El Kamel. Electrode oxygen-affinity influence on voltage nonlinearities in high-k metal-insulator-metal capacitors. *Applied Physics Letters*, 96(23):233504, 2010.

[VH88] M Vints and L Hellemans. The measurement of non-linear dielectric effects with re-entrant cavities. In *1988 Fifth International Conference on Dielectric Materials, Measurements and Applications*, pages 340–343, 1988.

[Vog92] W Vogel. *Glaschemie*. Springer, 1992.

[WKD99] B A Willemsen, K E Kihlstrom, and T Dahm. Unusual power dependence of two-tone intermodulation in high-Tc superconducting microwave resonators. *Applied Physics Letters*, 74(5):753–755, 1999.

[WKGS15] J Wilkerson, I Kilgore, K Gard, and M Steer. Passive Intermodulation Distortion in Antennas. *IEEE Transactions on Antennas and Propagation*, 63:474–482, 2015.

[WKSA18] M Wang, I M Kilgore, M B Steer, and J J Adams. Characterization of Intermodulation Distortion in Reconfigurable Liquid Metal Antennas. *IEEE Antennas and Wireless Propagation Letters*, 17(2):279–282, 2018.

[WLL+08] C Wenger, G Lupina, M Lukosius, O Seifarth, H-J Müssig, S Pasko, and C Lohe. Microscopic model for the nonlinear behavior of high-k metal-insulator-metal capacitors. *Journal of Applied Physics*, 103(10):104103, 2008.

[Yag16] K Yagi. Passive intermodulation measurement apparatus. US Patent 9 354 262, May 31 2016.

[YMM+15] H Yamada, A Meier, F Mazzocchi, S Schreck, and T Scherer. Dielectric properties of single crystalline diamond wafers with large area at microwave wavelengths. *Diamond and Related Materials*, 58:1–4, 2015.

[Zuc72] R Zucker. Elementary Transcendental Functions. In M Abramowitz and I A Stegun, editors, *Handbook of Mathematical Functions*. National Bureau of Standards, 1972.

[ZWKU97] C Zuccaro, M Winter, N Klein, and K Urban. Microwave absorption in single crystals of lanthanum aluminate. *Journal of Applied Physics*, 82(11):5695–5704, 1997.

Danksagungen

[wegen Datenschutz entfernt]

Erklärung

Die vorliegende Arbeit wurde in der Zeit von Mai 2018 bis Juni 2021 am Institut für Physik im Fachbereich 08 - Physik, Mathematik und Informatik der Johannes Gutenberg-Universität, Mainz in Zusammenarbeit mit der Schott AG in Mainz angefertigt.

Hiermit versichere ich, dass ich die vorliegende Arbeit ohne unzulässige Hilfe Dritter und ohne Benutzung anderer als der angegebenen Hilfsmittel angefertigt habe. Die aus fremden Quellen direkt oder indirekt übernommenen Gedanken sind als solche kenntlich gemacht. Ich habe bisher keinen Promotionsversuch unternommen und die Arbeit wurde bisher weder im In- noch im Ausland in gleicher oder ähnlicher Form einer anderen Prüfungsbehörde vorgelegt.

Florian Bergmann
Mainz, Juni 2021

Beitragende

[wegen Datenschutz entfernt]

Lebenslauf

[wegen Datenschutz entfernt]